Thesis for the degree of Doctor of Philosophy

Strong Light-Matter Interactions in 2D Materials

Beatriz Ferreira



Department of Physics and Astronomy

Chalmers University of Technology

Göteborg, Sweden 2026

Strong Light-Matter Interactions in 2D Materials

Beatriz Ferreira

ISBN 978-91-8103-490-5
Acknowledgements, dedications, and similar personal statements in this thesis, reflect the author's own views.

© Beatriz Ferreira, 2026.

Doktorsavhandlingar vid Chalmers tekniska högskola
Ny serie nr 5947
ISSN 0346-718X
https://doi.org/10.63959/chalmers.dt/5947

Department of Physics and Astronomy Chalmers University of Technology
SE-412 96 Göteborg
Sweden
Telephone + 46 (0)31-772 1000

Cover illustration: The cover image artistically illustrates the formation of exciton–polaritons in a two-dimensional material embedded in an optical environment. The interaction between light and matter is represented by the coupling of two distinct entities, symbolizing the hybridization process that gives rise to new quasiparticles. The directional light beam emphasizes the role of optical excitation, while the structured landscape reflects the underlying two-dimensional material platform. Cover made with AI.

Printed at Chalmers Digitaltryck
Göteborg, Sweden 2026

Strong Light-Matter Interactions in 2D Materials
Beatriz Ferreira
Department of Physics and Astronomy
Chalmers University of Technology

Abstract

Integrating 2D materials into high-quality optical microcavities opens the door to fascinating many-particle phenomena, including the formation of exciton-polaritons. These are hybrid quasi-particles inheriting properties of both the constituent photons and excitons. The corresponding change in the dispersion relation has a large impact on the optics, dynamics and transport behaviour of the materials.
In this thesis, we aim to microscopically understand the optical response and propagation of exciton-polaritons in transition metal dichalcogenides (TMDs). The theoretical method is based on the density matrix formalism combined with the Hopfield approach. In particular, we investigate how the exciton diffusion changes in the strong coupling regime, i.e. when exciton-polaritons are formed. Furthermore, we study the impact of dark excitons on the optical response of upper and lower polariton branches in absorption spectra of molybdenum- and tungsten-based TMDs, which are known to be direct and indirect semiconductors, respectively. We show how different experimentally accessible quantities, such as temperature or mirror reflectance, can be exploited to tune the optical response of polaritons. By changing the cavity detuning, we vary the polariton energy relative to the unaffected dark excitons in such a way that we open or close specific phonon-driven scattering channels. In a joint theory-experiment, with the group of Christian Schneider (University of Oldenburg), we show that this controlled switching of scattering channels manifests in characteristic sharp changes in the optical spectra of polaritons. These spectral features can be exploited to extract the position of dark excitons. This suggests new possibilities for exploiting polaritons for fingerprinting nanomaterials via their unique exciton landscape. Overall, this work contributed to a better microscopic understanding of optics, dynamics and transport of exciton-polaritons in technologically promising 2D materials.

Keywords: exciton-polaritons, 2D materials, diffusion, absorption, detuning.

Acknowledgments

This thesis marks the end of a long and formative journey, which would not have been possible without the support, guidance, and encouragement of many people.

First and foremost, I would like to thank my main supervisor, Prof. Ermin Malic, for his guidance, insight, and continuous support throughout my PhD. His deep understanding of physics and enthusiasm for research have been a constant source of inspiration.

I would like to express my particular gratitude to Roberto Rosati for his patience and for the many helpful and insightful discussions we shared during my PhD. His willingness to exchange ideas, answer questions, and engage deeply with scientific problems has had a lasting impact on both this work and my development as a researcher.

I am also grateful to my collaborators and co-authors for the stimulating scientific exchanges that shaped this thesis. In particular, I would like to thank Jamie M. Fitzgerald and all collaborators involved in the joint theory–experiment efforts, especially the group of Christian Schneider, for fruitful collaboration and valuable discussions.

I thank my colleagues at the Department of Physics and Astronomy at Chalmers University of Technology for providing a supportive and inspiring research environment. The scientific discussions, shared challenges, and interactions made this journey intellectually rewarding and personally meaningful.

I am grateful to my friends who accompanied me throughout this time. Your support, perspective, and shared experiences made the demanding moments easier and the good moments even better.

I would also like to thank my boyfriend for his constant support, patience, and encouragement. His presence and understanding brought balance and strength throughout this journey.

Finally, I would like to express my deepest gratitude to my family, and especially to my parents, for their unconditional support and unwavering belief in me. During particularly difficult periods, including times when I faced burnout, their understanding, care, and encouragement gave me the strength to continue. I am profoundly grateful for everything they have done for me.

List of publications

This thesis consists of an introductory text and the following published articles:

I. **Microscopic modeling of exciton-polariton diffusion coefficients in atomically thin semiconductors**
Beatriz Ferreira, Roberto Rosati, and Ermin Malic
Physical Review Materials **6**, 034008 (2022)

II. **Signatures of dark excitons in exciton-polariton optics of transition metal dichalcogenides**
Beatriz Ferreira, Roberto Rosati, Jamie M. Fitzgerald, and Ermin Malic
2D Materials **10**, 015012 (2023)

III. **Revealing dark exciton signatures in polariton spectra of 2D materials**
Beatriz Ferreira, Hangyong Shan, Roberto Rosati, Jamie M. Fitzgerald, Lukas Lackner, Bo Han, Martin Esmann, Patrick Hays, Gilbert Liebling, Kenji Watanabe, Takashi Taniguchi, Falk Eilenberger, Sefaattin Tongay, Christian Schneider, and Ermin Malic
ACS Photonics **11** (6), 2215-2220 (2024)

My contribution to the listed publications
As the first author of Paper I-III, I developed the theoretical model, performed the numerical evaluations, analyzed the results and wrote the manuscripts with the aid of my main supervisor and the other authors.

Publications not appended in this thesis:

IV. **Circumventing the polariton bottleneck via dark excitons in 2D semiconductors**
Jamie M. Fitzgerald, Roberto Rosati, Beatriz Ferreira, Hangyong Shan, Christian Schneider, Ermin Malic
Optica **11.9**, 1346-1351 (2024)

Contents

Abstract . . . iii
Acknowledgments . . . iv
List of Publications . . . vii

1 Introduction **1**
1.1 Transition Metal Dichalcogenides . . . 1
1.2 Optical Microcavities . . . 4
1.3 Excitons in Transition Metal Dichalcogenides . . . 6
1.4 Exciton-Polaritons . . . 8
1.5 Overview of investigated Project . . . 11

2 Theoretical Framework **13**
2.1 Theory of Fabry-Perot Cavities . . . 13
2.1.1 Fabry–Pérot Cavity . . . 15
2.1.2 Quantum Langevin Equations and Input-Output Theory 17
2.2 Many-particle Hamiltonian in Second Quantization . . . 19
2.3 Excitons and the Wannier Equation . . . 29
2.3.1 Microscopic Polarization and Excitonic Basis . . . 30
2.3.2 Excitonic Hamiltonian . . . 32
2.4 Exciton-Polaritons and Hopfield Transformation . . . 34
2.5 Diffusion Coefficient for Polaritons . . . 41
2.6 Heisenberg Equations of Motion for Polaritons . . . 44
2.7 Polariton Absorption . . . 47

3 Polariton Transport **51**
3.1 Phonon-induced Scattering Rates . . . 51
3.1.1 Intra-valley Scattering . . . 52
3.1.2 Inter-valley Scattering . . . 54
3.1.3 Temperature Study of Scattering Rates . . . 56
3.2 Polariton Diffusion . . . 58

4 Polariton Optics **63**
4.1 Polariton Absorption of WSe_2 63
4.2 Critical Coupling Condition 65
4.3 Polariton Absorption of $MoSe_2$ 69
4.4 The Effect of the Environment 71
4.5 Effects of Changing Cavity Length 73
4.5.1 Temperature-Dependent Polariton Dynamics 75
4.5.2 Influence of Scattering Channels on Linewidth 76
4.5.3 Polariton Linewidth: Experimental and Theoretical Insights 77

5 Conclusion and Outlook **81**

Bibliography **83**

Papers **103**
Paper I 103
Paper II 113
Paper III 124

CHAPTER 1

Introduction

This thesis delves into the interaction of exciton-polaritons within transition metal dichalcogenides (TMD) and optical microcavities, emphasizing the novel phenomena arising from this interaction, their dynamics, and their technological applications. By integrating theoretical approaches like the density matrix formalism and the Hopfield model, we explore how these interactions influence the properties and behaviours of hybrid quasi-particles, potentially paving the way for new optoelectronic devices. The introductory focus on transition metal dichalcogenides, optical microcavities, excitons, and exciton-polaritons, each critical to understanding the complex interplay in these systems.

1.1 Transition Metal Dichalcogenides

Transition metal dichalcogenides (TMDs) are a class of two-dimensional materials with chemical formula MX_2, where M denotes a transition metal

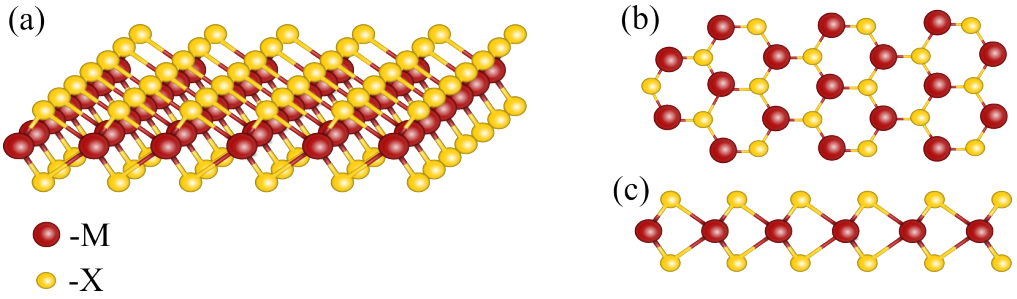


Figure 1.1: Structure of TMD. (a) Three-dimensional representation of the atomic structure of a TMD monolayer. (b) Top and (c) side perspectives of a TMD monolayer.

(e.g., Mo, W) and X a chalcogen (e.g., S, Se, or Te) [1–3]. A TMD monolayer consists of a plane of transition metal atoms sandwiched between two planes of chalcogen atoms, forming strong in-plane covalent bonds and weak out-of-plane van der Waals interactions [4–6], see Fig. 1.1. At the monolayer limit, the electronic band structure transitions from an indirect to a direct bandgap located at the K and K′ valleys, resulting in strong light–matter interaction and efficient optical absorption and emission [1, 7].

Strong spin–orbit coupling in TMDs leads to spin–valley locking, which gives rise to valley-contrasting optical selection rules enabling helicity-dependent excitation of specific valleys using circularly polarized light [4, 8]. This valley-selective optical response allows information to be encoded in the valley degree of freedom and forms the basis of emerging valleytronic concepts and potential quantum information applications [8–11]. Moreover, the discrete excitonic spectrum and coupled spin and valley degrees of freedom provide a versatile platform for exploring quantum phenomena in solid-state systems. Combined with nanoscale tunability and compatibility with established semiconductor technologies, TMDs represent promising platforms for optoelectronic and quantum photonic application [7, 12].

Another key feature of monolayer TMDs is their exceptionally strong light–matter interaction arising from reduced dielectric screening and enhanced Coulomb interactions in two dimensions. This leads to large oscillator strengths and exciton binding energies on the order of hundreds of meV, which dominate their optical response and enable efficient photoexcitation processes relevant for photodetectors, light-emitting devices, and photovoltaic applications [1, 13].

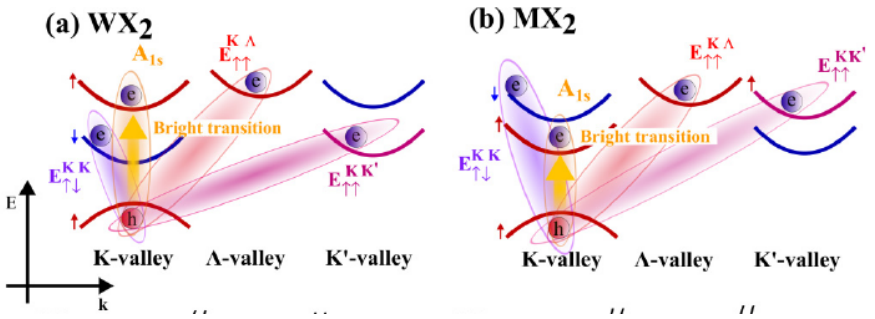


Figure 1.2: Excitonic landscape for a hole in the K valley. Schematic representation of electronic dispersions around the K and Λ valleys for (a) tungsten-based TMDs (WS_2 and WSe_2) and (b) molybdenum-based TMDs (MoS_2 and $MoSe_2$). Adapted from [16].

Additionally, the mechanical flexibility and environmental stability of TMDs facilitate integration into flexible and robust electronic and photonic platforms [2, 14].

Monolayer TMDs exhibit a rich excitonic landscape comprising both optically active (bright) and optically inactive (dark) exciton states, each playing distinct roles in optical dynamics and relaxation processes, see Fig. 1.2. Bright excitons arise when the electron and hole reside in the same valley with parallel spins, enabling efficient coupling to light through favourable optical selection rules [15–17]. In contrast, dark excitons involve spin- or momentum-forbidden configurations, such as electrons located in the Λ or K′ valleys, which render them optically inactive under direct excitation [18–23]. These dark states play a central role in relaxation pathways, thermalisation processes, and energy transfer dynamics. The interplay between different excitonic states gives rise to complex spatio-temporal dynamics, including non-classical diffusion [24], transient negative diffusion [25], strain-dependent transport [26], accelerated hot-exciton diffusion [27], spatial halo formation [28–30], and unconventional exciton funneling effects [31], and rich transport phenomena arising from exciton-phonon and exciton-exciton interactions [32]. These phenomena highlight the importance of the excitonic landscape for understanding transport properties in TMD systems.

Beyond monolayers, TMDs can be assembled into vertical and lateral heterostructures, enabling additional control over electronic and optical prop-

erties [33–43]. Vertical heterostructures support interlayer excitons, where electrons and holes reside in different layers, leading to long lifetimes and large dipole moments [33, 37, 44]. Lateral heterostructures allow the formation of charge-transfer excitons at in-plane interfaces, enabling spatially resolved manipulation of optical responses [23, 37–39, 43–49].

When integrated into optical microcavities, TMD monolayers can enter the strong coupling regime, where excitonic and photonic modes hybridize to form exciton–polaritons [4]. This regime is characterized by Rabi splitting in optical spectra and enables the exploration of hybrid light–matter physics combining the coherence of photons with strong excitonic interactions. Heterostructures incorporated into microcavities further expand this landscape, allowing interlayer excitons with long lifetimes to form distinct polaritonic states and potentially enabling new collective quantum phenomena [50, 51].

Despite these opportunities, challenges related to material quality, scalability, and environmental stability remain important considerations for technological implementation [52, 53]. Continued advances in fabrication and characterization are therefore essential for fully exploiting the potential of TMD-based systems.

1.2 Optical Microcavities

The properties of the optical microcavity determine the photonic component of polaritons and thus control the detuning-dependent scattering mechanisms investigated in this thesis. We therefore introduce the key cavity parameters relevant for the microscopic modelling of polariton transport and optical response.

Optical microcavities confine electromagnetic fields within a small mode volume, enhancing light–matter interaction and enabling the strong coupling regime [54–56]. A widely used implementation is the Fabry–Pérot cavity, consisting of two parallel mirrors separated by a finite distance [57, 58], see Fig. 1.3. These mirrors are typically realized as distributed Bragg reflectors (DBRs), composed of alternating high- and low-refractive-index layers that achieve high reflectivity through constructive interference. The resulting

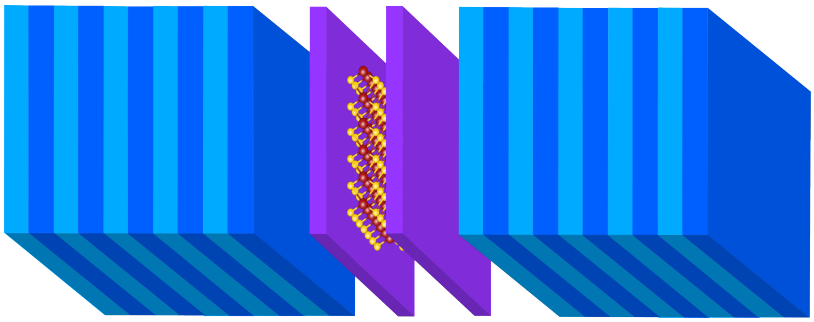


Figure 1.3: Schematic illustration of an hBN-encapsulated TMD monolayer in a Fabry–Pérot cavity.

cavity supports discrete photonic modes, increasing photon lifetime and interaction strength with embedded materials such as TMD monolayers.

The key parameters defining cavity behaviour include resonance frequency, quality factor (Q-factor), and mode volume. These quantities can be engineered through mirror reflectivity, cavity length, and refractive-index design [55, 59, 60].

In this thesis, we focus on Fabry–Pérot microcavities integrating TMD monolayers encapsulated in hexagonal boron nitride (hBN) [4], as illustrated in Fig. 1.3. Encapsulation reduces environmental disorder, preserves optical linewidths, and enables robust strong light–matter coupling [61]. By tuning cavity detuning and Q-factor, it becomes possible to explore polariton dispersion, scattering dynamics, and collective phenomena such as Bose–Einstein condensation and superfluid behaviour [62–64].

Beyond planar Fabry–Pérot cavities, alternative photonic architectures—including photonic crystal cavities and waveguide-based systems—offer additional control over light confinement and dispersion engineering [65, 66]. Such versatility highlights the central role of optical microcavities in studying hybrid light–matter states in two-dimensional material platforms.

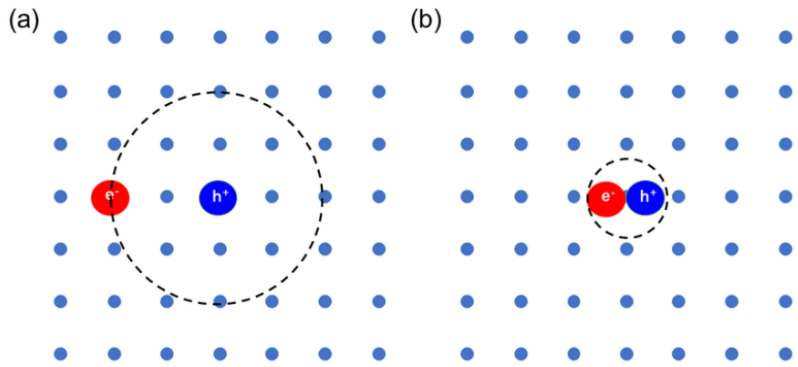


Figure 1.4: Schematic of two types of excitons: (a) Wannier exciton and (b) Frenkel exciton. Figure taken from [67].

1.3 Excitons in Transition Metal Dichalcogenides

The reduced dielectric screening and strong Coulomb interactions in monolayer TMDs result in tightly bound excitonic states that dominate the optical response even at room temperature. Understanding the nature and hierarchy of these excitonic states is therefore essential for describing light–matter interactions in TMD-based systems. Excitons in TMDs exhibit unique properties due to the distinct band structure and reduced dimensionality of these 2D materials. These quasiparticles, consisting of bound electron-hole pairs formed by Coulomb interaction, are important in determining the optical responses of TMDs, such as absorption, emission, and energy transport [7, 51, 68, 69].

While TMDs predominantly support Wannier-Mott excitons, it is also relevant to compare them with Frenkel excitons typically found in organic semiconductors and molecular crystals, see Fig. 1.4. Frenkel excitons have a much smaller spatial extent, are confined often to a single molecule or lattice site, and exhibit higher binding energies. However, due to their highly localized nature, Frenkel excitons contribute less to the electrical conductivity and are not as influential in the optoelectronic properties of inorganic semiconductors like TMDs [70, 71]. In TMDs, excitons predominantly exhibit Wannier-Mott characteristics due to the materials' high dielectric constant and the

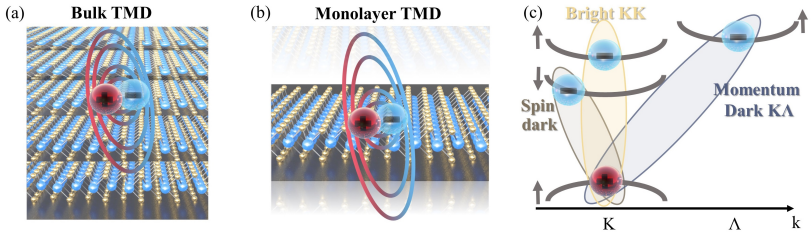


Figure 1.5: Schematic representation of excitons in (a) bulk versus (b) monolayer TMD, highlighting the influence of reduced dielectric screening in the monolayer form which enhances exciton binding energies. Panel (c) shows the representation of different exciton types, bright and dark. Figure taken from [72].

extensive spatial extent of the electron-hole pairs compared to the lattice dimensions [7, 69, 73]. The electron-hole interaction within these materials is influenced by the degree of dielectric screening, which varies significantly between the bulk and monolayer forms. In bulk TMDs, as shown in Figure 1.5(a), the three-dimensional environment provides more effective dielectric screening, reducing exciton binding energies. Conversely, in monolayer TMDs, depicted in Figure 1.5(b), the reduced thickness limits the dielectric screening effect. This diminished screening in two-dimensional environments leads to considerably enhanced exciton binding energies, often exceeding hundreds of meV, which are substantially higher than those found in conventional bulk semiconductors. Such high binding energies contribute to the unique optical properties of monolayer TMDs. From the perspective of light–matter interaction, excitons act as resonant oscillators that mediate coupling between electronic excitations and confined photonic modes. The large oscillator strength and discrete excitonic spectrum in monolayer TMDs therefore make them particularly favourable systems for entering the strong coupling regime and forming exciton–polaritons.

TMD monolayers support Wannier-Mott excitons, including a variety of excitonic states such as bright and dark excitons, trions, and biexcitons [73–75]. The rich excitonic landscape in TMDs, characterized by bright excitons that couple strongly with light and dark excitons that participate in complex scattering processes, contributes to the unique properties of exciton-polaritons when TMDs are integrated into microcavities [51]. In Figure 1.5(c) it is represented the different exciton types, bright and dark, and their respective energy transitions.

In vertical heterostructures, interlayer excitons are formed, possessing long lifetimes and tunable properties that are valuable for exploring exciton transport and polaritonic effects [44, 45]. Recent studies have demonstrated that even indirect excitons, such as interlayer excitons, can couple strongly with light through hybridization mechanisms, resulting in the formation of hybridized exciton-polaritons with unique optical characteristics [76]. This hybridization enables the exploration of novel polaritonic phenomena in TMD heterostructures, offering new opportunities for manipulating light-matter interactions in 2D materials.

Charge transfer excitons in lateral heterostructures allow for spatially engineered optical properties [26]. The spatial confinement and interface characteristics in these structures provide a versatile platform for studying exciton dynamics [42] and light-matter interactions at the nanoscale.

The dynamics of excitons in TMDs include various processes like exciton diffusion, scattering, and recombination [24, 25, 27, 32]. The strong oscillator strength and rich excitonic landscape of TMD monolayers make them particularly suitable for integration into optical microcavities, where excitons can coherently interact with confined photonic modes. Understanding these dynamics is essential for manipulating light-matter interactions in TMD-based microcavities, facilitating the exploration of phenomena such as Bose-Einstein condensation in exciton-polariton systems.

1.4 Exciton-Polaritons

When excitonic resonances in TMD monolayers are embedded within optical microcavities, the confined photonic modes can strongly couple to excitons, leading to hybridization between light and matter. In this regime, the eigenstates of the coupled system become exciton–polaritons. While exciton–polaritons have been extensively studied in conventional semiconductor platforms, TMD-based systems introduce additional complexity due to the presence of multiple excitonic states, including dark excitons. Understanding how these states modify polariton formation, transport, and optical response constitutes the central objective of this thesis. The Hopfield framework discussed here forms the basis for the microscopic modelling of polariton

diffusion and absorption developed in subsequent chapters.

Exciton–polaritons are hybrid quasiparticles arising from strong coupling between excitons and cavity photons [77, 78]. Within the Hopfield description, the system is treated in terms of new normal modes obtained through diagonalization of the light–matter Hamiltonian, resulting in upper and lower polariton branches that inherit properties from both photonic and excitonic components.

However, the word polariton is not exclusive to exciton-polaritons. Polaritons broadly describe hybrid states resulting from the interaction between light and matter, where an electromagnetic field couples with an elementary matter excitation [79–81]. Depending on the type of matter excitation, various kinds of polaritons can form, such as surface plasmon-polaritons [80], phonon-polaritons [82], and magnon-polaritons [83]. More specifically, a polariton is a coupled mode of the external electromagnetic field and an electric or magnetic dipole-carrying excitation, meaning a normal mode of the material that may linearly couple to the electromagnetic field through its electrical or magnetic character [79]. These excitations can be either single-particle electronic transitions (e.g., interband transitions in insulators) or many-body excitations (such as excitons and plasmons).

Exciton-polaritons represent a special case where excitons (electron-hole pairs) couple with photons to form these quasiparticles, retaining the properties of both [59, 84]. In the context of optoelectronics, the huge light-matter interaction demonstrated by TMDs has made them highly attractive for practical device applications [4]. Liu et al. were the first to confirm the formation of polariton states in a MoS_2 monolayer integrated into a microcavity by performing angle-resolved reflectivity and photoluminescence measurements [4].

Due to their mixed nature, exciton-polaritons have several remarkable properties:

- **Small Effective Mass**: The photonic component grants polaritons a small effective mass, enabling rapid propagation and making them ideal for transport applications [85–88]. Given their light component, polaritons show an interesting transport behaviour, resulting in fast

propagation in the ballistic regime [85, 87, 88].

- **Bose-Einstein Condensation**: The bosonic nature of polaritons allows them to undergo Bose-Einstein condensation (BEC) at relatively high temperatures, leading to the formation of coherent quantum states with properties like superfluidity [62, 89, 90].
- **Nonlinear Interactions**: Exciton-polaritons exhibit strong nonlinear interactions, crucial for developing optical switches, transistors, and other photonic devices [91–93].
- **Tunable Dispersion**: The dispersion of exciton-polaritons can be precisely controlled by modifying cavity parameters, allowing exploration of quantum phases of matter [84, 94].

Exciton–polaritons have been extensively studied using a wide range of experimental techniques, including angle-resolved spectroscopy and time-resolved optical measurements, which provide access to their dispersion, dynamics, and coherence properties [95, 96]. The hybrid light–matter nature of polaritons has enabled the observation of diverse phenomena, ranging from nonlinear optical effects and Bose–Einstein condensation to analog quantum simulations [84, 92]. While these developments highlight the versatility of polariton systems, the present thesis focuses specifically on the microscopic mechanisms governing polariton transport and optical response in TMD-based platforms, where dark excitons introduce additional scattering channels and modify the hybridization landscape.

In TMD monolayers, exciton-polaritons exhibit unique dynamics due to the presence of various excitonic states, including bright and dark excitons. The signature of dark excitons can be found in the optical spectrum of TMDs [15]. The coupling between these excitons and cavity photons leads to complex transport behaviour, influenced by polariton-phonon scattering processes. By varying the cavity detuning, researchers can modify the polariton energy relative to dark excitons, effectively controlling the scattering channels and influencing the optical spectra of the polaritons. One can even turn the dark WS_2 into a bright material [97].

While exciton–polaritons have been extensively studied in conventional semiconductor systems, TMD-based platforms introduce additional complexity

due to the presence of dark excitons and strong many-body interactions. By combining the exciton density matrix formalism with the Hopfield approach [78], the study examines how cavity properties and excitonic interactions influence polariton properties. Specifically, we investigate how the strong coupling regime impacts the optical absorption and transport behaviour of polaritons. These findings aim to contribute to the development of TMD-based optoelectronic devices, quantum technologies, and the simulation of fundamental physics phenomena.

1.5 Overview of investigated Project

In the **first paper**, "Microscopic modelling of exciton-polariton diffusion coefficients in atomically thin semiconductors," we developed a theoretical framework that combines the exciton density matrix formalism with the Hopfield model. This framework enabled us to predict polariton diffusion coefficients that are significantly enhanced compared to bare exciton diffusion.

The **second paper**, "Signatures of dark excitons in exciton-polariton optics of transition metal dichalcogenides," highlighted the role of dark excitons in shaping the optical response of TMDs. We demonstrated that the incorporation of dark exciton dynamics into the polariton spectra is crucial for accurately interpreting experimental results, thereby enhancing the understanding of light-matter interactions in these materials.

In our **third paper**, "Revealing dark exciton signatures in polariton spectra of 2D materials," we further investigated the impact of dark excitons on the optical properties of polaritons in TMDs. By analyzing various detuning conditions, we provided experimental evidence for the influence of dark excitons in polariton systems.

This thesis is organized in the following way. First, we introduce the theoretical framework in Chapter 2, in particular, we study the polariton dispersion and group velocity, which will be necessary for the following chapters. Then, we discuss the polariton-phonon scattering rates in Chapter 3, leading to the polariton diffusion coefficient (Paper I). Next, in Chapter 4 we study the

polariton absorption coefficient (Paper II and III). Finally, we end with a conclusion and future work prospects in Chapter 5.

CHAPTER 2

Theoretical Framework

In this chapter, we introduce the fundamental concepts underlying the theoretical framework for studying exciton-polaritons in transition metal dichalcogenides (TMDs) integrated into optical microcavities. The chapter is divided into sections covering the Theory of Fabry-Perot Cavities, many-particle systems in second quantization, excitons and the Wannier equation, and finally, exciton-polaritons and their interactions. The aim is to provide a comprehensive understanding of the essential theoretical tools needed for describing strong light-matter interactions in these systems.

2.1 Theory of Fabry-Perot Cavities

Because polariton dispersion and optical response depend critically on cavity losses and input–output coupling, we derive the Fabry–Perot framework required for quantitative comparison with absorption spectra and transport properties analysed later. In this section, we review the fundamental con-

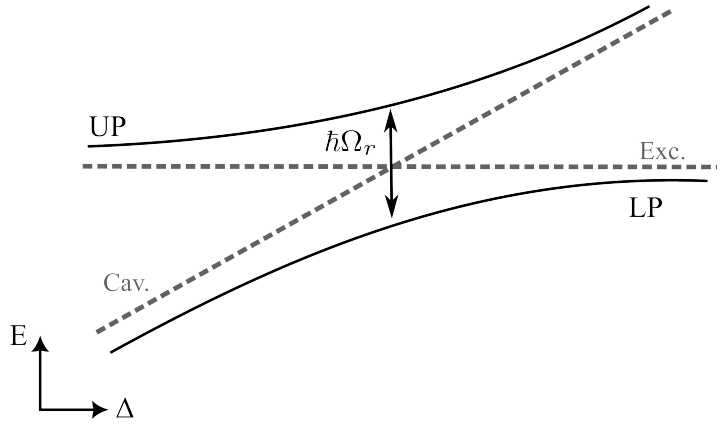


Figure 2.1: Schematic representation of how the exciton and photon modes hybridize, splitting into two new modes, LP and UP, which are separated by the Rabi splitting $\hbar\Omega_R$ at the anti-crossing of the exciton and cavity energies.

cepts of optical cavities [55], with particular emphasis on the Fabry–Pérot configuration. Fabry–Pérot resonators are central to the realization of exciton–polaritons, especially in systems based on transition metal dichalcogenide (TMD) monolayers. These cavities consist of two highly reflective mirrors that confine the electromagnetic field within a well-defined spatial region, leading to discrete photonic modes.

When the cavity resonance is tuned into spectral proximity with excitonic transitions in a TMD monolayer, strong light–matter coupling can be achieved. Owing to their large exciton binding energies and high oscillator strengths, TMDs are particularly well suited for integration into Fabry–Pérot cavities [4, 5, 98–100]. The resulting field confinement enhances the interaction between cavity photons and excitons, enabling the formation of hybrid exciton–photon states.

In this regime, the spatial overlap between the confined cavity modes and the excitonic transitions leads to a coherent energy exchange between light and matter, giving rise to a characteristic Rabi splitting of the dispersion into lower and upper polariton branches, as illustrated in Fig. 2.1.

2.1.1 Fabry–Pérot Cavity

A Fabry–Pérot cavity consists of two parallel mirrors separated by a distance L, forming an optical resonator that supports discrete longitudinal photon modes. Light confined between the mirrors undergoes multiple reflections, giving rise to standing-wave field distributions along the cavity axis. The resonance frequencies of these modes are determined by the cavity length and the optical boundary conditions imposed by the mirrors.

When a TMD monolayer is placed inside the cavity, its excitonic transitions can interact with the confined photon modes. By adjusting the cavity length L, the photonic resonance can be tuned into spectral alignment with the exciton energy, enabling the study of exciton–photon coupling in a controlled manner. In the strong coupling regime, this interaction leads to an anticrossing of the exciton and photon dispersions, which manifests as a Rabi splitting in the cavity transmission and reflection spectra [4, 84].

The formation of exciton–polaritons arises from the coherent and reversible exchange of energy between the excitonic and photonic components of the system [54, 56]. This regime is reached when the exciton–photon coupling strength exceeds the combined decay rates of the excitonic and photonic modes. In contrast, if this condition is not fulfilled, the system remains in the weak coupling regime, where the interaction is perturbative and no hybrid modes are formed. Owing to their large exciton binding energies and high oscillator strengths, TMD monolayers are particularly well suited for realizing strong coupling in Fabry–Pérot cavities, even at room temperature [4, 74].

Cavity Decay Rate and Quality Factor

The decay rate κ describes the rate at which photons leak out of the cavity due to the finite reflectivity of the mirrors. For a cavity with mirror reflectivities R_1 and R_2, the decay rate κ is given by [56, 57]:

$$\kappa = \frac{c(1 - R_1 R_2)}{2L\sqrt{R_1 R_2}}, \tag{2.1}$$

where c is the speed of light in the medium within the cavity, and L is the cavity length. This decay rate is directly related to the cavity's ability to store photons and determines the spectral linewidth of the cavity modes.

The quality factor Q of the cavity, which measures the sharpness of the resonance, is defined by:

$$Q = \frac{\omega_{\text{cav}}}{\kappa}, \tag{2.2}$$

where ω_{cav} is the resonance frequency of the cavity mode. Higher Q-factors indicate lower losses and more pronounced resonant effects, which are particularly important in achieving strong coupling with TMD excitons [55].

Reflection and Transmission in a Bare Cavity

For a bare Fabry–Pérot cavity (i.e., without excitonic effects), we can derive the reflection and transmission properties. The transmitted field can be written as

$$\mathbf{E}^t_{\text{out}} = E_0 e^{-i\omega t} \frac{1}{1 - \sqrt{R_1 R_2} e^{i\phi_{RT}}}, \tag{2.3}$$

where R_1 and R_2 are the intensity reflectivities of the two cavity mirrors. The phase

$$\phi_{RT} = 2kL\cos\theta + \phi_1 + \phi_2 \tag{2.4}$$

denotes the round-trip phase accumulated by the optical field inside the cavity. Here, $k = 2\pi/\lambda$ is the wavevector of the cavity photon in the medium, L is the mirror separation, and θ is the angle of propagation with respect to the cavity normal. The quantities ϕ_1 and ϕ_2 account for the phase shifts acquired upon reflection from the two cavity mirrors.

The corresponding transmitted intensity is then given by

$$I^t_{\text{out}} = \frac{I_0}{\left|1 - \sqrt{R_1 R_2} e^{i\phi_{RT}}\right|^2}. \tag{2.5}$$

When treating exciton–polaritons, this result provides an important consistency check of the theoretical framework. By setting the photonic Hopfield coefficient equal to unity, corresponding to purely photonic cavity modes, the expressions above are recovered.

These expressions agree with the results from the T-matrix approach, which describes the transmission and reflection behaviour of a bare cavity [101]. The T-matrix method, or transition matrix method, is a mathematical framework

used in the field of scattering theory. It is particularly useful for analyzing how waves, such as light, interact with objects, leading to transmission and reflection. The T-matrix relates electric and magnetic field coefficients across dielectric layers in stratified media. This consistency between the quantum and classical descriptions validates the framework and serves as a solid foundation for extending the analysis to exciton-polariton systems. For further details on the T-matrix method, see [102].
This section highlighted the foundational importance of Fabry-Pérot resonators in polariton physics. Their role in confining photons to interact strongly with excitons in TMDs is pivotal for achieving a strong coupling regime. This sets the stage for the subsequent discussions on polariton dispersion, dynamics, and quantum frameworks.

2.1.2 Quantum Langevin Equations and Input-Output Theory

Quantum open systems, like optical microcavities integrated with TMDs, are modelled using the quantum Langevin equations. These describe the time evolution of the system's degrees of freedom under the influence of both coherent dynamics and noise from the environment [103, 104]. The Langevin formalism is particularly suited for systems like exciton-polaritons in TMD monolayers integrated into optical microcavities, where interactions between light and matter play a significant role. The inclusion of noise and dissipation through the Langevin approach allows us to model how the system couples to its environment and how photons leak from the cavity, essential for understanding the dynamics and the measurement processes of polaritonic systems.

To analyze light-matter interactions in the Fabry-Pérot cavity, we employ a quantum approach where the electromagnetic fields inside and outside the cavity are quantized separately. We consider a single optical mode in the cavity, denoted by the annihilation and creation operators $\hat{a}$ and $\hat{a}^\dagger$ for the cavity photons, while fields outside the cavity are represented as continuum modes. This setup leads to input-output relations, connecting the internal and external fields [103, 105, 106].

The Hamiltonian describing the cavity photons in second quantization is given by

$$H_{\text{cav}} = \hbar\omega_{\text{cav}}\hat{a}^\dagger\hat{a}. \tag{2.6}$$

The interaction between the cavity field and the external environment, which consists of a continuum of modes outside the cavity, is represented by the Hamiltonian [107]

$$H_{\text{ext}} = i\hbar\int_{-\infty}^{\infty} d\omega\,\kappa(\omega)\left[\hat{b}^\dagger(\omega)\hat{a} - \hat{b}(\omega)\hat{a}^\dagger\right], \tag{2.7}$$

where $\kappa(\omega)$ is the coupling strength between the cavity field and the continuum, and $\hat{b}(\omega)$ and $\hat{b}^\dagger(\omega)$ are the annihilation and creation operators for the external modes.

This quantum approach aligns with the classical coupled-mode theory in the limit of large photon numbers, capturing the cavity's response to external fields. The Markov approximation assumes memoryless coupling between cavity and bath modes, implying that the bath correlation time is much shorter than the system dynamics [108]. This simplification, combined with input-output formalism, enables a clear description of the coupling of inner and outer cavity photons.

The input-output formalism relates the fields inside the cavity to the incoming and outgoing fields [103]. The output field $\hat{b}_{\text{out}}(t)$ is related to the input field $\hat{b}_{\text{in}}(t)$ by:

$$\hat{b}_{\text{out}}(t) = \hat{b}_{\text{in}}(t) + \sqrt{\kappa}\hat{a}(t). \tag{2.8}$$

In polariton experiments, the transmission and reflection spectra reveal the Rabi splitting and polariton resonances. By tuning the cavity length or changing the TMD properties, the polariton modes can be manipulated, making these systems ideal for studying light-matter interactions in the strong coupling regime [56, 84, 97]. By adopting the quantum Langevin framework, we bridge the gap between theoretical models and experimental observables. This formalism allows us to study polariton dynamics in open systems, including the effects of cavity losses and external coupling, offering a comprehensive understanding of TMD-based polariton systems. Having established the fundamental properties of Fabry-Pérot cavities and their role in confining photons, we now turn to a many-particle description of the

system. This framework enables us to model the interactions between photons and excitons within the cavity, laying the groundwork for describing hybrid light-matter quasiparticles.

2.2 Many-particle Hamiltonian in Second Quantization

To obtain a microscopic description of polariton dynamics beyond phenomenological models, we construct the full many-particle Hamiltonian including electron, phonon, and photon interactions. This framework enables the treatment of dark exciton scattering processes central to the results of this thesis. Second quantization is a powerful formalism used to describe many-particle quantum systems, particularly when dealing with indistinguishable particles such as excitons and photons [69, 109, 110]. In contrast to the first quantization, where the focus is on the wavefunctions of individual particles, the second quantization shifts the emphasis to the occupation of quantum states. This approach simplifies the treatment of systems with varying numbers of particles, making it particularly useful for studying the interactions between quasiparticles in condensed matter systems [69, 111, 112].

In the context of exciton-polaritons, second quantization provides a convenient framework to describe the creation and annihilation of excitons and photons, allowing us to capture the dynamics of the coupled light-matter system [59, 78]. By introducing creation, $c_i^\dagger$ and annihilation operators, c_i acting on the state i, we can formalize the processes in which particles are added to or removed from the system, paving the way to describe interactions between these particles. These particles can have either fermionic (+) or bosonic (-) character, which is reflected in their respective anti-commutation or commutation relations. Fermions, such as electrons, obey the Pauli exclusion principle and have half-integer spin, while bosons, like photons, have integer spin and can occupy the same quantum state. Then, the commutation and anti-commutations

relations are written as

$$[\hat{c}_i, \hat{c}_j]_\pm = \left[\hat{c}_i^\dagger, \hat{c}_j^\dagger\right]_\pm = 0 \tag{2.9}$$

$$\left[\hat{c}_i^\dagger, \hat{c}_j\right]_\pm = \delta_{ij}, \tag{2.10}$$

with the + and - indicating anti-commutation and commutation, respectively. As such, any one- or two-particle operator is expressed as

$$\hat{\mathcal{O}}^{(1)} = \sum_{ij} \langle i|\hat{\mathcal{O}}^{(1)}|j\rangle \hat{c}_i^\dagger \hat{c}_j, \tag{2.11}$$

$$\hat{\mathcal{O}}^{(2)} = \frac{1}{2}\sum_{ijlm} \langle i,j|\hat{\mathcal{O}}^{(2)}|l,m\rangle \hat{c}_i^\dagger \hat{c}_j^\dagger \hat{c}_l \hat{c}_m. \tag{2.12}$$

This approach is particularly useful for handling the system's Hamiltonian and defining microscopic quantities.

The Hamiltonian plays a critical role in describing the time evolution of a system. In this work, we consider the interactions within a cavity-embedded monolayer of transition metal dichalcogenides (TMDs), a many-particle system involving excitons and photons. The objective is to obtain the Hamiltonian describing the exciton-polaritons and their interactions. However, before defining the polaritonic Hamiltonian, we will first examine the underlying basis from which it is constructed. The Hamiltonian of this system is the sum of several contributions as

$$\hat{H} = \hat{H}_\mathrm{e}^0 + \hat{H}_\mathrm{phon}^0 + \hat{H}_\mathrm{phot}^0 + \hat{H}_\mathrm{bath} + \hat{H}_\mathrm{e\text{-}e} + \hat{H}_\mathrm{e\text{-}phon} + \hat{H}_\mathrm{e\text{-}phot} + \hat{H}_\mathrm{phot\text{-}bath}, \tag{2.13}$$

where we have in order of appearance quasi-free electrons in a lattice, free phonons, free photons inside and outside the cavity, and the interactions between electrons (electron-electron), between electrons and phonons (electron-phonon), between electrons and photons (electron-photon), as well as between photons inside and outside the cavity (photon-bath).

Quasi-free electrons in a lattice

In a crystal, electrons experience the periodic potential created by the ion lattice [113–115], where some of these electrons are shared and quasi-free. In the simplest approximation, we can treat the electrons as quasi-free, meaning

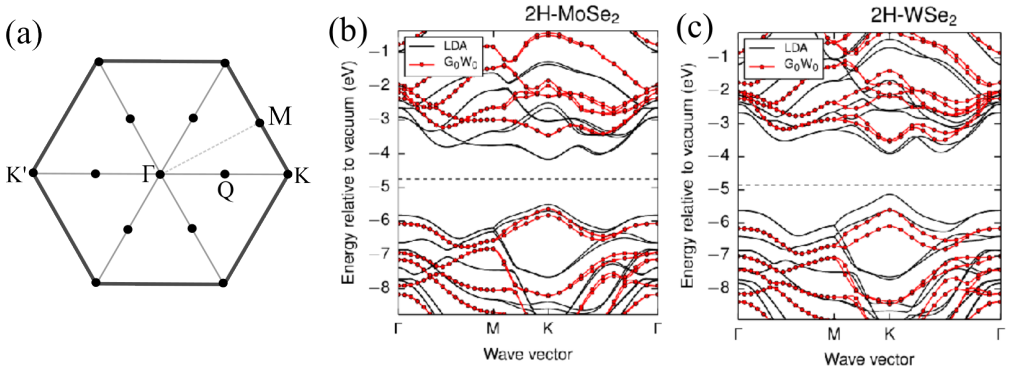


Figure 2.2: Electronic band structure of monolayer transition metal dichalcogenides. (a) Hexagonal Brillouin zone showing the high-symmetry points *Gamma*, K, and M, as well as the Q valley along the Γ–K direction. (b,c) Calculated band structures of monolayer 2H-$MoSe_2$ and 2H-WSe_2 along the high-symmetry path $\Gamma - M$–K–Γ. Black lines correspond to density functional theory (LDA) calculations, while red symbols indicate quasiparticle energies obtained within the G_0W_0 approximation. The dashed line marks the vacuum reference level. Adapted from Ref. [118]

.

their motion is only weakly perturbed by the lattice potential. The band structure of a material represents the relationship between the energy levels and the momenta of these electrons. It arises from the quantum mechanical nature of electrons in the periodic lattice and determines the allowed energies, which form discrete bands separated by forbidden energy gaps. For transition metal dichalcogenides (TMDs), the conduction- and valence-band extrema occur at specific high-symmetry points in the Brillouin zone—such as Γ, K, and the Λ (or Q) valleys—where the electrons and holes predominantly reside, as shown in Fig. 2.2. [7, 116, 117].

Near these symmetry points, the band structure can be approximated as parabolic, meaning the electron behaves as a free particle with an effective mass. This effective mass accounts for interactions with the periodic potential of the lattice. In this approximation, the energy ε_i of the electron is related to its effective mass m and wavevector $\mathbf{k}$ by:

$$\varepsilon_i = \frac{\hbar^2 k^2}{2m}, \tag{2.14}$$

where $\hbar$ is the reduced Planck's constant and $\mathbf{k}$ is the crystal momentum.

Here we employ the effective-mass approximation near the band extrema, which assumes parabolic dispersion and neglects higher-order band structure effects. This approximation is valid for low-momentum excitons considered in this work. The Hamiltonian for quasi-free electrons can then be expressed as:

$$\hat{H}_{\mathrm{e}}^{0} = \sum_{i} \varepsilon_i \hat{d}_i^{\dagger} \hat{d}_i, \tag{2.15}$$

where $\hat{d}_i^{\dagger}$ and $\hat{d}_i$ are the fermionic creation and annihilation operators for an electron in state i. The composite index i includes the electron's spin, band, and momentum.

In the case of two-dimensional materials like TMDs, the electronic behaviour is constrained to the 2D plane, which restricts the electron's momentum to this plane. The effective mass and relative energies of the electrons are typically extracted from first-principles calculations, such as density functional theory (DFT), to accurately describe the band structure and the role of electrons in determining the material's optical and electronic properties, in particular from Ref. [119].

Phonons

Phonons represent the quanta of lattice vibrations in a crystal and play a crucial role in the relaxation dynamics of electrons and excitons by assisting them in reaching thermal equilibrium. In the context of exciton-polaritons, phonons are vital in facilitating energy dissipation and momentum scattering, allowing polaritons to interact and relax into lower-energy states.

The phonon dynamics can be described using a free-particle Hamiltonian:

$$\hat{H}_{\mathrm{phon}}^{0} = \sum_{j} \hbar \Omega_j \hat{b}_j^{\dagger} \hat{b}_j, \tag{2.16}$$

where $\hat{b}_j^{\dagger}$ and $\hat{b}_j$ are the bosonic creation and annihilation operators for a phonon in state j, and Ω_j is the corresponding phonon frequency. The index j represents the composite state of the phonon, which includes both the momentum and mode of vibration [110].

The phonon dispersion relation, which characterizes the vibrational modes of the lattice, can be derived by solving the problem of interacting ions in

a periodic structure. Although the full dispersion is generally complex, we often focus on phonons near high-symmetry points in the Brillouin zone, where electronic transitions are most relevant. Phonons in these regions provide the dominant scattering pathways for electrons and excitons [69]. In this work, we primarily consider the optical modes (longitudinal optical (LO), transverse optical (TO), and out-of-plane optical (A_1)) and the acoustic modes (longitudinal acoustic (LA) and transverse acoustic (TA)), as these play key roles in exciton–phonon interactions.

For two-dimensional materials such as transition metal dichalcogenides (TMDs), the low-energy acoustic branches can be approximated by a Debye-like linear dispersion, while the dominant optical phonon energies are well described by an Einstein model [113, 120]. These simplified descriptions are sufficient for capturing the exciton–phonon and electron–phonon scattering processes relevant for relaxation and thermalization [120, 121]. The parameters entering these models, such as sound velocities and characteristic phonon energies, are obtained from *ab initio* calculations as reported in Ref. [122].

Photons: Inner-Cavity Photons

In a Fabry-Perot cavity, photons are confined between two highly reflective mirrors, allowing the formation of discrete photon modes. These cavity photons play a crucial role in light-matter interactions, especially in systems like exciton-polaritons, where strong coupling between the cavity photons and excitons gives rise to hybrid quasiparticles. The free Hamiltonian describing photons in the cavity is given by:

$$\hat{H}^0_{\text{phot}} = \sum_{\sigma,\mathbf{k}} \hbar\omega_{\sigma\mathbf{k}} \hat{a}^\dagger_{\sigma\mathbf{k}} \hat{a}_{\sigma\mathbf{k}}, \tag{2.17}$$

where $\hat{a}^\dagger_{\sigma\mathbf{k}}$ and $\hat{a}_{\sigma\mathbf{k}}$ are the bosonic creation and annihilation operators for a photon in mode σ with wavevector $\mathbf{k}$, and $\omega_{\sigma\mathbf{k}}$ is the frequency of the photon in this mode. This quantized photon field represents the electromagnetic modes within the cavity, with each mode corresponding to a specific quantized wave vector and polarization state. We restrict the analysis to the fundamental cavity mode, assuming higher-order modes are spectrally well separated and weakly coupled to excitons. The cavity confines the photons to discrete frequencies determined by the boundary conditions imposed by the mirrors. In the ideal case, these photon modes form a discrete set of energy levels, which are important in the interaction with excitons confined within the

monolayer of TMD. [56, 84]. The photon frequency depends on the cavity length and the refractive index of the materials within the cavity [107].

Photon Bath: Outer-Cavity Photons
Outer-cavity photons, or the photon bath, play a role in mediating the interaction between the cavity mode and the external environment. This coupling is central to understanding the radiative properties and dynamics of cavity systems.

The Hamiltonian governing the photon bath for outer-cavity photons is given by

$$\hat{H}_{\text{bath}} = \hbar \sum_{k} \int d\omega \, \omega(k) \hat{\mathcal{B}}^{\dagger}_{k,\omega} \hat{\mathcal{B}}_{k,\omega}, \tag{2.18}$$

with

$$[\hat{\mathcal{B}}_{k,\omega}, \hat{\mathcal{B}}^{\dagger}_{k',\omega'}] = \delta_{\mathbf{k},\mathbf{k}'} \delta(\omega - \omega'), \tag{2.19}$$

where $\hat{\mathcal{B}}^{\dagger}_{k,\omega}$ and $\hat{\mathcal{B}}_{k,\omega}$ are the creation and annihilation operators for photons in the external bath, with momentum k and frequency ω [108]. This Hamiltonian represents a continuum of external photon modes acting as an environmental reservoir, whose coupling to the cavity mode gives rise to radiative decay and input–output dynamics.

Electron-Electron or Coulomb interaction
The electron-electron interaction plays a fundamental role in shaping the electronic properties of materials, as it significantly modifies the electronic energy landscape [109, 112]. In particular, the Coulomb interaction between electrons in the conduction band and holes in the valence band leads to the formation of bound electron-hole pairs known as excitons [69, 123]. A hole represents the absence of an electron in the valence band and behaves as a positively charged quasiparticle within the material. These excitonic states are energetically favourable due to the strong Coulomb attraction, especially in two-dimensional materials like transition metal dichalcogenides, where the reduced dimensionality enhances the interaction strength [16, 73, 74, 124]. The unique electronic properties of TMDs, combined with the reduced dielectric screening in two-dimensional systems, lead to large exciton binding energies, often on the order of hundreds of meV.

The electron-electron interaction is described by the following Hamiltonian:

$$\hat{H}_{\text{e-e}} = \frac{1}{2} \sum_{ij,\mathbf{k}\mathbf{k}'\mathbf{q}} V_{\mathbf{q}} \hat{c}^{\dagger}_{i,\mathbf{k}+\mathbf{q}} \hat{c}^{\dagger}_{j,\mathbf{k}'-\mathbf{q}} \hat{c}_{j,\mathbf{k}'} \hat{c}_{i,\mathbf{k}} \tag{2.20}$$

where $\hat{c}^{\dagger}$ and $\hat{c}$ represent the fermionic creation and annihilation operators, respectively. The Coulomb matrix element $V_{\mathbf{q}}$ accounts for the strength of the interaction between particles in states i and j. The indices $\mathbf{k}$ and $\mathbf{q}$ represent the momenta of the involved electrons. The electron-electron interaction in two-dimensional materials like TMDs is typically modelled using the Rytova-Keldysh potential, which accurately captures the impact of the surrounding dielectric environment on the Coulomb interaction [125–127]. This potential is essential for understanding the screening effects in low-dimensional systems, particularly in the presence of encapsulating layers or substrates that alter the dielectric landscape.This potential is written as [128]

$$V_{\mathbf{q}} = \frac{e^2}{2\epsilon_0(\epsilon_1 + \epsilon_2)\, L^2} \frac{1}{|\mathbf{q}|(1 + r_0|\mathbf{q}|)},$$

where: e is the elementary charge, ϵ_0 is the vacuum permittivity, ϵ_1 and ϵ_2 are the dielectric constants of the surrounding media, r_0 is the screening length, and L^2 is the system's size. The Coulomb interaction is treated within the static Rytova–Keldysh model, which assumes spatially homogeneous dielectric screening and neglects frequency-dependent screening effects. This is appropriate for the low-energy excitonic regime considered here. This approximation holds well for many practical scenarios where low-energy interactions dominate the physics of the system [111, 125, 126].

Electron-Phonon Interaction

In a solid, electrons interact with the periodic potential created by the vibrating ions of the crystal lattice. These vibrations, quantized as phonons, lead to the scattering of electrons, enabling transitions between different electronic states. The electron-phonon interaction plays a fundamental role in determining many properties of materials, such as electrical conductivity and thermalization dynamics [112, 129, 130]. It is particularly important in two-dimensional materials, where the reduced dimensionality enhances certain scattering processes [122, 131]. This interaction facilitates energy exchange between the electronic and lattice subsystems, significantly affecting the relaxation processes of excited states [132, 133].

The Hamiltonian describing the electron-phonon interaction is given by

$$\hat{H}_{\text{e-phon}} = \sum_{ijl} \left(g_{lij} a_i^\dagger a_j \hat{b}_l + g_{lij}^* a_j^\dagger a_i \hat{b}_l^\dagger \right), \tag{2.21}$$

where $a_i^\dagger$ and a_j are the electron creation and annihilation operators, and $v_l^\dagger$ and $\hat{b}_l$ are the phonon creation and annihilation operators. The prefactor appearing in the electron–phonon coupling originates from the quantization of lattice displacements. In second quantization, the displacement field associated with a phonon mode q is expressed as

$$g_{lij} = \sqrt{\frac{\hbar}{2\rho A \Omega_l}} \langle i | \Delta V_l | j \rangle, \tag{2.22}$$

where ρ is the mass density, A the normalization area, and Ω_l the phonon frequency. This factor corresponds to the zero-point displacement amplitude of the lattice vibration. The electron–phonon coupling can therefore be viewed as the product of the deformation potential (energy change per unit displacement) and the quantized lattice displacement, ensuring that the resulting coupling constant carries units of energy. Finally, we have the ΔV_l as the scattering potential. The scattering potential is treated within the deformation potential approximation, retaining the zeroth- and first-order contributions in momentum. The corresponding deformation potential parameters are obtained from *ab initio* calculations reported in Ref. [112, 122].

These equations capture the essential dynamics of electron-phonon interaction, where phonons mediate transitions between electronic states through the emission and absorption of vibrational energy.

Electron-Photon Interaction

The interaction between electrons and photons is fundamental to the optical properties of two-dimensional materials, such as transition metal dichalcogenides [74]. This interaction can be described using the minimal coupling formalism, where the vector potential of the electromagnetic field modifies the electron's canonical momentum [134–136].

$$\hat{H} = \frac{1}{2m} \left(\mathbf{p} + e\mathbf{A} \right)^2 + V(\mathbf{r}), \tag{2.23}$$

where $\mathbf{p}$ is the electron momentum operator, e is the electron charge, m is the electron mass, $\mathbf{A}$ is the vector potential of the electromagnetic field, and $V(\mathbf{r})$ is the potential due to the lattice. Expanding this expression yields the electron-photon interaction term.

The Hamiltonian for electron-photon interaction can be expressed as

$$\hat{H}_{\text{e-phot}} = \frac{e}{m} \sum_{ij} \mathbf{M}_{ij} \cdot \mathbf{A}(t)\, \hat{a}_i^\dagger \hat{a}_j, \tag{2.24}$$

where $\hat{a}_i^\dagger$ and $\hat{a}_j$ represent electron creation and annihilation operators, respectively, and $\mathbf{M}_{ij} = \langle i|\nabla|j\rangle$ is the optical matrix element governing the probability of electronic transitions between states i and j. Here, $\mathbf{A}(t)$ denotes the time-dependent vector potential, representing the electromagnetic field interacting with the electrons. Expanding the vector potential in terms of photon operators yields

$$\mathbf{A}(\mathbf{r}, t) \to \hat{\mathbf{A}}(\mathbf{r}, t) = \sum_{\sigma, \mathbf{k}} \sqrt{\frac{\hbar}{2\epsilon_0 L^3 \omega_k}}\, \mathbf{e}_{\sigma\mathbf{k}} \left(\hat{c}_{\sigma\mathbf{k}}(t) e^{i\mathbf{k}\cdot\mathbf{r}} + \text{h.a.} \right), \tag{2.25}$$

where $\hat{c}_{\sigma\mathbf{k}}$ and $\hat{c}_{\sigma\mathbf{k}}^\dagger$ are photon annihilation and creation operators in mode σ with wavevector $\mathbf{k}$, $\mathbf{e}_{\sigma\mathbf{k}}$ is the polarization vector, and $\omega_k = c|\mathbf{k}|$ is the photon frequency. The term h.a. stands for the Hermitian adjoint, representing the complex conjugate and transpose of the preceding term. Using this quantized form of the vector potential, the electron-photon interaction Hamiltonian becomes

$$\hat{H}_{\text{e-phot}} = \sum_{ij,\sigma,\mathbf{k}} g_{\sigma\mathbf{k}}^{ji} \hat{a}_j^\dagger \hat{a}_i \hat{c}_{\sigma\mathbf{k}} + \text{h.a.}, \tag{2.26}$$

where the coupling constant, often referred to as the oscillator strength, is given by

$$g_{\sigma\mathbf{k}}^{ji} = \frac{e}{m} \sqrt{\frac{\hbar}{2\epsilon_0 L^3 \omega_k}}\, \mathbf{e}_{\sigma\mathbf{k}} \cdot \mathbf{M}_{ji}. \tag{2.27}$$

This Hamiltonian describes the absorption (annihilation of a photon with $\hat{c}_{\sigma\mathbf{k}}$) and emission (creation of a photon with $\hat{c}_{\sigma\mathbf{k}}^\dagger$) processes accompanied by

electronic transitions between states i and j. The electron-photon matrix element $g^{ji}_{\sigma\mathbf{k}}$ determines the strength of this coupling and thus the likelihood of optical transitions.

In this work, we focus primarily on inter-band transitions, where electrons are excited from the valence band to the conduction band through photon absorption. This process is central to the optical absorption properties of TMDs [7, 137]. The interaction described by this Hamiltonian enables an external electromagnetic field to induce electronic transitions between different energy bands, leading to phenomena such as exciton formation, which plays a key role in light-matter interactions within these materials [124].

Inner-Outer Cavity Photon Interaction

The interaction between photons confined within the cavity and those in the external radiation field is central to describing radiative decay and input–output processes in cavity systems [103]. Mediated by the cavity mirrors, this coupling allows photons to escape into the external environment, enabling the control and measurement of the system's optical response. It forms the basis of quantum optical treatments of open cavity systems, particularly within the input–output formalism [138]. This interaction also influences the dynamics of exciton–polaritons, as the exchange of photons between the cavity and the external field directly affects their behaviour [108, 139].

The Hamiltonian governing this interaction is expressed as seen in the previous section (see equation 2.7)

$$\hat{H}_{\text{phot-bath}} = i\hbar \sum_{j=L,R} \sum_{k} \int \frac{d\omega}{2\pi} \alpha_{j,k}(\omega) \left(\hat{\mathcal{B}}^{\dagger}_{j,\omega k} \hat{c}_k - \hat{\mathcal{B}}_{j,\omega k} \hat{c}\dagger_k \right). \tag{2.28}$$

The coupling parameter $\alpha_{j,k}(\omega)$ defines the interaction strength between the photons inside and outside the cavity. The index j refers to the two sides of the cavity (left and right), and k is the in-plane momentum of the photon, which is conserved in this interaction [108].

This interaction governs the leakage of photons from the cavity into the external environment, which determines the radiative decay rate of the exciton–polaritons [108, 140]. It also enables the coupling of the polaritonic system to external electromagnetic fields, providing experimental access for

optical measurements and control [139]. The interaction between inner- and outer-cavity photons is therefore an integral component in modelling the optical response of polaritons, particularly within input–output approaches used to describe cavity systems [84, 103].

The input–output theory relates the external radiation modes to the intra-cavity fields, allowing one to compute experimentally measurable response functions such as transmission and reflection spectra [105]. This formalism plays an important role in the analysis of exciton–polariton systems, where the coupling to external modes determines the observable optical properties of the quasiparticles inside the cavity.

With the many-particle Hamiltonian formalism established, we next introduce excitons, whose microscopic properties determine how they couple to photons in a microcavity.

2.3 Excitons and the Wannier Equation

The excitonic basis introduced here allows us to transform the electron–hole description into a form suitable for polariton modelling. In particular, it provides access to exciton energies and wavefunctions that determine coupling strengths and scattering pathways analysed in Chapters 3 and 4. In TMDs, the strong Coulomb interaction leads to the formation of deeply bound electron-hole pairs called excitons [123, 141, 142]. When the material absorbs a photon with energy higher than the bandgap, an electron is excited from the valence band to the conduction band, leaving behind a hole. If the electron and hole remain bound due to Coulomb attraction, they form an exciton with an energy slightly below the bandgap, the difference being the exciton binding energy.

Due to their large binding energies, excitons dominate the optical and transport properties of TMDs, even at room temperature [74, 142–145], and exhibit a rich exciton landscape, including both bright and dark states [15, 142]. Bright excitons are optically active and can couple directly to light, while dark excitons are optically inactive due to spin or momentum mismatches between the electron and hole.

The optical response is typically dominated by $1s$ excitons, the lowest-energy excitonic states with no angular momentum nodes. These states are the solutions to the generalized Wannier equation, which describes the relative motion of the electron-hole pair in excitonic systems [73, 74, 124]. Higher excitonic states, such as $2s$ and $2p$, have additional nodes in their wavefunctions and lie at higher energies [124, 146]. The Wannier equation effectively describes the excitonic binding energy and spatial distribution by accounting for the Coulomb interaction between electrons and holes in TMDs, cf. Eq. (2.20), providing a robust framework for analyzing excitonic properties in these materials [69, 123, 147].

2.3.1 Microscopic Polarization and Excitonic Basis

The microscopic polarization, denoted by

$$p^{v\uparrow c\uparrow}_{\mathbf{k}_1\mathbf{k}_2} = \langle \hat{a}^\dagger_{c,\mathbf{k}_2} \hat{a}_{v,\mathbf{k}_1} \rangle,$$

describes the creation of electron-hole pairs, where $\hat{a}^\dagger_{c,\mathbf{k}_2}$ and $\hat{a}_{v,\mathbf{k}_1}$ represent the creation and annihilation operators for conduction and valence band states, respectively. The polarization term $p^{v\uparrow c\uparrow}_{\mathbf{k}_1\mathbf{k}_2}$ encapsulates the electron–hole correlations that underlie the formation of excitonic states [69, 110].

To facilitate the transition from the electron–hole pair representation to an excitonic basis, it is useful to separate the center-of-mass (CoM) motion from the relative motion of the electron and hole. This decoupling is a standard step in deriving the generalized Wannier equation, which captures the binding energy and spatial structure of excitons [123, 141].

The Schrödinger equation for an electron-hole pair with total momentum $\mathbf{Q}$ and relative momentum $\mathbf{q}$ is given by

$$\left(\frac{\hbar^2 Q^2}{2M} + \frac{\hbar^2 q^2}{2m_r} \right) \psi(\mathbf{r}_e, \mathbf{r}_h) - V(\mathbf{r}_e - \mathbf{r}_h)\psi(\mathbf{r}_e, \mathbf{r}_h) = E\,\psi(\mathbf{r}_e, \mathbf{r}_h), \qquad (2.29)$$

where $\mathbf{Q}$ is the center-of-mass momentum, $\mathbf{q}$ is the relative momentum, M is the total mass of the electron-hole pair, m_r is the reduced mass, and $V(\mathbf{r}_e - \mathbf{r}_h)$ is the Coulomb interaction potential between the electron at $\mathbf{r}_e$ and hole at $\mathbf{r}_h$ [69, 110].

We can redefine the polarization in terms of the center-of-mass momentum $\mathbf{Q}$ and the relative momentum $\mathbf{q}$, where

$$\mathbf{Q} = \mathbf{k}_1 + \mathbf{k}_2, \quad \mathbf{q} = \alpha_\nu \mathbf{k}_1 + \beta_\nu \mathbf{k}_2,$$

with α_ν and β_ν determined by the masses of the electron and hole, m_e and m_h, as:

$$\alpha_\nu = \frac{m_h}{m_e + m_h}, \quad \beta_\nu = \frac{m_e}{m_e + m_h}.$$

This transformation enables the excitonic representation

$$p^{v\uparrow c\uparrow}_{\mathbf{qQ}} = \sum_\nu \varphi^\nu_{\mathbf{q}} p^\nu_{\mathbf{Q}}, \tag{2.30}$$

where ν represents the excitonic state, such as the bright KK exciton.

By focusing on the relative motion $\mathbf{q}$ alone, we derive the generalized Wannier equation, which describes the binding energy of the exciton in momentum space

$$\frac{\hbar^2 q^2}{2m_r^\nu}\varphi^\nu_{\mathbf{q}} - \sum_{\mathbf{k}} V^{exc}(\mathbf{k})\varphi^\nu_{\mathbf{q}-\mathbf{k}} = \varepsilon_\nu \varphi^\nu_{\mathbf{q}}, \tag{2.31}$$

where m_r^ν is the reduced exciton mass, and $V^{exc}(\mathbf{k})$ is the screened Coulomb interaction in momentum space [19, 69]. The Wannier equation provides a microscopic description of the excitonic states in a TMD monolayer. It determines the binding energies and wavefunctions of excitons, allowing us to calculate key properties such as their spatial extent and coupling strength with photons

The solutions to this equation provide the exciton eigenenergies ε_ν and eigenfunctions $\varphi^\nu_{\mathbf{q}}$, forming a quantized series of excitonic states (e.g., $1s$, $2s$, etc.) [123]. For this thesis, we only consider the $1s$ exciton states. The exciton center-of-mass dispersion can then be expressed as

$$E^{\mathrm{X}}_{\nu\mathbf{Q}} = E^\nu_g + \varepsilon_\nu + \frac{\hbar^2 Q^2}{2M^\nu}, \tag{2.32}$$

where E^ν_g is the single-particle bandgap corresponding to valley ν [19, 69]. The excitonic basis assumes low excitation density, allowing excitons to be treated as weakly interacting bosonic quasiparticles.

2.3.2 Excitonic Hamiltonian

We have introduced the exciton basis and states, occupied by electron-hole pairs. If we continue working with the electron picture, the calculation of equations of motion becomes complex. Instead, we simplify by focusing on the center-of-mass momentum of the 1s excitons. The excitonic Hamiltonian can be derived using the excitonic expansion scheme [148, 149]. The new operators $\hat{X}^{\dagger}_{\nu\mathbf{Q}}(\hat{X}_{\nu\mathbf{Q}})$ create and annihilate an exciton in state ν with center-of-mass momentum $\mathbf{Q}$. Excitons can be treated as bosons in the low-density limit [69, 126]. The exciton Hamiltonian also includes exciton-photon and exciton-phonon interactions, as discussed in [148, 150]. In order to transition from the electron-hole picture to the excitonic picture, we first start by considering the Hamiltonians for free electrons and holes and their Coulomb interactions.

The total Hamiltonian consists of a free part and an interaction part:

$$\hat{H} = \hat{H}_{\mathrm{e-0}} + \hat{H}_{\mathrm{Coulomb}},$$

where the free electron-hole Hamiltonian is given by equation (2.15) and the corresponding Coulomb interaction (electron-electron or electron-hole) term in equation (2.20)

To transform the Hamiltonian into the excitonic picture, we introduce the electron–hole pair annihilation and creation operators, which combine conduction-band electrons and valence-band holes:

$$\hat{A}_{\mathbf{k}_1\mathbf{k}_2} = \hat{a}^{\dagger}_{c,\mathbf{k}_1}\hat{a}_{v,\mathbf{k}_2}, \qquad \hat{A}^{\dagger}_{\mathbf{k}_1\mathbf{k}_2} = \hat{a}^{\dagger}_{v,\mathbf{k}_2}\hat{a}_{c,\mathbf{k}_1}.$$

In the low-density limit, we approximate the commutator between the electron-hole operators as

$$[\hat{A}_{\mathbf{k}_1\mathbf{k}_2}, \hat{A}^{\dagger}_{\mathbf{k}_3\mathbf{k}_4}] \approx \delta_{\mathbf{k}_1\mathbf{k}_3}\delta_{\mathbf{k}_2\mathbf{k}_4}.$$

This allows us to treat the electron-hole pair operators as bosons, which is valid in the low-excitation limit.

Next, we perform a basis transformation from the electron-hole operators $\hat{A}$ to the exciton operators $\hat{X}$, where the excitonic operators $\hat{X}^{\dagger}_{\nu\mathbf{Q}}$ ($\hat{X}_{\nu\mathbf{Q}}$) create (annihilate) an exciton in state ν with center-of-mass momentum $\mathbf{Q}$. The

excitonic states are a superposition of electron-hole pairs, and the electron-hole pair operator can be expanded into excitonic eigenstates as

$$\hat{A}^{\dagger}_{\mathbf{k}_1\mathbf{k}_2} = \sum_{\nu} \hat{X}^{\dagger}_{\nu,\mathbf{k}_1-\mathbf{k}_2} \varphi_{\nu}(\alpha_{\nu}\mathbf{k}_1 + \beta_{\nu}\mathbf{k}_2),$$

where φ_{ν} represents the excitonic wave function, and α_{ν} and β_{ν} are the weighting factors that describe the electron and hole contributions to the total exciton momentum.

Consequently, the total Hamiltonian in the excitonic basis, neglecting higher-order correlations, becomes the free excitonic Hamiltonian

$$H^0_X = \sum_{\nu,\mathbf{Q}} E^{\mathrm{X}}_{\nu\mathbf{Q}} \hat{X}^{\dagger}_{\nu\mathbf{Q}} \hat{X}_{\nu\mathbf{Q}}. \tag{2.33}$$

The excitonic Hamiltonian captures the internal dynamics of excitons, accounting for their kinetic energy and Coulomb interactions. This framework provides the basis for modelling the interactions of excitons with other quasi-particles, such as photons and phonons.

In addition to the free exciton Hamiltonian, we need to account for interactions with photons and phonons. The exciton-photon interaction is obtained from the change of basis to excitons of the Hamiltonian in equation (2.26) and is described by

$$\hat{H}_{X-c} = \sum_{\nu,\mathbf{Q}} g_{\mathbf{Q}} \left(\hat{c}^{\dagger}_{\mathbf{Q}} \hat{X}_{\nu\mathbf{Q}} + \hat{c}_{\mathbf{Q}} \hat{X}^{\dagger}_{\nu\mathbf{Q}} \right), \tag{2.34}$$

where $g_{\mathbf{Q}}$ is the exciton-photon coupling constant, and $\hat{c}^{\dagger}_{\mathbf{Q}}$ and $\hat{c}_{\mathbf{Q}}$ are the photon creation and annihilation operators.

Repeating the exciton-phonon interaction, which describes scattering between excitons via phonons, starting from equation (2.16, we obtain

$$H_{X-p} = \sum_{\nu\nu',\mathbf{Q},\alpha,\mathbf{q}} \mathcal{D}^{\nu\nu'}_{\alpha\mathbf{q}} \hat{X}^{\dagger}_{\nu,\mathbf{Q}+\mathbf{q}} \hat{X}_{\nu',\mathbf{Q}} \left(\hat{b}^{\dagger}_{\alpha,-\mathbf{q}} + \hat{b}_{\alpha\mathbf{q}} \right), \tag{2.35}$$

where $\mathcal{D}^{\nu\nu'}_{\alpha\mathbf{q}}$ is the exciton-phonon coupling matrix element. The coupling element is expressed as

$$\mathcal{D}^{\nu\nu'}_{\alpha\mathbf{q}} = D^{c}_{\alpha\mathbf{q}} \sum_{\mathbf{k}} \psi^{*\nu}(\mathbf{k}) \psi^{\nu'}(\mathbf{k} + \beta_{\nu}\mathbf{q}) - D^{v}_{\alpha\mathbf{q}} \sum_{\mathbf{k}} \psi^{*\nu}(\mathbf{k}) \psi^{\nu'}(\mathbf{k} - \alpha_{\nu}\mathbf{q}). \tag{2.36}$$

Here, $D^c_{\alpha\mathbf{q}}$ and $D^v_{\alpha\mathbf{q}}$ represent the electron-phonon coupling constants in the conduction and valence bands, respectively, and $\psi^{*\nu}(\mathbf{k})$ is the excitonic wave function.

2.4 Exciton-Polaritons and Hopfield Transformation

In this section, we introduce the Hopfield transformation, which describes the mixing of excitonic and photonic components in exciton-polaritons. We begin with the polaritonic Hamiltonian and derive analytical expressions for the polariton energies and the corresponding Hopfield coefficients, which quantify the exciton and photon contributions to the polariton states.

This analysis is central to the thesis, which explores exciton-polaritons in an hBN-encapsulated TMD monolayer integrated into an optical microcavity. The system, as illustrated in Fig. 2.3, includes both inner-cavity photons (confined within the cavity) and outer-cavity photons (coupled to the external environment). In this framework, we combine the density matrix formalism with the Hopfield approach [59, 78] to comprehensively characterize the exciton-photon coupling in the system. The works [151–153] provide additional context for the strong coupling regime and its observable consequences.

The total Hamiltonian, which describes the formation of polaritons, is composed of three main parts: the free exciton Hamiltonian, the free photon Hamiltonian, and the exciton-photon interaction Hamiltonian. The system Hamiltonian can be written as

$$\begin{aligned}\hat{H}_{\mathrm{X-pol}} &= \hat{H}^0_{\mathrm{X}} + \hat{H}^0_{\mathrm{phot}} + \hat{H}_{\text{X-phot}} \\ &= \sum_{\nu\mathbf{k}} E^{\mathrm{X}}_{\nu\mathbf{k}} \hat{X}^\dagger_{\nu\mathbf{k}} \hat{X}_{\nu\mathbf{k}} + \sum_{\mathbf{k}} E^{\mathrm{c}}_{\mathbf{k}} \hat{c}^\dagger_{\mathbf{k}} \hat{c}_{\mathbf{k}} + \sum_{\nu,\mathbf{Q}} g_{\mathbf{Q}} \left(\hat{c}^\dagger_{\mathbf{Q}} \hat{X}_{\nu\mathbf{Q}} + \hat{c}_{\mathbf{Q}} \hat{X}^\dagger_{\nu\mathbf{Q}} \right).\end{aligned} \tag{2.37}$$

We focus on the strong-coupling regime, where the exciton-photon coupling strength $g_{\mathbf{k}}$ exceeds the decay rates of the cavity and exciton. In this regime,

polaritons form as new eigenmodes of the system

$$\hat{Y}^n_{\mathbf{k}} = h^n_{\mathrm{X},\mathbf{k}}\hat{X}_{\mathbf{k}} + h^n_{\mathrm{c},\mathbf{k}}\hat{c}_{\mathbf{k}}, \tag{2.38}$$

where $h^n_{\mathrm{X},\mathbf{k}}$ and $h^n_{\mathrm{c},\mathbf{k}}$ are the Hopfield coefficients that determine the exciton and photon content of the polariton states. The Hopfield transformation assumes linear coupling between excitonic and photonic modes and neglects nonlinear interaction terms, restricting the analysis to the low-excitation regime. The polariton description relies on a separation of timescales between fast photonic dynamics and slower excitonic relaxation processes, allowing the hybrid light–matter states to be treated as well-defined quasiparticles. Applying the Hopfield transformation to the Hamilton operator, we obtain [59, 78]

$$\hat{H}_{pol} = \sum_{\mathbf{k},n} E^n_{\mathbf{k}}\hat{Y}^{n\dagger}_{\mathbf{k}}\hat{Y}^n_{\mathbf{k}}, \tag{2.39}$$

yielding the free polaritonic Hamiltonian with $\hat{Y}^{n\dagger}_{\mathbf{k}}(\hat{Y}^n_{\mathbf{k}})$ as the polariton creation (annihilation) operators. Here, $E^n_{\mathbf{k}}$ represents the polariton energy, including the lower (LP) and upper polariton (UP) branches separated by the Rabi splitting $\hbar\Omega_R = E^{UP}_0 - E^{LP}_0$ at $\mathbf{k} = 0$. When the system is resonant ($E^{\mathrm{X}}_0 = E^{\mathrm{c}}_0$), the exciton and photon states hybridize, producing two polariton branches with an avoided crossing in the energy dispersion and are visualized in optical spectra at strong enough coupling g [151–153]. Throughout this work we consider the low-excitation regime, where nonlinear exciton–exciton interactions and phase-space filling effects are negligible, allowing a linearized treatment of light–matter coupling.

Returning to the total Hamiltonian in the exciton basis, adding to equation (2.37) the terms to include interaction with phonons and with the outer-cavity bath

$$\begin{aligned}\hat{H}_{\mathrm{total}} = \hat{H}_{pol} &+ \sum_{\mathbf{q}} E^b_{\alpha\mathbf{q}}\hat{b}^\dagger_{\alpha\mathbf{q}}b_{\alpha\mathbf{q}} + \sum_{j=L,R}\sum_{\mathbf{k}}\int_0^\infty d\omega h\omega(\mathbf{k})\hat{\mathcal{B}}^\dagger_{j\mathbf{k}\omega}\hat{\mathcal{B}}_{j\mathbf{k}\omega} \\ &+ \sum_{\nu\nu'\mathbf{k}\alpha\mathbf{q}} \mathcal{D}^{\nu\nu'}_{\alpha\mathbf{q}}\hat{X}^\dagger_{\nu\mathbf{k}+\mathbf{q}}\hat{X}_{\nu'\mathbf{k}}(\hat{b}^\dagger_{\alpha,-\mathbf{q}} + \hat{b}_{\alpha\mathbf{q}}) + \\ &+ i\hbar\sum_{j=L,R}\sum_{\mathbf{k}}\int_0^\infty \frac{d\omega}{2\pi}\alpha_{j,\mathbf{k}}(\omega)[\hat{\mathcal{B}}^\dagger_{j\omega\mathbf{k}}\hat{c}_{\mathbf{k}} - \hat{\mathcal{B}}_{j\omega\mathbf{k}}\hat{c}^\dagger_{\mathbf{k}}],\end{aligned} \tag{2.40}$$

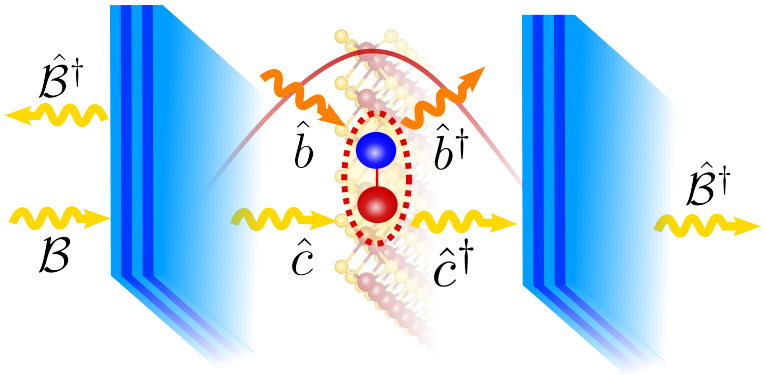


Figure 2.3: Schematic illustration of a TMD monolayer in a Fabry-Perot cavity with the fundamental cavity mode represented by the red curve. TMD excitons-polaritons interact with photons and phonons as indicated by the creation (annihilation) operators for photons ($\hat{c}^\dagger(\hat{c})$) and phonons ($\hat{b}^\dagger(\hat{b})$). The cavity system interacts with the outside world via the operators $\hat{\mathcal{B}}^\dagger(\hat{\mathcal{B}})$.

where we quantize separately a single internal cavity mode of a Fabry-Perot resonator and the external radiation fields, which are split into two sets of continuum modes corresponding to the left and right of the cavity (Fig.2.3).

Applying the Hopfield transformation to the Hamilton operator of Eq. (2.40) yields

$$\begin{aligned}\hat{H}_{\text{total-pol}} = &\sum_{\mathbf{k},n} E^n_{\mathbf{k}} \hat{Y}^{n\dagger}_{\mathbf{k}} \hat{Y}^n_{\mathbf{k}} + \hat{H}_{\text{phon}-0} + \hat{H}_{\text{bath}} + \\ &+ \sum_{\mathbf{k}\alpha\mathbf{q}nn'} \tilde{\mathcal{D}}^{n'n}_{\mathbf{k}\alpha\mathbf{q}} \left(\hat{b}^\dagger_{\alpha,-\mathbf{q}} + \hat{b}_{\alpha\mathbf{q}}\right) \hat{Y}^{n'\dagger}_{\mathbf{k}+\mathbf{q}} \hat{Y}^n_{\mathbf{k}} + \\ &+ i\hbar \sum_{\mathbf{k},n,j} \int_0^\infty \frac{d\omega}{2\pi} \alpha_{j\mathbf{k}}(\omega) \left(h^n_{C,\mathbf{k}} \hat{\mathcal{B}}^\dagger_{j\mathbf{k}\omega} \hat{Y}^n_{\mathbf{k}} - h^{n*}_{C,\mathbf{k}} \hat{\mathcal{B}}_{j\mathbf{k}\omega} \hat{Y}^{n\dagger}_{\mathbf{k}} \right). \end{aligned} \tag{2.41}$$

with momentum k running now over all the Brillouin zone. Here, the first term is the free polaritonic Hamiltonian, which we described in equation (2.39). The terms that described the free-phonons and the photon bath do not change under the Hopfield transformation, for convenience of notation we just refer as $\hat{H}_{\text{phon}-0}$ and $\hat{H}_{\text{bath}}$, respectively. When it comes to the polariton-phonon interaction, only the excitonic part of the polariton couples with phonons. Hence, we obtain a matrix element $\tilde{D}$ related to the exciton-phonon

coupling via $\tilde{\mathcal{D}}^{i',i}_{\mathbf{Q}',\mathbf{Q},\mathbf{q}} = h^{i'*}_{X,\mathbf{Q}'}\mathcal{D}_{\mathbf{q}}h^{i}_{X,\mathbf{Q}}$ [154], or simply put the exciton-phonon coupling is re-normalized by the excitonic Hopfield coefficient. Finally, the interaction of exciton-polaritons with the photon bath is mediated by the photonic Hopfield coefficient $h^{i}_{C,\mathbf{Q}}$. Hence, we have two main interactions with polariton mechanisms, and according to the part of the exciton-polariton that interacts with the other particles, the proper Hopfield coefficient mediates this interaction.

In this section, we established the theoretical framework for describing exciton-polaritons using the Hopfield transformation. The derived polariton Hamiltonian and analytical expressions for the Hopfield coefficients provide a robust toolset to quantify exciton-photon interactions. This is the foundation for subsequent sections that address polariton dispersion, group velocity, and dynamic properties.

Polariton Dispersion

The Hopfield transformation provides the formalism to describe exciton-polaritons as hybrid light-matter states. Building on this, we now derive the polariton energy dispersion, illustrating the energy separation into lower and upper polariton branches and its dependence on exciton-photon coupling. Hence, we investigate the change of the excitonic band structure in the presence of a strong coupling regime. Both polariton energies $E^{n}_{\mathbf{k}}$ (Figure 2.4(a)) and Hopfield coefficients $h^{n}_{\mathrm{X},\mathbf{k}}$ and $h^{n}_{\mathrm{c},\mathbf{k}}$ (Figure 2.4(b)) can be obtained analytically (with subscript X and c referring to exciton and intra-cavity photon component, respectively) [59]

$$E^{\mathrm{LP/UP}}_{\mathbf{k}} = \frac{1}{2}E^{\mathrm{X}}_{\mathbf{k}} + \frac{1}{2}E^{\mathrm{c}}_{\mathbf{k}} \mp \frac{1}{2}\sqrt{4g^{2}_{\mathbf{k}} + \Delta E^{2}_{\mathbf{k}}} \tag{2.42}$$

with $\Delta E_{\mathbf{k}} = E^{\mathrm{X}}_{\mathbf{k}} - E^{\mathrm{c}}_{\mathbf{k}}$ and the Hopfield coefficients $h^{\mathrm{LP}}_{\mathrm{X},\mathbf{k}} = h^{\mathrm{UP}}_{\mathrm{c},\mathbf{k}} = C_{+,\mathbf{k}}$ and $h^{LP}_{\mathrm{c},\mathbf{k}} = -h^{UP}_{\mathrm{X},\mathbf{k}} = C_{-,\mathbf{k}}$ [59, 78], where

$$|C_{\pm,\mathbf{k}}|^{2} = \frac{1}{2}\left(1 \pm \Delta E_{\mathbf{k}}\left[\Delta E^{2}_{\mathbf{k}} + 4g^{2}_{\mathbf{k}}\right]^{-\frac{1}{2}}\right). \tag{2.43}$$

For a vanishing exciton-phonon coupling $g_{\mathbf{k}}$, the lower/upper polariton branch in the light-cone approaches the cavity and exciton energy (thin yellow and

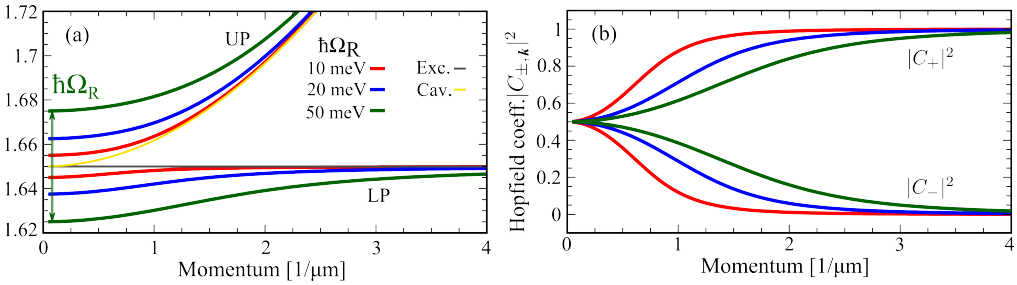


Figure 2.4: (a) Polariton dispersion and (b) Hopfield coefficients for three typical values of Rabi splitting. The bare exciton and photon energy are shown for comparison with thin grey and yellow lines, respectively.

grey lines in Fig. 2.4(a)), respectively. The Hopfield coefficients quantify the excitonic and photonic contributions to each polariton state. They determine how polaritons interact with their environment, as different interactions (e.g., with phonons or photons) depend on these contributions.

Figure 2.4(a) illustrates the polariton dispersion for three values of the Rabi splitting representing different exciton-photon coupling strengths. The avoided crossing in the energy dispersion, characteristic of strong coupling, is evident. This figure visually demonstrates how the lower and upper polariton branches emerge as hybrid states of excitons and photons, with the energy separation determined by the Rabi splitting. We investigate the polariton dispersion for typical Rabi splitting values of $\hbar\Omega_{\mathrm{R}}$ =10, 25, 50 meV [6], which are larger than the non-radiative exciton linewidth (typically a few meV at low temperatures for hBN-encapsulation TMDs [19, 61, 155]) and the cavity linewidth (ranging from the meV [5] down to the μeV range [85, 156]), thus allowing for strong-coupling regime [59]. At larger momenta, the LP and UP branches merge with the exciton and photon dispersion, respectively. The larger $\hbar\Omega_{\mathrm{R}}$, the higher the momentum values at which this occurs, cf. Fig. 2.4(a). Polaritons are coherent superpositions of excitonic and photonic states with the Hopfield coefficients defining the weights of the single constituents, cf. Fig. 2.4(b). The coefficient $|C_{+,\mathbf{k}}|^2$ gives the exciton content of the lower polariton and the photon content of the upper polariton, i.e. for $|C_{+,\mathbf{k}}|^2$ =1 the LP state $|\mathrm{LP},\mathbf{k}\rangle = \hat{Y}^{\mathrm{LP}\dagger}_{\mathbf{k}}|0\rangle$ coincides with the exciton state $|\mathrm{X},\mathbf{k}\rangle$ and the UP state $|\mathrm{UP},\mathbf{k}\rangle$ corresponds to the photon state $|\mathrm{c},\mathbf{k}\rangle$.
In this section, we analyzed the polariton dispersion relations, illustrating

the energy separation of the lower and upper polariton branches due to Rabi splitting. This behaviour reflects the hybridization of excitonic and photonic states, forming the basis for understanding polariton-mediated processes in TMD-based microcavities.

Polariton Group Velocity and Occupation

The polariton energy dispersion not only defines the polariton states but also determines their transport properties, such as group velocity and band occupation. These properties are relevant for understanding polariton-mediated energy and information transfer, which we explore next. From the polariton energies (2.42), we can calculate the polariton group velocity and the polariton band occupation. In Fig. 2.5, we consider the polariton group velocity given by

$$v_{\mathbf{k}}^{n} = \hbar^{-1} \frac{dE_{\mathbf{k}}^{n}}{d\mathbf{k}}, \tag{2.44}$$

in particular focusing on the lower polariton branch, since the upper one has a negligible occupation. We consider the two cases of Rabi splitting $\hbar\Omega_{\mathrm{R}}$=25, 50 meV for the polariton group velocity and compare it with the excitonic group velocity $v_k^X = \hbar k/M_X$, where M_X is the exciton mass.

We find that the polariton group velocity is approximately 4 to 5 orders of magnitude larger than the excitonic one for small momenta within the light-cone, cf. Fig. 2.5.This enhancement is due to the flatter exciton dispersion compared to the hybridized polariton states, underscoring the potential of polaritons for long-range ballistic transport. Due to the rapidly changing polariton dispersion, we find group velocities in the range of 10 μm/ps, thus principally opening the possibility of ballistic polariton propagation for distances in the tens of microns. This has recently indeed been observed in space- and angle-resolved photoluminescence experiments on a WS_2 monolayer in a distributed Bragg reflector cavity [87]. In addition to the remarkable magnitude difference, the group velocity for polaritons also has a qualitatively different momentum dependence. It shows a maximum in correspondence to the inflexion point in the lower polariton branch and decreases toward the excitonic velocity for momenta of several $\mu\mathrm{m}^{-1}$. In short, two subsets of states with considerably different group velocities coexist in a cavity: The fast ones located within the light-cone and the slow ones outside of it coinciding with conventional excitons. Next, we overlay the occupation of the lower polariton

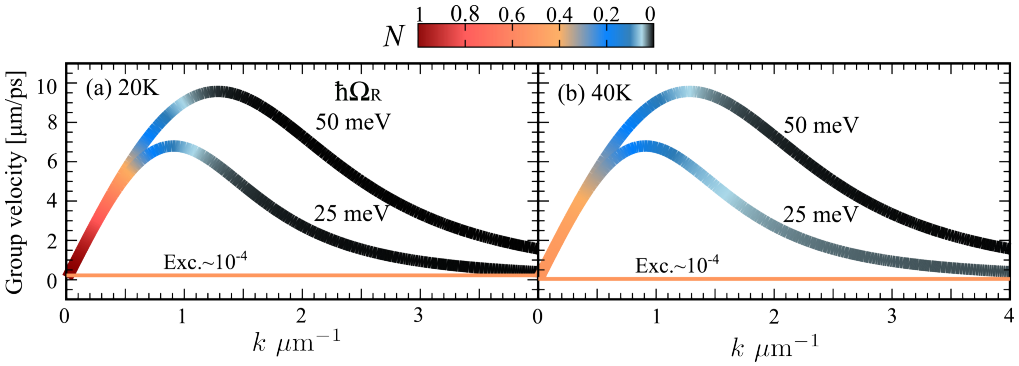


Figure 2.5: Lower polariton group velocity at (a) T=20 K and (b) T=40 K for two different Rabi splittings of $\hbar\Omega_R$ = 25 and 50 meV. The corresponding band occupation is overlaid on the polariton dispersion, see the colour map. For comparison, the excitonic group velocity is shown by the thin orange line.

state on the line displaying the group velocity (reddish colours denote large occupation), cf. Fig. 2.5, assuming a thermalized Boltzmann distribution

$$f^n_{\mathbf{k}} \propto e^{-E^n_{\mathbf{k}}/k_B T}. \tag{2.45}$$

While the excitonic occupation is momentum-independent in the considered range of momenta (cf. the thin orange line in Fig. 2.5), strong variations are observed for polaritons. At 20 K, the occupation of the states at larger momenta is decreased by two orders of magnitude when compared to the exciton case for both considered Rabi splittings ($f^{\mathrm{LP}}/f^{\mathrm{X}} \approx 10^{-5}$ at $k \approx 4\ \mu\mathrm{m}^{-1}$), cf. orange vs black colour in Fig. 2.5. The curvature of the polariton branch induces a significant decrease in the occupation of the slow quasi-excitonic states at large momenta, as the energetically lower states at $k \approx 0$ are more efficiently populated. Increasing the temperature, the population of the former starts to increase, particularly for the smaller Rabi splitting of 25 meV, cf. Fig. 2.5(b). Regarding the behaviour at smaller momenta, we see that at 20 K, the occupation of states with the maximum group velocity is negligible for $\hbar\Omega_{\mathrm{R}}$=50 meV (black colour at approximately $k \approx 1.3\ \mu\mathrm{m}^{-1}$). However, when increasing the temperature to 40 K, we find a considerable occupation even at these states, indicating the possibility of a strongly accelerated polariton diffusion. We will discuss the diffusion coefficient in chapter 3.

Here, we demonstrated that polaritons exhibit significantly enhanced group

velocities compared to excitons, enabling ballistic transport over micron-scale distances. The unique band occupation of polaritons underpins their potential for novel optoelectronic applications. Having examined the group velocity and occupation of polaritons, we turn to their spatiotemporal dynamics. The diffusion coefficient provides a measure of how polaritons spread in space, offering insights into their transport behaviour under steady-state conditions.

2.5 Diffusion Coefficient for Polaritons

To describe polariton transport in the steady-state regime, we employ a semiclassical kinetic approach based on the Boltzmann equation. The derivation follows the standard semiclassical transport theory based on the linearized Boltzmann equation within the relaxation-time approximation [112, 113, 157].The diffusion description assumes incoherent scattering dominated by phonon interactions and neglects localization effects arising from strong disorder. We consider the phase-space distribution function $f(\mathbf{k}, \mathbf{r}, t)$ and expand it around a local quasi-equilibrium distribution [158, 159]

$$f(\mathbf{k}, \mathbf{r}, t) = f_0(\mathbf{k}, \mathbf{r}, t) + \delta f(\mathbf{k}, \mathbf{r}, t), \tag{2.46}$$

where f_0 denotes a local thermal distribution and δf represents small deviations induced by spatial gradients.

The particle current is given by

$$\mathbf{J}(\mathbf{r}, t) = \frac{1}{A} \sum_{n,\mathbf{k}} \mathbf{v}_{\mathbf{k}}^n f(\mathbf{k}, \mathbf{r}, t), \tag{2.47}$$

where $\mathbf{v}_{\mathbf{k}}^n = \nabla_{\mathbf{k}} E_{\mathbf{k}}^n / \hbar$ is the polariton group velocity and A is the normalization area. Since f_0 is isotropic in momentum space, it does not contribute to a net current, yielding

$$\mathbf{J}(\mathbf{r}, t) = \frac{1}{A} \sum_{n,\mathbf{k}} \mathbf{v}_{\mathbf{k}}^n \, \delta f(\mathbf{k}, \mathbf{r}, t). \tag{2.48}$$

The evolution of the distribution function is governed by the Boltzmann equation

$$\partial_t f + \mathbf{v}_{\mathbf{k}}^n \cdot \nabla_{\mathbf{r}} f = \left. \frac{df}{dt} \right|_{\text{scatt}}. \tag{2.49}$$

Within the relaxation-time approximation, the scattering term is written as

$$\left.\frac{df}{dt}\right|_{\text{scatt}} = -\frac{\delta f}{\tau_{\mathbf{k}}}, \tag{2.50}$$

where $\tau_{\mathbf{k}}$ denotes the momentum-dependent relaxation time.

Assuming a steady-state regime ($\partial_t f \approx 0$) and retaining only linear terms in spatial gradients, we obtain

$$\delta f(\mathbf{k}, \mathbf{r}) = -\tau_{\mathbf{k}}\, \mathbf{v}_{\mathbf{k}}^n \cdot \nabla_{\mathbf{r}} f_0(\mathbf{k}, \mathbf{r}). \tag{2.51}$$

Substituting this expression into the current yields

$$\mathbf{J}(\mathbf{r}) = -\frac{1}{A} \sum_{n,\mathbf{k}} \tau_{\mathbf{k}}\, \mathbf{v}_{\mathbf{k}}^n \left(\mathbf{v}_{\mathbf{k}}^n \cdot \nabla_{\mathbf{r}} f_0\right). \tag{2.52}$$

Assuming isotropic dispersion and scattering allows the tensor average

$$v_i v_j \to \frac{|v|^2}{d} \delta_{ij}, \tag{2.53}$$

where d denotes the dimensionality of the system. The current then reduces to Fick's law

$$\mathbf{J} = -D\, \nabla_{\mathbf{r}} N(\mathbf{r}), \tag{2.54}$$

with the diffusion coefficient given by

$$D = \frac{1}{dA} \sum_{n,\mathbf{k}} |v_{\mathbf{k}}^n|^2 \tau_{\mathbf{k}} \left(-\frac{\partial f_0}{\partial E_{\mathbf{k}}^n}\right) \frac{\partial \mu}{\partial N}. \tag{2.55}$$

To obtain a more explicit form of the diffusion coefficient, we consider the low-density (Boltzmann) limit, where the equilibrium distribution reads

$$f_0(\mathbf{k}) \approx \exp\left(-\frac{E_{\mathbf{k}}^n - \mu}{k_B T}\right). \tag{2.56}$$

In this regime, the energy derivative simplifies to

$$-\frac{\partial f_0}{\partial E_{\mathbf{k}}^n} = \frac{f_0}{k_B T}. \tag{2.57}$$

Furthermore, for a dilute classical gas the thermodynamic relation

$$\frac{\partial \mu}{\partial N} = \frac{k_B T}{N} \tag{2.58}$$

holds, yielding

$$\left(-\frac{\partial f_0}{\partial E^n_{\mathbf{k}}}\right) \frac{\partial \mu}{\partial N} = \frac{f_0}{N}. \tag{2.59}$$

The diffusion coefficient therefore reduces to

$$D = \frac{1}{dV} \sum_{n,\mathbf{k}} |v^n_{\mathbf{k}}|^2 \tau_{\mathbf{k}} \frac{f_0(\mathbf{k})}{N}. \tag{2.60}$$

Introducing the scattering rate $\Gamma^n_{\mathbf{k}} = \hbar/\tau_{\mathbf{k}}$ and expressing the normalized distribution as $f^n_{\mathbf{k}}/\mathcal{Z}$ finally leads to

$$D = \frac{\hbar}{d} \sum_{n,\mathbf{k}} \frac{|v^n_{\mathbf{k}}|^2}{\Gamma^n_{\mathbf{k}}} \frac{f^n_{\mathbf{k}}}{\mathcal{Z}}. \tag{2.61}$$

We derived the steady-state diffusion coefficient for polaritons, highlighting the interplay between scattering mechanisms and group velocities. This theoretical groundwork provides critical insights for understanding polariton transport in strongly coupled systems. The diffusion coefficient encapsulates steady-state behaviour, but to fully understand polariton dynamics, we must examine their quantum evolution. By employing the Heisenberg picture, we can derive time-dependent equations of motion for polaritons, including their interactions with phonons and external radiation.

The diffusion coefficient depends on both the polariton group velocity and the effective scattering rate through the relation $\Gamma^n_{\mathbf{k}} = \hbar/\tau_{\mathbf{k}}$. While the group velocity reflects the dispersion of the polariton branches (see Sec.2.4), the scattering rate phenomenologically accounts for relaxation processes such as phonon-induced scattering and disorder. Due to the hybrid light–matter nature of polaritons, these quantities generally inherit contributions from both the photonic and excitonic components, with the group velocity largely influenced by the photonic dispersion and scattering processes predominantly arising from the excitonic fraction. A detailed microscopic treatment of the scattering mechanisms is deferred to chapter 3.

2.6 Heisenberg Equations of Motion for Polaritons

Until now, we have worked in the Schrödinger picture, where the operators are constant in time. However, the Hamiltonian can give us access to the time dynamics of the system. To accomplish this, we change into the Heisenberg picture, where the time evolution of an observable (or, in our case, the expectation value) is determined by the equation of motion

$$i\hbar\frac{d\langle\hat{\mathcal{O}}\rangle}{dt} = \langle[\hat{H},\hat{\mathcal{O}}]\rangle. \tag{2.62}$$

In modelling polariton dynamics, phonons are treated as an incoherent thermal bath that induces relaxation and scattering processes. We therefore adopt the Markov approximation, assuming that bath correlations decay rapidly compared to system dynamics, allowing scattering to be described as memoryless. Furthermore, coherent phonon dynamics are neglected, such that phonons primarily act as stochastic scattering channels rather than coherent degrees of freedom. This approach is justified in the weak-coupling, finite-temperature regime relevant for TMD microcavity systems. These approximations enable us to derive a tractable set of equations that capture the essential dynamics. We start from the Heisenberg equations of motion for the coherent population of polaritons and the external radiation field, taking their expectation values. For this, we make a correlation expansion including the dynamics of the phonon-assisted polarization [19, 160]. We consider a coherent calculation, i.e., the input laser is coherent and creates a coherent population of polaritons $\langle\hat{Y}\rangle = \hat{Y} \neq 0$, but not coherent phonons, i.e., $\langle\hat{b}\rangle = 0$.

Hence, the equations of motion are

$$i\hbar\frac{d}{dt}\hat{Y}^n_{\mathbf{k}}(t) = E^n_{\mathbf{k}}\hat{Y}^n(t) - i\hbar\sum_{j=\mathrm{L,R}}\sum_{\mathbf{k}}\int_0^\infty \frac{d\omega}{2\pi}\alpha_{j,\mathbf{k}}(\omega)h^n_{\mathrm{c},\mathbf{k}}\langle\hat{\mathcal{B}}_{j\mathbf{k}}(t)\rangle + \\ + \hbar\sum_{\mathbf{q},n',n}\tilde{\mathcal{D}}^{n'n}_{\mathbf{k}\alpha\mathbf{q}}\langle\hat{Y}^{n'}_{\mathbf{k}-\mathbf{q}}(t)\left(\hat{b}^\dagger_{\alpha,-\mathbf{q}}(t) + \hat{b}_{\alpha\mathbf{q}}(t)\right)\rangle, \tag{2.63}$$

$$i\hbar\frac{d}{dt}\langle\hat{\mathcal{B}}_{j\mathbf{k}\omega}(t)\rangle = \langle[\hat{\mathcal{B}}_{j\mathbf{k}},\hat{H}]\rangle = \hbar\omega\hat{\mathcal{B}}^\dagger_{j\mathbf{k}\omega}(t) + i\hbar\alpha_{j,\mathbf{k}}(\omega)\sum_n h^n_{\mathrm{c},\mathbf{k}}\hat{Y}^n_{\mathbf{k}}(t), \tag{2.64}$$

$$i\hbar\frac{d}{dt}\langle\hat{b}_{\alpha\mathbf{q}}(t)\rangle = \langle[\hat{b}_{\alpha\mathbf{q}},\hat{H}]\rangle = \hbar\sum_{n,n'\mathbf{k}}\tilde{D}^{n'n}_{\alpha,-\mathbf{q}}\langle\hat{Y}^{n,\dagger}_{\mathbf{k}-\mathbf{q}}(t)\hat{Y}^n_{\mathbf{k}}(t)\rangle = 0, \tag{2.65}$$

$$i\hbar\frac{d}{dt}S^{+,n}_{\mathbf{k}\alpha\mathbf{q}}(t) = \left(E^n_{\mathbf{k}-\mathbf{q}} - E^b_{\alpha\mathbf{q}}\right)S^{+,n}_{\mathbf{k}\alpha\mathbf{q}}(t) + \hbar\sum_{n'}\tilde{\mathcal{D}}^{n'n}_{\mathbf{k}\alpha,-\mathbf{q}}n^b_{\alpha\mathbf{q}}\hat{Y}^{n'}_{\mathbf{k}}(t), \tag{2.66}$$

$$i\hbar\frac{d}{dt}S^{-,n}_{\mathbf{k}\alpha\mathbf{q}}(t) = \left(E^n_{\mathbf{k}-\mathbf{q}} + E^b_{\alpha\mathbf{q}}\right)S^{-,n}_{\mathbf{k}\alpha\mathbf{q}}(t) + \hbar\sum_{n'}\tilde{\mathcal{D}}^{n'n}_{\mathbf{k}\alpha,-\mathbf{q}}n^b_{\alpha\mathbf{q}}\hat{Y}^{n'}_{\mathbf{k}}(t), \tag{2.67}$$

where n characterizes each polariton branch and $S^{+/-,n}_{\mathbf{k}}$ are the phonon-assisted polarizations [154]. Next, we write a formal solution for the photon bath operator in terms of an arbitrary initial time solution t_0 with $t > t_0$. This operator depends on the state of the bath at a time t_0 and on the history of the polaritons, i.e., they are leaking light into the photonic reservoir. We find

$$\hat{\mathcal{B}}_{j\mathbf{k}\omega}(t) = \hat{\mathcal{B}}_{j\mathbf{k}\omega}(t_0)e^{-i\omega(t-t_0)} + a_j(\omega)\sum_i h^n_{\mathrm{c},\mathbf{k}}\int_{t_0}^t dt'\hat{Y}^n_{\mathbf{k}}e^{-i\omega(t-t')}. \tag{2.68}$$

Inserting this solution into the second term of Eq. (2.63) and assuming that the coupling parameter $\alpha_{j,\mathbf{k}}(\omega) = \sqrt{\kappa_{j,\mathbf{k}}/2}$ is not frequency dependent [108], we obtain

$$i\hbar h^n_{\mathrm{c},\mathbf{k}}\sum_{\mathbf{k},j=\mathrm{L,R}}\int_0^\infty\frac{d\omega}{2\pi}\alpha_{j,\mathbf{k}}(\omega)\langle\mathcal{B}_{j\mathbf{k}\omega}(t)\rangle = -\left(\kappa_{\mathrm{L},\mathbf{k}} + \kappa_{\mathrm{R},\mathbf{k}}\right)\sum_{n'}h^{n,*}_{\mathrm{c},\mathbf{k}}h^{n'}_{\mathrm{c},\mathbf{k}}\hat{Y}^{n'}_{\mathbf{k}}(t) \\ + h^{n,*}_{\mathrm{c},\mathbf{k}}\sqrt{2\kappa_{\mathrm{L},\mathbf{k}}}b_{1,\mathbf{k}}(t) - h^{n,*}_{\mathrm{c},\mathbf{k}}\sqrt{2\kappa_{\mathrm{R},\mathbf{k}}}b_{2,\mathbf{k}}(t). \tag{2.69}$$

with the input fields

$$b_{1,\mathbf{k}}(t) = -\int_{-\infty}^\infty\frac{d\omega}{2\pi}\hat{\mathcal{B}}_{L\mathbf{k}\omega}(t_0)e^{-i\omega(t-t_0)}, \quad b_{2,\mathbf{k}}(t) = \int_{-\infty}^\infty\frac{d\omega}{2\pi}\hat{\mathcal{B}}_{R\mathbf{k}\omega}(t_0)e^{-i\omega(t-t_0)}. \tag{2.70}$$

To calculate the third term in Eq. (2.63), we need to determine the dynamics of the phonon-assisted polarizations $S^{+,n}_{\mathbf{k}\alpha\mathbf{q}}(t) = \langle \hat{Y}^n_{\mathbf{k}-\mathbf{q}} b^\dagger_{\alpha,-\mathbf{q}} \rangle$ and $S^{-,n}_{\mathbf{k}\alpha\mathbf{q}}(t) = \langle \hat{Y}^n_{\mathbf{k}-\mathbf{q}} b_{\alpha\mathbf{q}} \rangle$ appearing in Eqs. (2.66) and (2.67). These can be formally solved within the Markov approximation yielding [154].

$$S^{+,n}_{\mathbf{k}\alpha\mathbf{q}}(t) = -i\pi \sum_{n'} \tilde{\mathcal{D}}^{n'n}_{\mathbf{k}\alpha,-\mathbf{q}} n^b_{\alpha\mathbf{q}} \hat{Y}^{n'}_{\mathbf{k}}(t) \delta(\omega^{n'}_{\mathbf{k}} - \omega^n_{\mathbf{k}-\mathbf{q}} + \omega^b_{\alpha q}), \tag{2.71}$$

$$S^{-,n}_{\mathbf{k}\alpha\mathbf{q}}(t) = -i\pi \sum_{n'} \tilde{\mathcal{D}}^{n'n}_{\mathbf{k}\alpha,-\mathbf{q}} (1 + n^b_{\alpha\mathbf{q}}) \hat{Y}^{n'}_{\mathbf{k}}(t) \delta(\omega^{n'}_{\mathbf{k}} - \omega^n_{\mathbf{k}-\mathbf{q}} - \omega^b_{\alpha q}). \tag{2.72}$$

Furthermore, we determine the dynamics of the coherent polariton amplitude

$$i\hbar \frac{d}{dt} \hat{Y}^n_{\mathbf{k}}(t) = -\frac{i}{\hbar} E^n_{\mathbf{k}} \hat{Y}^n_{\mathbf{k}}(t) - \sum_{n'} [h^{n,*}_{\mathrm{c},\mathbf{k}} h^{n'}_{\mathrm{c},\mathbf{k}} (\kappa_{\mathrm{L},\mathbf{k}} + \kappa_{\mathrm{R},\mathbf{k}} + i\hbar \Gamma^{n',n}_{\mathbf{k}}] \hat{Y}^{n'}_{\mathbf{k}}(t), \tag{2.73}$$

and in the limit of a perfect cavity, $\kappa_L = \kappa_R = 0$, we find [154]

$$\frac{d}{dt} \hat{Y}^n_{\mathbf{k}}(t) = -\frac{i}{\hbar} E^n_{\mathbf{k}} \hat{Y}^n_{\mathbf{k}}(t) - \sum_{n'} \Gamma^{n',n}_{\mathbf{k}} \hat{Y}^{n'}_{\mathbf{k}}(t), \tag{2.74}$$

where $\Gamma^{n',n}_{\mathbf{k}}$ is the polariton-phonon scattering rate. Assuming that phonons do not induce oscillations between different polaritons, we obtain

$$\begin{aligned} i\hbar \frac{d}{dt} \hat{Y}^n_{\mathbf{k}}(t) = (E^i_{\mathbf{k}} - i\hbar\Gamma^n_{\mathbf{k}}) \hat{Y}^n_{\mathbf{k}}(t) - i\hbar \sum_{n'} [h^{n,*}_{\mathrm{c},\mathbf{k}} h^{n'}_{\mathrm{c},\mathbf{k}} (\kappa_{\mathrm{L},\mathbf{k}} + \kappa_{\mathrm{R},\mathbf{k}})] \hat{Y}^{n'}_{\mathbf{k}}(t) \\ + i\hbar h^{n,*}_{\mathrm{c},\mathbf{k}} \sqrt{2\kappa_{\mathrm{L},\mathbf{k}}} b_{1,\mathbf{k}}(t) - i\hbar h^{n,*}_{\mathrm{c},\mathbf{k}} \sqrt{2\kappa_{\mathrm{R},\mathbf{k}}} b_{2,\mathbf{k}}(t). \end{aligned} \tag{2.75}$$

This equation is similar to the expression found in Ref. [50], except that we have an additional term describing distinct phonon-induced damping for each polariton. Neglecting the excitation from the right-hand side of the cavity and performing the Fourier transform yields

$$\hat{Y}^n_{\mathbf{k}}(\hbar\omega) = \frac{-\hbar \sum_{n'} [h^{n,*}_{\mathrm{c},\mathbf{k}} h^{n'}_{\mathrm{c},\mathbf{k}} (\kappa_{\mathrm{L},\mathbf{k}} + \kappa_{\mathrm{R},\mathbf{k}})] \hat{Y}^{n'}_{\mathbf{k}}(\omega) + \hbar h^{n,*}_{\mathrm{c},\mathbf{k}} \sqrt{2\kappa_{\mathrm{L},\mathbf{k}}} b_{1,\mathbf{k}}(t)}{i(E^n_{\mathbf{k}} - \hbar\omega) + \hbar\Gamma^n_{\mathbf{k}}} \tag{2.76}$$

with the polariton scattering rates

$$\Gamma^n_{\mathbf{k}} = 2\pi \sum_{n'\alpha\mathbf{k}'} |\tilde{\mathcal{D}}^{n',n}_{\alpha,\mathbf{k}-\mathbf{k}'}|^2 \left(\frac{1}{2} \pm \frac{1}{2} + n^b_{\alpha,\mathbf{k}-\mathbf{k}'} \right) L_{\tilde{\gamma}_0} \left(E^{n'}_{\mathbf{k}'} - E^k_{\mathbf{k}} \pm \hbar\omega^b_{\alpha,\mathbf{k}-\mathbf{k}'} \right), \tag{2.77}$$

with $\tilde{\mathcal{D}}^{n',n}_{\alpha,\mathbf{k}-\mathbf{k}'}$ the polariton-phonon matrix element, $n^b_{\alpha,\mathbf{k}-\mathbf{k}'}$ the Bose-Einstein distribution, $\hbar\omega^b_{\alpha,\mathbf{k}-\mathbf{k}'}$ the phonon energy of the mode α with momentum $\mathbf{q} = \mathbf{k}' - \mathbf{k}$, and $L_{\tilde{\gamma}_0}(\hbar\omega)$ the Lorentzian function with a broadening $\tilde{\gamma}_0$,

$$L_{\tilde{\gamma}_0}(\hbar\omega) = \frac{1}{\pi}\frac{\tilde{\gamma}_0}{\tilde{\gamma}_0^2 + \hbar\omega^2}. \tag{2.78}$$

This result is similar to the exciton scattering rates [160, 161], where one can replace the exciton energies with the polaritonic energies and the exciton-phonon matrix element with the renormalized polariton-phonon matrix element. This is due to only the excitonic part of the polariton coupling to the phonons.

Using the Heisenberg equations, we derived the time evolution of polariton states, incorporating phonon-assisted processes and cavity dynamics. These results provide the basis for modelling the coherent and incoherent dynamics of polariton populations in microcavities. The Heisenberg equations of motion offer a comprehensive description of polariton dynamics. To connect these theoretical insights to experimental observables, we analyze polariton absorption, which links microscopic interactions to measurable macroscopic spectra.

2.7 Polariton Absorption

Cavity polaritons constitute an open quantum system due to their photonic component, which enables coupling between the intracavity field and the external radiation continuum. To describe this interaction, we employ the Heisenberg–Langevin formalism together with input–output theory [108]. This framework provides a direct connection between the internal cavity dynamics and the measurable external optical fields.

We consider a coherent excitation scenario in which an external laser drives the cavity, generating a coherent population of polaritons. Starting from the Heisenberg equations of motion for the polariton operators and the external radiation modes, we include a correlation expansion that accounts for phonon-assisted polarization dynamics. To derive the input–output relations, we adopt the standard formalism based on a formally time-reversed description of the reservoir dynamics, allowing the external photon bath to be expressed

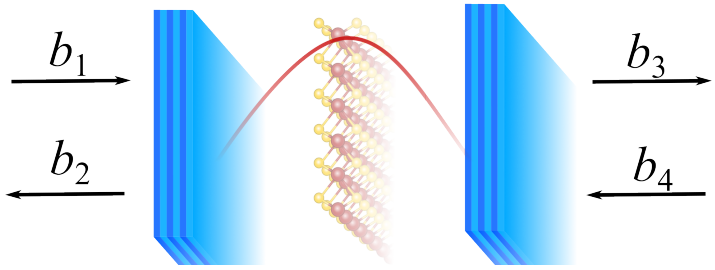


Figure 2.6: Schematic representation of the input and output fields $b_{i,\mathbf{k}}(t)$ in the system.

in terms of asymptotic output fields [50]. Throughout this treatment, we assume restricted time reversal [162], whereby dissipative processes remain lossy rather than transforming into gain. Under this assumption, the presence of phonons does not modify the fundamental structure of the input–output relations but instead enters through modified decay channels.

The following equations initiate our analysis, starting from Eq. (2.75) derived in the previous section:

$$i\hbar\frac{d}{dt}\hat{Y}^n_{\mathbf{k}}(t) = (E^i_{\mathbf{k}} - i\hbar\Gamma^n_{\mathbf{k}})\hat{Y}^n_{\mathbf{k}}(t) - i\hbar\sum_{n'}[h^{n,*}_{\mathrm{c},\mathbf{k}}h^{n'}_{\mathrm{c},\mathbf{k}}(\kappa_{\mathrm{L},\mathbf{k}} + \kappa_{\mathrm{R},\mathbf{k}})]\hat{Y}^{n'}_{\mathbf{k}}(t)$$
$$+ i\hbar h^{n,*}_{\mathrm{c},\mathbf{k}}\sqrt{2\kappa_{\mathrm{L},\mathbf{k}}}b_{3,\mathbf{k}}(t) - i\hbar h^{n,*}_{\mathrm{c},\mathbf{k}}\sqrt{2\kappa_{\mathrm{R},\mathbf{k}}}b_{4,\mathbf{k}}(t) \tag{2.79}$$

which lead to the subsequent relations for the input and output fields

$$b_{3,\mathbf{k}}(t) = -\int_{-\infty}^{\infty}\frac{d\omega}{2\pi}\hat{\mathcal{B}}_{\mathrm{R}\mathbf{k}\omega}(t_1)e^{-i\omega(t-t_1)}, \tag{2.80}$$

$$b_{4,\mathbf{k}}(t) = +\int_{-\infty}^{\infty}\frac{d\omega}{2\pi}\hat{\mathcal{B}}_{\mathrm{L}\mathbf{k}\omega}(t_1)e^{-i\omega(t-t_1)}. \tag{2.81}$$

To better visualize the input and output fields $b_{i,\mathbf{k}}(t)$, Figure 2.6 schematically represents the input and output fields in the cavity system, highlighting the roles of photonic coupling and the polariton recombination pathways. This diagram is instrumental in understanding the derivation of the transmission and reflection coefficients discussed in this section.

The next step is to Fourier transform these relations and apply them to the previously discussed polariton dynamics, allowing us to calculate the

transmission coefficient under single-sided excitation, where no incoming field is present at the right port ($b_{2,\mathbf{k}} = 0$ as illustrated in Fig. 2.6).

$$it^n_{\mathbf{k}}(\omega) = \frac{b_{3,\mathbf{k}}(\omega)}{b_{1,\mathbf{k}}(\omega)} = -\frac{\Omega_{\mathbf{k}}(\omega)\sqrt{2\kappa_{\mathrm{R},\mathbf{k}}}\sqrt{2\kappa_{\mathrm{L},\mathbf{k}}}}{1+\Omega_{\mathbf{k}}(\omega)[\sqrt{2\kappa_{\mathrm{L},\mathbf{k}}}+\sqrt{2\kappa_{\mathrm{R},\mathbf{k}}}]}, \tag{2.82}$$

with the corresponding omega function

$$\Omega_{\mathbf{k}}(\omega) = \sum_n \frac{|h^n_{\mathrm{c},\mathbf{k}}|^2}{i(\omega^n_{\mathbf{k}} - \omega + \Gamma^n_{\mathbf{k}})}. \tag{2.83}$$

Reflection coefficients follow a similar pattern

$$r^n_{\mathbf{k}}(\omega) = \frac{b_{4,\mathbf{k}}(\omega)}{b_{1,\mathbf{k}}(\omega)} = \frac{-1+\Omega_{\mathbf{k}}(\omega)[\kappa_{\mathrm{L},\mathbf{k}} - \kappa_{\mathrm{R},\mathbf{k}}]}{1+\Omega_{\mathbf{k}}(\omega)[\kappa_{\mathrm{L},\mathbf{k}} + \kappa_{\mathrm{R},\mathbf{k}}]}. \tag{2.84}$$

Finally, under the assumption of a symmetric cavity where $\kappa_L = \kappa_R$, the Elliot-like formula for polariton absorption is derived as follows:

$$A^n_{\mathbf{k}}(\hbar\omega) = 1 - |r^n_{\mathbf{k}}(\hbar\omega)|^2 - |it^n_{\mathbf{k}}(\hbar\omega)|^2 = \frac{4\gamma^n_{\mathbf{k}}\Gamma^n_{\mathbf{k}}}{(E^n_{\mathbf{k}} - \hbar\omega)^2 + (2\gamma^n_{\mathbf{k}} + \Gamma^n_{\mathbf{k}})^2}. \tag{2.85}$$

This equation mirrors the findings reported in Ref. [50], highlighting crucial differences primarily due to the inclusion of polariton-phonon interactions in our analysis. We introduce the decay rates as follows

$$\gamma^n_{\mathbf{k}} = \hbar c(1-|r_m|^2)|h_{\mathrm{c},\mathbf{k}}|^2/(4L_{cav}), \tag{2.86}$$

$$\Gamma^n_{\mathbf{k}} = 2\pi \sum_{n'\alpha\mathbf{k}'} |\tilde{\mathcal{D}}^{n'n}_{\alpha,\mathbf{k}'-\mathbf{k}}|^2 \left(\frac{1}{2} \pm \frac{1}{2} + n^b_{\alpha,\mathbf{k}'-\mathbf{k}}\right) \times$$
$$\times\, L_{\tilde{\gamma}_0}\left(E^{n'}_{\mathbf{k}'} - E^n_{\mathbf{k}} \pm E^b_{\alpha,\mathbf{k}'-\mathbf{k}}\right), \tag{2.87}$$

where $\gamma^n_{\mathbf{k}}$ represents the effective cavity decay rate from one port, and $\Gamma^n_{\mathbf{k}}$ denotes the polariton-phonon scattering rate, summing over all potential scattering channels from a given polariton state $n, \mathbf{k}$ to all possible destination polariton states $n', \mathbf{k}'$ through phonon interaction with mode α and momentum $\mathbf{q}$. The cavity's quality factor is given by $Q_f = E^{\mathrm{c}}_0 L_{cav}/[\hbar c(1-|r_m|^2)|)]$, with r_m set by default to 0.99 unless stated otherwise.

The polaritonic Elliot formula provides insights into how microscopic decay channels manifest in the absorption of light by polaritons, an analysis not

achievable with the traditional classical transfer-matrix method [56]. Evaluating Equation (2.85) at resonance conditions shows that absorption is maximized when the effective polariton decay rates are closest. Thus, a maximum absorption of 50% is achievable under the critical coupling condition [163, 164], where $\gamma_{\mathbf{k}}^{n} = \Gamma_{\mathbf{k}}^{n}/2$, indicating an equilibrium between the radiative leakage from the cavity and the intrinsic dissipation within the TMD layer. This state represents a well-known limitation for symmetric, two-port systems supporting a singular resonance [165, 166]. The presence of dark excitons, particularly in tungsten-based TMDs where they are the lowest energy states, is expected to significantly elevate the polariton-phonon scattering rates. This adjustment could profoundly affect the balance between effective radiative coupling and scattering losses, potentially leading to distinctive features in polariton absorption spectra that are measurable in experimental settings.

This section provided a detailed analysis of polariton absorption, connecting microscopic decay channels to macroscopic optical spectra. The derived Elliot-like formula offers a quantitative tool for interpreting absorption experiments in strongly coupled TMD microcavity systems.

CHAPTER 3

Polariton Transport

This chapter investigates the transport properties of exciton-polaritons TMDs, focusing on the role of phonon interactions in influencing their diffusion coefficients. An in-depth analysis of polariton-phonon induced scattering rates provides the foundation for understanding energy dissipation and mobility in polaritonic devices. We explore how these rates affect polariton mobility under various conditions, impacting their efficacy in device applications. The insights from this chapter lay the groundwork for optimizing polariton-based devices, potentially leading to new developments in optoelectronic technology. In this chapter, we discuss the results of Paper I.

3.1 Phonon-induced Scattering Rates

Understanding phonon-induced scattering rates is the basis for describing the transport properties and energy dissipation mechanisms of exciton-polaritons in semiconductor systems. These hybrid quasiparticles interact strongly

with lattice vibrations, influencing their linewidth, lifetime, and transport behaviours such as diffusion and optical absorption.

We begin by retrieving the polariton-phonon scattering rate, calculated in Chapter 2,

$$\begin{aligned}\Gamma^{n}_{\mathbf{k}} =& 2\pi \sum_{n'\alpha\mathbf{k}'} |\tilde{\mathcal{D}}^{n',n}_{\alpha,\mathbf{k}-\mathbf{k}'}|^2 \left(\frac{1}{2} \pm \frac{1}{2} + n^{b}_{\alpha,\mathbf{k}-\mathbf{k}'}\right) \times \\ & \times L_{\tilde{\gamma}_0}\left(E^{n'}_{\mathbf{k}'} - E^{n}_{\mathbf{k}} \pm \hbar\omega^{b}_{\alpha,\mathbf{k}-\mathbf{k}'}\right), \end{aligned} \tag{3.1}$$

where $\tilde{\mathcal{D}}^{n',n}_{\alpha,\mathbf{k}-\mathbf{k}'}$ is the polariton-phonon matrix element, $n^{b}_{\alpha,\mathbf{k}-\mathbf{k}'}$ is the Bose-Einstein distribution, $\hbar\omega^{b}_{\alpha,\mathbf{k}-\mathbf{k}'}$ is the phonon energy of mode α with momentum $\mathbf{q} = \mathbf{k}' - \mathbf{k}$, and $L_{\tilde{\gamma}_0}(\hbar\omega)$ is the Lorentzian function with broadening $\tilde{\gamma}_0$. The Lorentzian function, rather than a delta function, captures higher-order effects like collisional broadening [167, 168] and provides a more accurate representation of real systems beyond the so-called completed-collision limit [169]. A broadening parameter of 0.1 meV is chosen to establish a lower bound for scattering rates.

Given the excitonic landscape, this chapter is organized into two main sections: intra-valley scattering in the KK valley, followed by inter-valley scattering, which includes contributions from the Λ and K$'$ valleys. Effects of disorder and defects are neglected in our analysis [87].

3.1.1 Intra-valley Scattering

We begin by examining intra-valley scattering processes within the KK valley, focusing on how these interactions shape the polariton dynamics. Figure 3.1 shows the intra-valley polariton-phonon scattering rates at $T = 40$ K, chosen for its relevance to key phenomena.

At $T = 40$ K, scattering into lower polariton (LP) states outside the light-cone is most efficient due to limited available states within the light-cone and the negligible Hopfield coefficient $h^{\mathrm{UP}}_{\mathrm{X}}$ for large-momentum upper polariton (UP) states. The receiving LP state is quasi-excitonic ($h^{\mathrm{LP}}_{\mathrm{X}} \approx 1$), as the excitonic component drives phonon scattering. However, despite the dominant excitonic

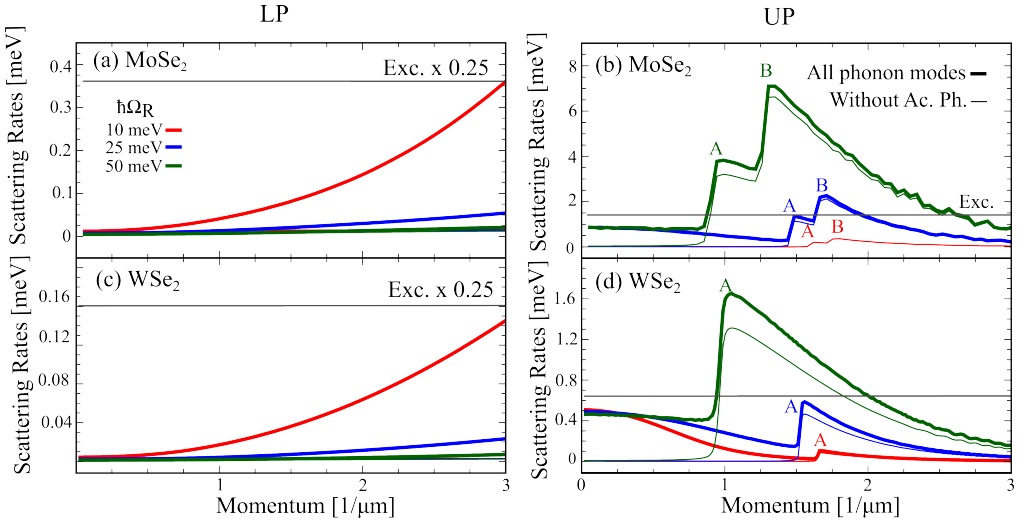


Figure 3.1: Polariton-phonon scattering rates at $T = 40$ K for (a) and (c) the lower polariton branch for $MoSe_2$ and WSe_2, respectively. (b) and (d) the upper polariton branch for $MoSe_2$ and WSe_2, respectively. Thin lines represent the case without acoustic phonon contributions. Note that in (a) and (c), the thin lines are nearly momentum-independent, highlighting the significant role of acoustic phonons in enhancing scattering at large momenta.

character of LP states, our microscopic calculations reveal an intriguing result: the UP branch exhibits more efficient scattering in certain momentum regimes (Fig. 3.1(b)).

This behaviour can be understood by analysing the role of polariton dispersion and phonon-assisted transitions. Figure 3.2(a) schematically depicts the scattering channels mediated by acoustic and optical phonons, while Fig. 3.2(b) highlights the crossing points of the optical phonon dispersion with the UP branch for different Rabi splitting, explaining the observed resonances in Fig. 3.1(b). At small momenta, resonant scattering with optical phonons leads to enhanced rates for the UP branch, as the polariton's higher energy provides access to a broader range of scattering partners.

For the LP branch in $MoSe_2$ (Fig. 3.1(a)), scattering rates are two orders of magnitude smaller than the excitonic case (thin black line). This substantial reduction arises from the polariton dispersion in the strong coupling regime, which limits resonant scattering with acoustic phonons except near the exci-

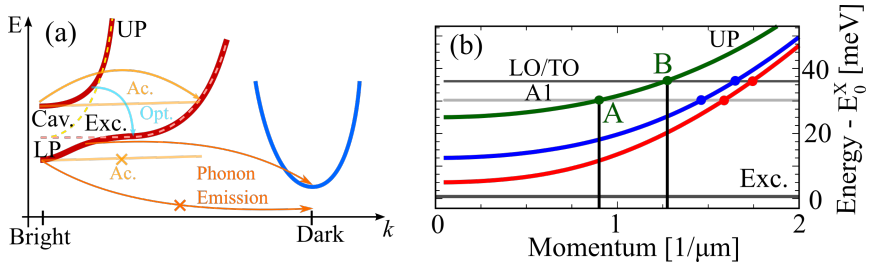


Figure 3.2: (a) Schematic of scattering channels via acoustic and optical phonons.(b) Crossing points of the optical phonon dispersion with the upper polariton branch for different values of $\hbar\Omega_R$, indicating the minimal upper polariton energies required for scattering into excitonic states and explaining the resonances in Fig. 3.1(b).

ton energy E_0^X. As momentum increases, non-resonant scattering becomes possible, reflected in the gradual rise in scattering rates with broadening (thin lines in Fig. 3.1(a)).

In WSe_2 (Fig. 3.1(c)), scattering rates are generally smaller due to weaker excitonic scattering within the KK valley. However, the qualitative trends remain consistent with $MoSe_2$, demonstrating the crucial role of acoustic phonons at larger momenta. These findings highlight how intra-valley scattering is shaped by the interplay between polariton dispersion and exciton-phonon interactions, laying the groundwork for understanding inter-valley processes discussed in the next section.

3.1.2 Inter-valley Scattering

Allowing polaritons to scatter into dark valleys introduces new pathways mediated by K′ and Q′ phonons, enabling transitions into dark excitonic states such as KK′ and KΛ. These inter-valley scattering processes significantly influence the polariton linewidth and transport properties, particularly in tungsten-based TMDs like WSe_2, where dark excitons are energetically favourable.

Figure 3.3 compares scattering rates for $MoSe_2$ and WSe_2 at $T = 77$ K for different Rabi splitting ($\hbar\Omega_R = 10, 25, 50$ meV). For $MoSe_2$, the contribution of dark excitons is negligible due to their higher energy, as shown by the

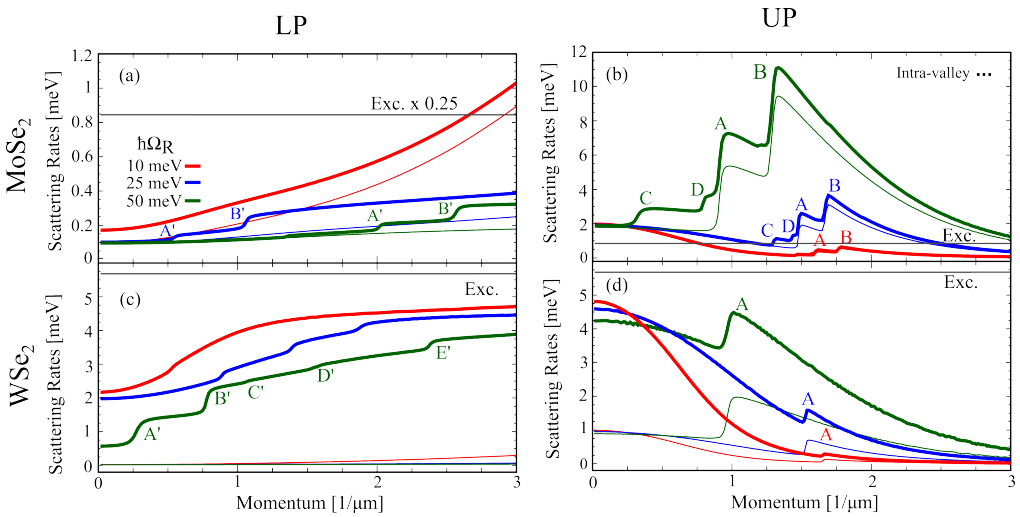


Figure 3.3: Full polariton-phonon scattering rates at $T = 77$ K for (a) and (c) lower polariton branch for $MoSe_2$ and WSe_2, respectively. (b) and (d) upper polariton branch for $MoSe_2$ and WSe_2, respectively. Thin lines indicate intra-valley scattering rates without dark exciton contributions.

overlap between intra-valley (thin lines) and total scattering rates (thick lines). By contrast, WSe_2 exhibits a significant enhancement in scattering rates due to inter-valley transitions, particularly for the lower polariton branch (LP).

For the LP branch in WSe_2, inter-valley scattering introduces step-like features in the scattering rates, corresponding to transitions mediated by acoustic and optical phonons. As shown in Fig. 3.4, these steps align with the crossing points of the polariton dispersion with phonon modes, highlighting the critical role of dark excitonic states. The energy alignment of dark excitons with $K\Lambda$ states enables efficient coupling, particularly for $\hbar\Omega_R = 50$ meV, where scattering rates increase sharply at threshold momenta.

These findings underscore the material-dependent nature of inter-valley scattering, with WSe_2 providing a unique platform for exploring dark excitonic states and their impact on polariton dynamics. This understanding is essential for interpreting temperature-dependent behaviour discussed in the next section.

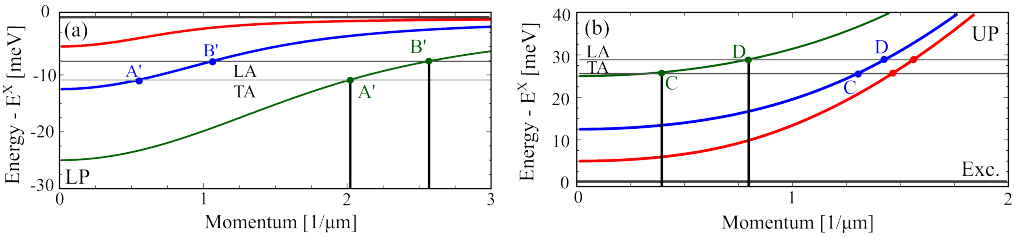


Figure 3.4: Crossing points of the acoustic phonon dispersion for $MoSe_2$ with the lower (a) and upper (b) polariton branches for different values of $\hbar\Omega_R$, indicating the minimal polariton energies required for scattering into excitonic states and explaining the resonances appearing in Fig. 3.3(a) and (b).

3.1.3 Temperature Study of Scattering Rates

The temperature dependence of polariton-phonon scattering rates provides valuable insights into the mechanisms governing polariton dynamics in WSe_2. Figure 3.5 illustrates how intra-valley and inter-valley scattering channels contribute to the linewidth of upper (UP) and lower (LP) polaritons at $k = 0$, focusing on transitions mediated by acoustic and optical phonons.

At low temperatures (e.g., 20 K), inter-valley processes dominate, particularly for the LP branch, where transitions into KK′ excitons require minimal phonon energy. As temperature increases, thermally activated phonons enable inter-valley scattering into dark states such as KΛ, leading to a substantial increase in the LP linewidth. The temperature-induced shift in dominant scattering channels reflects the increased phase space available for intervalley transitions at higher temperatures.

For the UP branch, the behaviour is distinct. At low temperatures, the UP state's higher energy makes it more susceptible to scattering into dark states, resulting in larger initial scattering rates compared to the LP branch. However, the temperature dependence is less pronounced, as many dark-state transitions are already accessible at low temperatures. This asymmetry between the LP and UP branches underscores the role of energy alignment and phonon coupling in shaping temperature-dependent scattering rates.

These findings highlight how temperature can be used as a tunable parameter to control polariton dynamics, particularly in systems where dark excitons

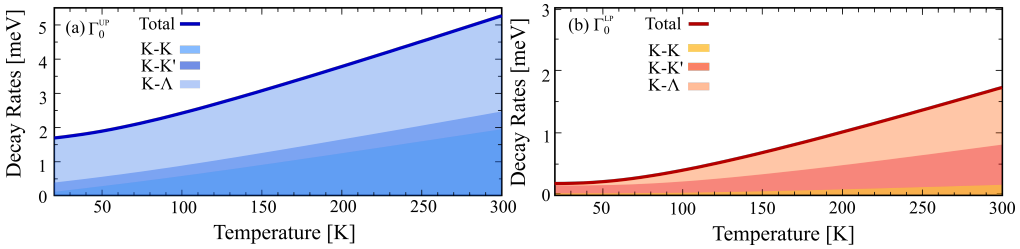


Figure 3.5: Temperature-dependent polariton-phonon scattering rates for (a) upper and (b) lower polariton branches in WSe_2 at $k = 0$ with a Rabi splitting of 25 meV, with contributions from intra-valley (K-K) and inter-valley (KK′, KΛ) scattering.

dominate inter-valley scattering. This understanding can be important for designing devices that exploit polariton-phonon interactions for tailored transport and optical properties.

To conclude, in this section, we reveal the interplay between intra- and inter-valley processes and acoustic/optical phonons in shaping polariton dynamics. Our analysis demonstrated the material-specific nature of scattering mechanisms, with dark excitons playing a part in WSe_2.

Table 3.1: Comparison of scattering characteristics in $MoSe_2$ and WSe_2.

Property	**$MoSe_2$ (Direct Bandgap)**	**WSe_2 (Indirect Bandgap)**
Dominant scattering	Intra-valley	Inter-valley (dark states)
Contribution of dark states	Minimal	Significant
Temperature dependence	Weak	Strong
Role of Rabi splitting ($\hbar\Omega_R$)	Small effect	Significant enhancement

Intra-valley scattering was shown to dominate at low temperatures and small momenta, while inter-valley scattering became increasingly significant with temperature and momentum, particularly for transitions into KΛ states. These findings provide insights into polariton transport and optical properties, laying the groundwork for further studies on tunable scattering rates in

polariton-based devices. The detailed analysis of phonon-induced scattering rates not only elucidates the intricate dynamics within TMDs but also sets the stage for understanding how these interactions impact polariton diffusion, which is explored in the following section.

3.2 Polariton Diffusion

Building on the scattering rate analysis, this section examines how these rates influence polariton diffusion across different conditions. We link scattering dynamics directly to transport properties, providing a comprehensive view of polariton mobility.

Our analysis of polariton diffusion builds on the conceptual foundation of how temperature, Rabi splitting, and scattering rates influence the diffusion coefficient. According to Eq. (2.61), the crucial parameters affecting polariton diffusion are the polariton group velocity $v^i_{\mathbf{Q}}$, the polariton-phonon scattering rate $\Gamma^i_{\mathbf{Q}}$, and the occupation of polariton states $f^i_{\mathbf{Q}}$.

Hence, a key factor influencing the diffusion of polaritons is the polariton group velocity, which depends on the extent of exciton-photon coupling. As illustrated in Fig. 3.6, polaritons with a strong photonic component exhibit significantly higher group velocities compared to those with predominantly excitonic character. This distinction arises because photonic modes, by nature, propagate much faster than excitonic modes, which are typically bound to slower transport due to their larger effective mass.

This group velocity difference between fast mixed polaritons and slower excitonic polaritons has a direct impact on the diffusion coefficient. Faster polaritons contribute more significantly to overall transport, resulting in higher diffusion coefficients, whereas slower excitonic states can act as bottlenecks, limiting diffusion, especially at higher momenta where the polariton dispersion becomes more exciton-like. With this foundation in place, we can now explore how these effects manifest in the diffusion coefficient across different conditions, as shown in Fig. 3.7.

Figure 3.7(a) shows the diffusion coefficient as a function of temperature and Rabi splitting. Based on our microscopic model, we predict that polariton

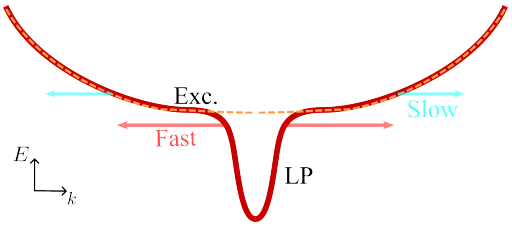


Figure 3.6: Schematic representation showing the difference in group velocity for excitonic versus mixed (strongly coupled) polaritons. Mixed polaritons, having both excitonic and photonic components, display higher group velocities (labelled as "Fast") compared to purely excitonic polaritons ("Slow"). This variation in group velocity has direct implications for the diffusion coefficient of polaritons.

diffusion coefficients can be two to three orders of magnitude larger than those for bare excitons. This enhancement is due to the following key factors:
1. **High group velocities**: Mixed polaritons with a strong photonic component benefit from enhanced group velocities, as illustrated in Fig. 3.6. This is especially pronounced for polaritons within the light-cone, where the photonic component dominates.
2. **Effective occupation of fast polaritonic states**: Lower polariton states with small momenta are more efficiently populated due to their lower energies, which enhances the contribution of fast states to the overall diffusion.
3. **Reduced phonon scattering for lower polaritons**: The phonon scattering rates for polaritons are typically lower for states with a substantial photonic component, resulting in longer relaxation times and thus enhanced diffusion.

It is important to note that these features primarily affect small-momentum polaritons. At larger momenta, the dispersion of polaritons resembles that of excitons, and their transport characteristics revert to excitonic behaviour. Therefore, the overall diffusion coefficient is the result of a non-trivial interplay between a few very fast polariton states within the light-cone and excitonic-like states outside the cone, which contribute more weakly to diffusion.

In Fig. 3.7(b), we examine the temperature dependence of the diffusion coefficient for three fixed values of the Rabi splitting: 10, 25, and 50 meV. At low temperatures, the diffusion coefficient is high due to the dominance of fast polaritonic states. Interestingly, for larger Rabi splitting, we observe

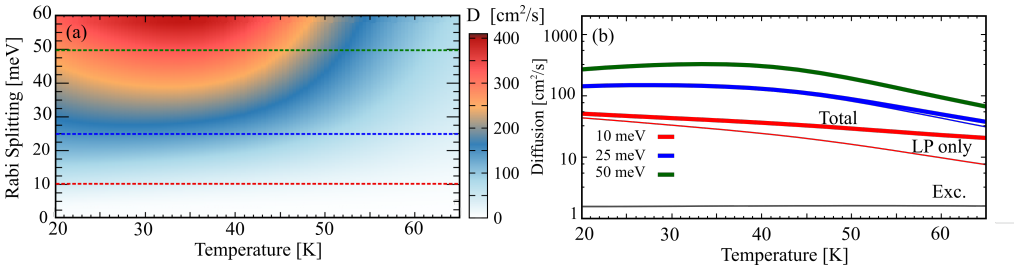


Figure 3.7: (a) Polariton diffusion coefficient as a function of temperature and Rabi splitting. (b) Cross-sectional view of (a) evaluated for fixed Rabi splitting of 10, 25, and 50 meV, with thin lines indicating diffusion stemming only from the lower polariton branch.

a peak in the diffusion coefficient around 40 K. This peak is attributed to the population of fast polariton states with maximum group velocity at approximately $Q \lesssim 1.3\,\mu\text{m}^{-1}$ at this temperature. As the temperature increases further, higher-momentum states become populated, which have lower group velocities due to their excitonic character, resulting in a gradual decrease in the diffusion coefficient. For smaller Rabi splitting (e.g., $\hbar\Omega_\text{R} = 10$ meV), the peak in diffusion is less pronounced, and diffusion decreases more rapidly with temperature. This is because, for smaller splitting, the states within the light-cone are closer to the excitonic regime and thus experience slower transport. At higher temperatures, the quasi-excitonic states outside the light-cone are increasingly populated, leading to diffusion coefficients that approach the excitonic limit, as illustrated by the grey line representing the excitonic diffusion coefficient.

To further illustrate the importance of polariton-specific scattering channels, we perform a "thought experiment" by recalculating the polariton diffusion coefficient assuming exciton-phonon scattering rates, as shown by the dashed line in Fig. 3.8. In this case, the diffusion coefficient decreases by more than an order of magnitude compared to the full polariton model. This demonstrates the significant role of modified polariton-phonon scattering in enhancing the diffusion of polaritons relative to excitons.

Interestingly, the peak at 40 K observed in the full polariton calculation (Fig. 3.7(b)) vanishes when excitonic scattering rates are used. This is because excitonic scattering rates have a weaker dependence on momentum,

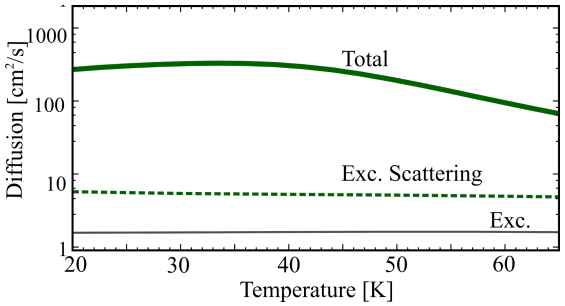


Figure 3.8: Polariton diffusion calculated under the assumption of exciton-phonon scattering rates. This calculation highlights the impact of modified scattering channels for polaritons, as opposed to the excitonic case.

which diminishes the distinction between fast and slow polariton states. Consequently, without polariton-specific scattering channels, the enhanced diffusion seen for polaritons cannot be sustained, highlighting the importance of phonon interactions in differentiating polariton transport from that of pure excitons. In summary, our results indicate that the polariton diffusion coefficient is significantly influenced by both the exciton-photon coupling strength and the polariton-phonon interactions. Large group velocities for photonic components and reduced scattering rates for mixed polaritons lead to diffusion coefficients that are considerably higher than those of bare excitons. This enhanced diffusion is most pronounced at low temperatures and large Rabi splitting, where the photonic character dominates. As temperature increases, however, the quasi-excitonic nature of higher-momentum states reduces the diffusion coefficient, approaching excitonic values at high temperatures. This study provides insights into the mechanisms underlying polariton transport and lays the groundwork for controlling diffusion in polaritonic systems.

This chapter provides a detailed overview of polariton transport in TMDs, emphasizing the role of phonon-induced scattering rates and their influence on diffusion properties. The insights obtained here provide a microscopic framework for understanding and controlling polariton transport through cavity detuning and material parameters.

CHAPTER 4

Polariton Optics

The study of polariton absorption spectra offers profound insights into the quantum mechanical interactions between light and matter within optical microcavities. Such spectra not only reveal the presence of strong coupling, characterized by Rabi splitting but also serve as a tool for understanding the dynamic properties of exciton-polaritons across various semiconductor platforms. In this chapter, we delve into polariton absorption spectra within different TMDs, exploring how these materials influence the coupling dynamics and the resulting spectral properties. In this chapter, we discuss the results of Paper II and Paper III.

4.1 Polariton Absorption of WSe_2

We begin by evaluating Equation (2.85), using numerically derived polariton-phonon scattering rates from Chapter 3, to explore polariton absorption in a strong-coupling regime for an hBN-encapsulated WSe_2 monolayer integrated

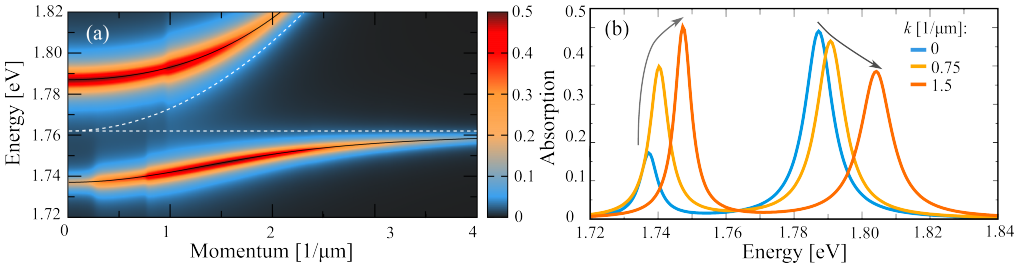


Figure 4.1: Polariton absorption in an hBN-encapsulated WSe_2 monolayer, displaying energy and momentum-resolved absorption at a temperature of 77 K, assuming a Rabi splitting of $\hbar\Omega_R = 50$ meV and a cavity quality factor of $Q_f = 160$. Dashed white lines illustrate the bare exciton and cavity dispersions, while solid black lines depict the polariton dispersion. Panel (b) shows absorption profiles for selected momenta.

within a Fabry-Perot cavity. Figure 4.1(a) presents an energy- and momentum-resolved surface plot of polariton absorption, revealing a higher intensity for the upper polariton compared to the lower polariton at zero momentum (also depicted in Fig. 4.1(b)). Such an observation aligns with historical data on GaAs, where peak intensities for lower and upper polaritons were similarly matched in zero-detuning scenarios [170, 171]. At zero detuning, both polariton branches contribute equally in terms of their photonic and excitonic components at zero momentum, thereby maintaining a consistent cavity decay rate, $\gamma^n_{\mathbf{k}}$, across both branches. Consequently, the variation in the heights of absorption peaks must be attributed to differences in phonon-induced decay rates among the polaritons. Additionally, the absorption profile enhances as momentum increases for the lower polariton (A^{LP}) up to about $k = 1.6$ μm^{-1}, contrasting with a decrease observed for the upper polariton (A^{UP}), as illustrated further in Fig. 4.1(b). The absorption intensity and the spectral linewidth for polariton resonances are predominantly influenced by the interplay between cavity decay and non-radiative decay via phonon scattering.

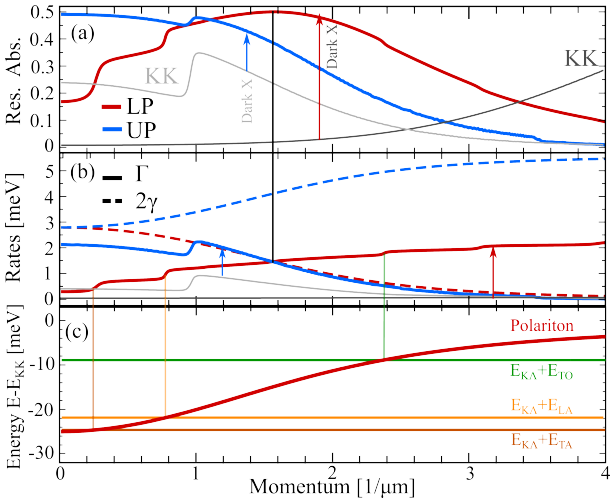


Figure 4.2: Critical coupling conditions depicted for both the lower (red, LP) and upper (blue, UP) polariton branches at 77 K, featuring a Rabi splitting of $\hbar\Omega_R = 50$ meV and a cavity quality factor of approximately 160. Panel (a) shows the maximal absorption at the resonant energy as a function of momentum. Panel (b) illustrates the polariton-phonon scattering rate $\Gamma^n_{\mathbf{k}}$ (solid lines) and cavity decay rate $\gamma^n_{\mathbf{k}}$ (dashed lines) as functions of momentum for both branches, with the critical coupling condition marked by a vertical black line. The grey lines indicate scenarios where only bright KK excitons are considered, excluding dark states. Panel (c) details the lower polariton dispersion (red line) alongside phonon energies (plus the energy of the dark KΛ exciton), showcasing the activation of emission channels into dark exciton states at momenta of approximately 0.3, 0.8, 2.4, and μm^{-1}.

4.2 Critical Coupling Condition

Exploring the varying behaviours in the absorption spectra for upper and lower polariton branches, we plot the maximal absorption, $A^n_{\mathbf{k}}$, for both branches at a temperature of 77 K (Fig. 4.2(a)). Generally, the absorption intensity for the upper polariton branch decreases with increasing momentum, except for a notable increment around $k = 1$ μm^{-1} (indicated by the blue line). In contrast, the lower polariton branch exhibits enhanced absorption up to approximately $k = 1.6$ μm^{-1}, achieving a peak absorption value of $A = 0.5$ (highlighted by the red line). This peak is accompanied by several pronounced, step-like enhancements as the maximum absorption is approached.

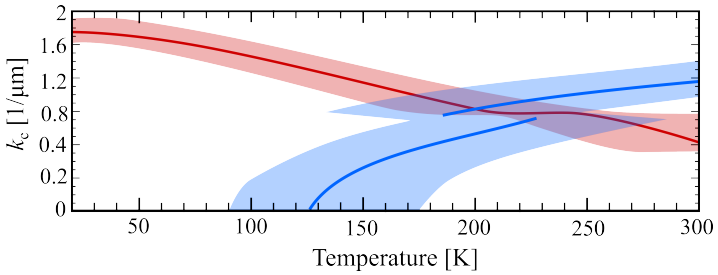


Figure 4.3: Critical coupling momentum k_c as a function of temperature for both the upper (blue) and lower polariton (red) branches. The shaded areas denote the range $0.5 \geq A^n \geq 0.495$, accounting for experimental uncertainties in measuring the maximal absorption.

To elucidate the absorption changes as a function of in-plane momentum and the divergent behaviours of the upper and lower polariton branches, we examine the momentum-dependent cavity decay rate, $\gamma^n_{\mathbf{k}}$, alongside the polariton-phonon scattering rate, $\Gamma^n_{\mathbf{k}}$, as outlined in Equations (2.86) and (2.87) and depicted in Fig. 4.2(b). The critical coupling condition, where $\Gamma^n_{\mathbf{k}} = 2\gamma^n_{\mathbf{k}}$, is attained at $k = 1.6\ \mu\text{m}^{-1}$ for the lower polariton branch, marked by the vertical black line in the figure, aligning precisely with the momentum that maximizes absorption at $A^{LP} = 0.5$. Figure 4.2(c) plots the lower polariton dispersion relative to the bright exciton energy together with the phonon dispersion for LA, TA, and TO modes responsible for scattering into dark KΛ excitons. A more detailed analysis of the step-like behaviour of the lower polariton is provided in Chapter 3. It is noteworthy that the cavity decay rate, $\gamma^n_{\mathbf{k}}$, varies smoothly with k for both the upper and lower polariton branches, as shown by the dashed lines in Fig. 4.2(b). This variation is influenced by the photonic Hopfield coefficient, which increases for the upper polariton while decreasing for the lower polariton.

To highlight the significance of dark excitons, we also present polariton absorption and polariton-phonon scattering rates excluding dark exciton states, considering only bright KK excitons (represented by grey lines in Figs. 4.2(a,b)). For the lower polariton, resonant absorption is drastically reduced at small momenta, with the critical coupling condition shifting to higher momenta. Additionally, the notable step-like increases observed for these polaritons are absent (comparing the red and lower grey lines), as they originate from scattering into dark excitons. Although our analysis initially

focuses on polariton absorption at 77 K, where the critical coupling condition is achievable only for the lower polariton branch, we extend our investigation to varying temperatures as illustrated in Fig. 4.3. Here, we depict the critical coupling momentum, k_c, as a function of temperature for both the upper (blue line) and lower polariton (red line) branches. The blue- and red-shaded areas correspond to regions where $0.5 \geq A^n \geq 0.495$, accommodating uncertainties in the experimental measurement of maximal absorption. As temperature increases, the critical coupling occurs at smaller momenta for the LP branch due to heightened scattering with phonons. Given that the cavity decay rates, $\gamma^i_{\mathbf{k}}$, are temperature-independent within our model, the overall increase in $\Gamma^n_{\mathbf{k}}$ at elevated temperatures results in smaller k_c values that meet the critical coupling conditions. Notably, for the upper polariton branch, critical coupling is absent below approximately 125 K. As shown in Fig. 4.2(b), at $k = 0$, the cavity decay rate $\gamma^n_{\mathbf{k}}$ exceeds $\Gamma^n_{\mathbf{k}}$. However, while $\gamma^{LP}_{\mathbf{k}}$ diminishes with increasing momenta, approaching the lower values of $\Gamma^n_{\mathbf{k}}$, the reverse occurs for $\gamma^{UP}_{\mathbf{k}}$. Thus, for upper polaritons, critical coupling is achievable only at higher temperatures, where $\Gamma^n_{\mathbf{k}}$ is substantially enhanced. Intriguingly, around 200 K, two distinct momenta fulfil the critical coupling condition for UP (as indicated by the blue lines in Fig. 4.3). At these temperatures, the cavity decay rate intersects the polariton-phonon scattering rate in the region of the opening of the optical emission (noted by a step-like increase), allowing for identical scattering and cavity-decay rates at two (or more) momenta.

We have shown that polariton absorption depends on two key factors: the polariton-phonon scattering rate $\Gamma^n_{\mathbf{k}}$ and the cavity decay rate $\gamma^n_{\mathbf{k}}$. Our goal now is to tune the absorption by manipulating these variables. While $\Gamma^n_{\mathbf{k}}$ is highly sensitive to temperature changes, $\gamma^n_{\mathbf{k}}$ is primarily determined by the cavity's quality factor, specifically the reflectance of the cavity's end mirrors.

In Figs. 4.4(a) and (b), we present the temperature-dependent polariton-phonon scattering rates at zero momentum for both the upper and lower polariton branches, respectively. Note that this corresponds to half the linewidth of the respective polariton resonance in absorption spectra. We include various scattering channels such as intravalley scattering within the K valley (KK) as well as intervalley scattering into momentum-dark exciton states (KK$'$ and KΛ). For comparison, the black dashed line illustrates the temperature-independent $2\gamma_0$, indicating the temperatures at which the critical coupling condition is met at $k_C = 0$. This condition is achieved for

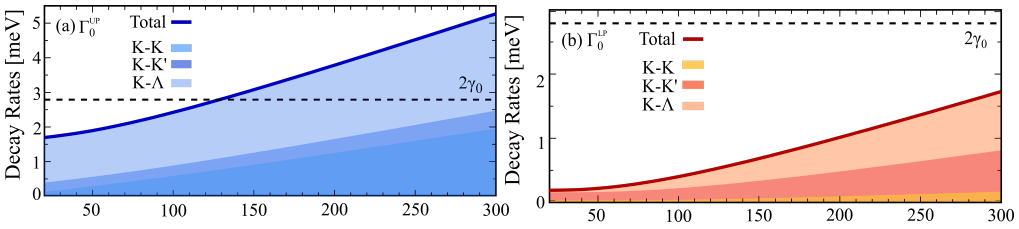


Figure 4.4: Temperature study of polariton-phonon scattering rates $\Gamma^n_{\mathbf{k}}$ for both the upper (UP) and lower polariton branch (LP) at $k = 0$ as a function of temperature (for Q_f ≈160). Contributions from intravalley (KK) and intervalley (KK′, KΛ) scattering channels are highlighted (shaded areas), with $2\Gamma^i_0$ representing the spectral linewidth of the respective polariton. The crossing point with the cavity decay rate $2\gamma^i_0$ (dashed line) marks the critical coupling condition.

the UP branch at approximately 125 K, in alignment with observations from Fig. 4.2(c).

In contrast, for the LP branch, reaching the critical coupling at $k_C = 0$ is only possible at temperatures significantly above room temperature. For both polariton branches, the major contributions to the linewidth arise from intervalley scattering into dark KΛ excitons, reflecting efficient scattering plus the three-fold degeneracy of the Λ valley, akin to the excitonic scenario [128]. Furthermore, at room temperature, intervalley scattering within the K valley also plays a significant role. At 20 K, the LP linewidth is predominantly determined by scattering into the dark KK′ excitons. We emphasize that our focus here is on scattering from the $k = 0$ polariton state, although additional scattering channels at larger momenta are possible, as illustrated in Fig. 4.2(b).

Increasing the temperature to 300 K leads to a substantial broadening of the lower polariton (LP) linewidth, increasing by approximately an order of magnitude as intervalley phonon absorption channels become thermally activated. At 77 K, the intravalley contribution to the phonon-scattering rates remains weak, consistent with the behaviour observed in Fig. 4.2. The upper polariton (UP) linewidth is already comparatively large at 20 K, as emission into dark exciton states is energetically allowed even at $k = 0$ due to the higher polariton energy (see Fig. 4.1(b)). Consequently, the relative increase in UP linewidth between 20 K and 300 K is less pronounced than for the LP branch. Overall, Figs. 4.4(a,b) highlight the significant role of dark exciton

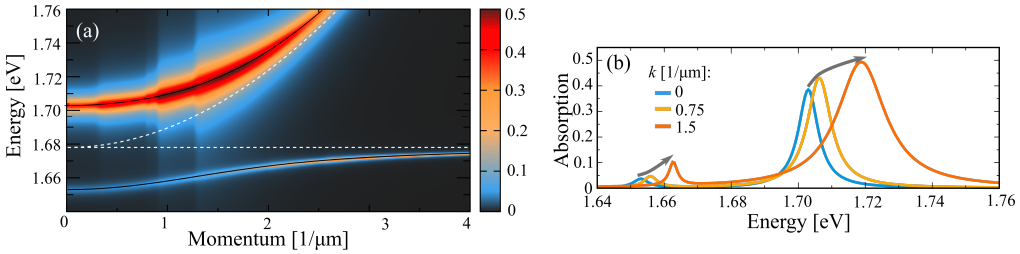


Figure 4.5: Polariton absorption of an hBN-encapsulated $MoSe_2$ monolayer, showing momentum and energy-resolved absorption at 77 K, assuming a Rabi splitting of $\hbar\Omega_R = 50$ meV and a cavity quality factor of approximately 160. Panel (b) presents absorption profiles at various energies for selected momenta.

channels in enhancing polariton–phonon scattering and thereby increasing the polariton linewidth.

4.3 Polariton Absorption of $MoSe_2$

While our studies thus far have focused on WSe_2 monolayers, where dark excitons influence the absorption, we now turn our attention to $MoSe_2$ monolayers, which exhibit a different energetic alignment of dark and bright states. With bright states being energetically lower in $MoSe_2$ [17, 19, 142], we anticipate a negligible contribution from dark excitons. Similarly to our observations with WSe_2, we examine the absorption of polaritons as a function of momentum and energy for the zero-detuning case at 77 K in $MoSe_2$. We observe a significant reduction in both absorption and the linewidth of the LP absorption compared to WSe_2, as depicted in Fig. 4.5(b). Although the intensity of resonant absorption increases for larger momenta, similar to WSe_2, the rate of increase is markedly slower, peaking at approximately 0.1 at $k = 1.5$ μm^{-1}, in contrast to the near-0.5 peak observed for WSe_2. Additionally, for larger momenta, we note an increase in the absorption for the UP branch in $MoSe_2$, opposite to the trend observed in WSe_2 (Fig. 4.1(b)). Furthermore, we witness a substantial expansion in the spectral width of polariton resonances at increased in-plane momenta, k.

To microscopically comprehend the qualitative and quantitative differences in

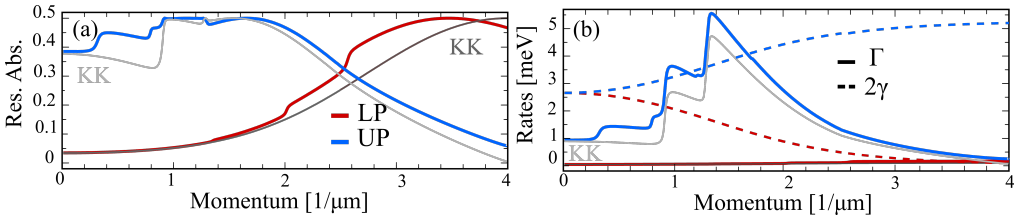


Figure 4.6: Absorption of $MoSe_2$. (a) Absorption intensity as a function of momentum for the lower (LP) and the upper (UP) polariton branch. (b) Decay rates $\Gamma^n_{\mathbf{k}}$ and $2\gamma^n_{\mathbf{k}}$ as a function of momentum for the LP and UP branches. The thin grey lines in (a) and (b) correspond to the case without dark excitons (considering only the bright KK excitons).

the momentum-resolved absorption between $MoSe_2$ and WSe_2, we analyze the intensity of the resonant polariton absorption and the underlying polariton-phonon and cavity decay rates. Assuming the same reflectivity value, $r_m = 0.99$, as used in our WSe_2 studies, we achieve similar cavity decay rates, $\gamma^n_{\mathbf{k}}$, for both materials. We also present both absorption and decay rates for scenarios excluding dark excitons (grey lines in Figs. 4.6(a,b)). As anticipated, in $MoSe_2$, dark states contribute minimally (as previously observed in scattering rates, see Chapter 3).

Nonetheless, the decrease in the cavity decay rate, $\gamma^n_{\mathbf{k}}$, with increasing momenta facilitates the attainment of the critical coupling condition at exceptionally high momenta of $k_c = 3.25\ \mu\text{m}^{-1}$ (cf. Fig. 4.5(b)), where the LP absorption reaches its maximal value of $A^n = 0.5$ (Fig. 4.6(a)). Interestingly, despite the minor contribution from dark excitons, their presence shifts the critical coupling condition to a lower momentum (compare the grey and red lines in Fig. 4.6(a)).

For the upper polariton, the intravalley scattering contribution is predominant (with only slight deviations between the grey and blue lines). Unlike WSe_2, we observe a significant increase in phonon-scattering rates for the UP branch in $MoSe_2$, indicative of more efficient intravalley scattering with optical modes in this material [122]. This phenomenon leads to the broader spectral width of the resonances observed in Fig. 4.5(b). Although the contribution from dark excitons is minor, we still detect an opening of an emission channel into dark states, as reflected by the step-like increase in $\Gamma^{UP}_{\mathbf{k}}$ at approximately $k = 0.4\ \mu\text{m}^{-1}$.

This opening is the basis for comprehending the increase in resonant absorption from $k = 0$ to $k = 0.75$ μm^{-1}, as observed in Fig. 4.5(b) and in contrast to predictions for WSe_2 in Fig. 4.1(a). Without dark states, there would be a decrease in absorption up to about 0.9 μm^{-1} (cf. the grey line in Fig. 4.6(a)). In $MoSe_2$, the upper polariton meets the critical coupling condition at four different momenta: $k_c \approx 1$, 1.2, 1.3, and 1.6 μm^{-1}. The lowest two are a result of polariton scattering into dark exciton states.

4.4 The Effect of the Environment

In this section, we briefly explore how changes in the dielectric medium impact polariton absorption. We compare the free-standing case with the hBN-encapsulated scenario discussed previously. One notable difference when considering various substrates is the altered dielectric screening of the Coulomb interaction. The dielectric constant, ε, is larger for hBN compared to other substrates like SiO_2 or air (in the free-standing scenario). A lower ε increases the energy separation $E_{\mathrm{K}\mathrm{K}} - E_{\mathrm{K}\Lambda}$ between bright and dark excitons, due to conduction band electrons possessing a higher effective mass at the Λ valley compared to the K valley. This results in a higher binding energy for KΛ excitons (relative to KK excitons) and thus a more pronounced change due to substrate-induced screening.

To delve deeper into the substrate impact, we perform new calculations for a free-standing WSe_2 monolayer. Figure 4.7(a) presents the polariton scattering rates as a function of momentum for both hBN-encapsulated and free-standing WSe_2. Changes in the dielectric medium exhibit no significant impact on the upper polariton, as illustrated by the solid and dashed blue lines in Fig. 4.7(a). However, the LP scattering rates (red lines) are noticeably affected, displaying a substantial increase at $k = 0$ μm^{-1} for free-standing WSe_2 monolayers. Moreover, the typical step-like increase in scattering rates, characteristic of hBN-encapsulated samples, is absent in the free-standing scenario. The heightened scattering at vanishing momenta is attributed to the screening-induced augmentation of the energy separation between polaritons and dark excitons, facilitating efficient scattering into KΛ excitons via the emission of acoustic phonons. Conversely, the activation of these channels at larger momenta accounts for the step-like behaviour observed

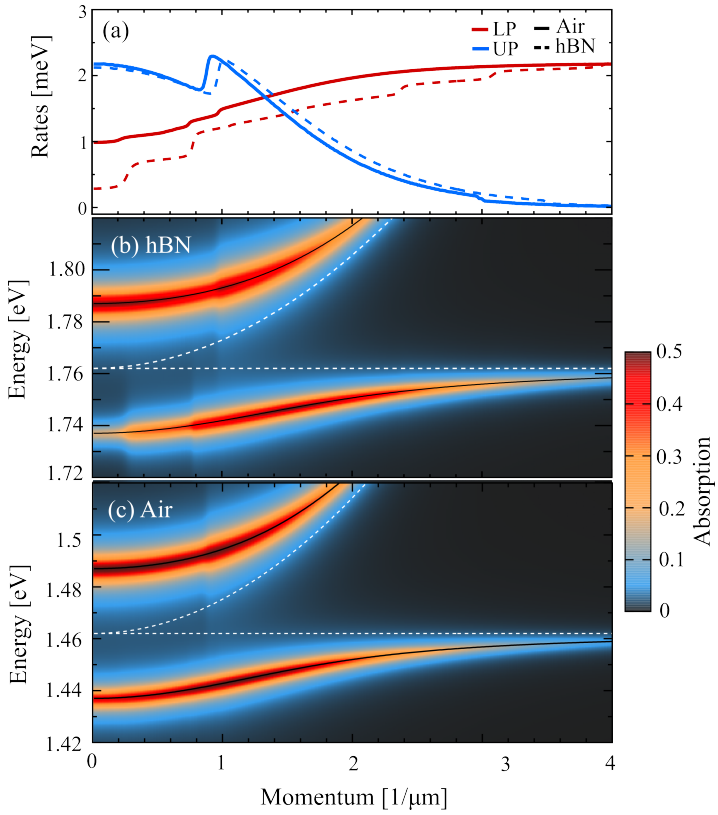


Figure 4.7: (a) Comparison of polariton-phonon scattering rates for hBN-encapsulated and free-standing (air) WSe_2 monolayers for the upper and lower polariton branch (UP/LP). The corresponding polariton absorption for (b) hBN-encapsulated and (c) free-standing WSe_2.

at approximately $k = 0.3$, 0.8 μm^{-1} in the hBN-encapsulated case (dashed red line in Fig.4.7(a)). This results in a more pronounced lower polariton absorption (with an expanded spectral width) at smaller momenta, as shown in Fig.4.7(c).

It is important to note that besides substrate-induced screening, hBN - encapsulation also significantly narrows exciton resonances compared to other substrates [61, 172, 173]. For TMD monolayers in a cavity, the phenomenon known as motional narrowing could compensate for the increase in disorder-related loss in the absence of hBN encapsulation [56, 87, 174]. Motional

narrowing arises from the dynamical averaging of spatial disorder as polaritons propagate across the sample. Due to their hybrid light–matter nature, polaritons can exhibit large group velocities, enabling them to sample multiple disorder configurations on timescales shorter than the dephasing time. This rapid motion effectively reduces disorder-induced broadening compared to localized excitonic states [56, 174]. Importantly, this effect can yield spectra with a reduced impact of disorder while preserving the phonon-induced effects even without hBN encapsulation. In general, the influence of disorder on polaritons is a complex topic, with varying contributions from exciton and photon components [175], potentially adding to the linewidth in addition to cavity decay and scattering with phonons [176]. A more detailed examination of this effect is beyond the scope of our current work but should be considered in future studies.

4.5 Effects of Changing Cavity Length

Adjusting the cavity length in TMD-based devices has proven to be a parameter in controlling the interaction dynamics between lower polariton branches and dark exciton states, particularly in tungsten-based TMDs. By modulating the cavity detuning, which alters the relative energy levels between polaritons and excitons, we can selectively enable or disable phonon-driven scattering channels. This adjustment directly influences the scattering rate Γ, impacting the polariton absorption intensity and linewidth. Optimal absorption occurs under the critical coupling condition, where Γ matches twice the cavity decay rate γ [164].

With appropriate detuning, the lower polariton branch can be manipulated to fall below the dark exciton state, effectively becoming the new ground state. This shift closes the scattering channel between these states, significantly enhancing the material's photoluminescence properties (Fig. 1(d)). This technique has also been employed to brighten materials typically considered optically inactive, showcasing the versatile application of cavity detuning in material science [97].

Our investigations highlight the emergence of distinct, step-like increases in polariton linewidth as detuning is adjusted. These variations correlate

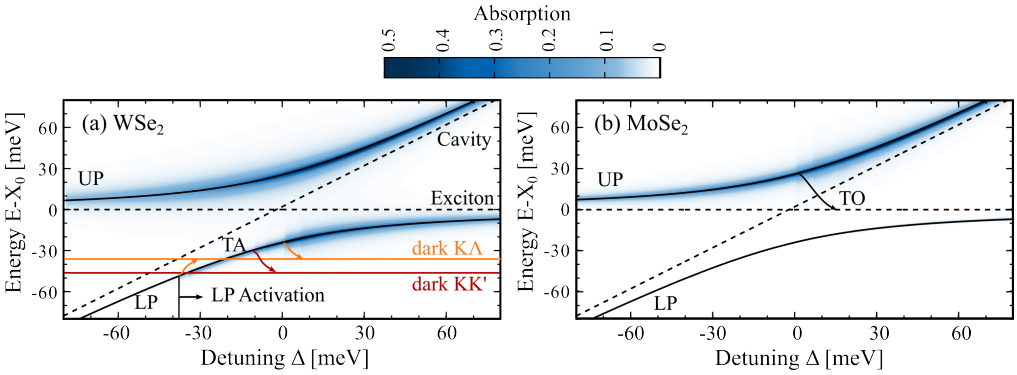


Figure 4.8: Detailed polariton absorption as a function of detuning and energy for WSe_2 and $MoSe_2$, highlighting the differing responses in absorption due to variations in the scattering rate and cavity detuning.

with the activation or suppression of specific dark exciton scattering channels, providing a method to map the exciton energy landscape across different TMD materials. These findings are substantiated by a detailed spectral analysis at 77 K, employing numerical methods to evaluate Equation (2.85) for hBN-encapsulated WSe_2 and $MoSe_2$ within symmetrically configured cavities.

This analysis reveals striking differences in polariton absorption behaviours between tungsten- and molybdenum-based TMDs, as depicted in Fig. 4.8. Despite similar cavity decay rates, the marked contrast in absorption profiles primarily arises from variations in the polariton-phonon scattering rates Γ. $MoSe_2$ exhibits minimal lower polariton branch absorption, especially when far from the critical coupling condition, attributed to the weaker phonon absorption pathways at cryogenic temperatures. Conversely, WSe_2 displays significant absorption enhancements for detunings just below $\Delta = -38$ meV, with sharp increases observed around $\Delta = -10$ and 0 meV. These detunings align with energies that facilitate efficient scattering into dark KK' and KΛ excitons through intervalley phonons, significantly affecting both polariton linewidth and absorption properties.

The upper polariton branches in both WSe_2 and $MoSe_2$ exhibit more uniform absorption profiles across all detuning levels, facilitated by continuous intravalley scattering. However, additional intervalley scattering channels in WSe_2

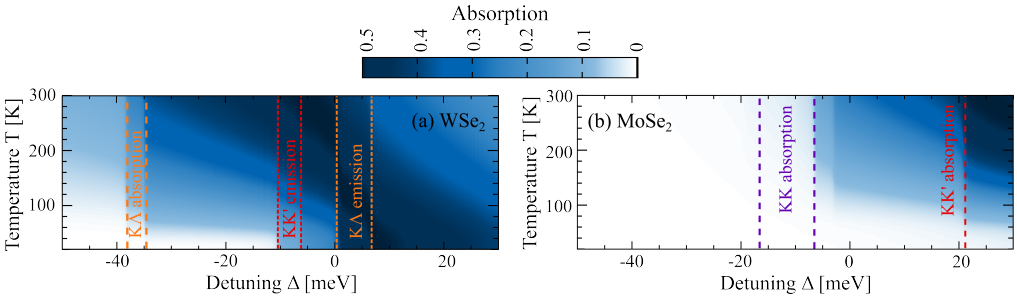


Figure 4.9: Detailed depiction of polariton absorption as a function of detuning and temperature for WSe_2 and $MoSe_2$ monolayers in a cavity, highlighting the influence of temperature and phonon-driven scattering processes.

modestly enhance the absorption, contrasting with the broader linewidth and higher absorption peaks in $MoSe_2$ when intravalley scattering from optical emissions is prevalent.

4.5.1 Temperature-Dependent Polariton Dynamics

Temperature influences polariton absorption by dictating the efficiency of phonon-driven scattering processes, which play a role for the energy transfer between polaritons and dark excitons in TMD monolayers [128]. To elucidate this, we have conducted a comprehensive study on the effects of detuning and temperature on polariton absorption in WSe_2 and $MoSe_2$, as shown in Figure 4.9. Our investigation reveals intriguing behaviours in the absorption spectra of these materials, as depicted in Figure 4.9(a) and (b). We observe distinct regions where polariton absorption is nearly absent, indicated by the white areas in the figure. Notably, WSe_2 demonstrates specific detuning thresholds where the absorption significantly increases. These increments occur at $\Delta = -10$ and 0 meV, correlating with the activation of scattering channels into the dark KK' and KΛ excitons, facilitated by the emission of LA and TA phonons, respectively.

The temperature dependency of these features is relatively modest, remaining visible up to room temperature. However, a more pronounced temperature-dependent absorption increase is noted around $\Delta = -40$ meV. This increase becomes more prominent at temperatures exceeding 100 K, aligning with the

conditions necessary for phonon absorption processes to enable scattering into the higher-energy KΛ states. This behaviour underscores the dynamic interplay between phonon activity and polariton behaviour under varying thermal conditions.

Comparatively, $MoSe_2$ exhibits weaker absorption features across similar detuning ranges. This disparity stems primarily from its band alignment, which restricts phonon-emission-mediated scattering processes essential for enhancing polariton absorption. The phonon absorption channels that are available do not compensate for this deficit, leading to less pronounced absorption increases even under increased temperature conditions.

Interestingly, at higher temperatures, we occasionally observe modest step-like increases in the absorption for $MoSe_2$, linked to thermally activated intravalley optical modes or intervalley phonons targeting the dark KK' valley. These subtle features, marked by purple and red in the spectral data, emphasize the nuanced role of temperature in facilitating or hindering specific phonon-driven scattering processes.

4.5.2 Influence of Scattering Channels on Linewidth

Our investigations have primarily focused on the polariton absorption at zero momentum. To further elucidate the dynamic interplay between momentum, detuning, and polariton absorption, we turn our attention to the behaviours at higher momenta. Figure 4.10(a) illustrates the lower polariton (LP) absorption in WSe_2 at a fixed temperature of 77 K, across various detunings and momenta. It is notable that for negative cavity detuning values and below $k = 2\ \mu m^{-1}$, the absorption is nearly negligible. This minimal absorption is attributed to the requisite polariton access energy necessary to scatter into the dark exciton states. Moreover, the steep dispersion characteristic of the lower polariton enables a clear visualization of how these scattering channels open up as a function of momentum. Crucially, the smaller the negative detuning, the lower the required momentum for such scattering events, with critical detuning values for different channels manifesting at zero in-plane momentum, as detailed in Figure 4.10.

Additionally, our analysis reveals that not only the absorption magnitude

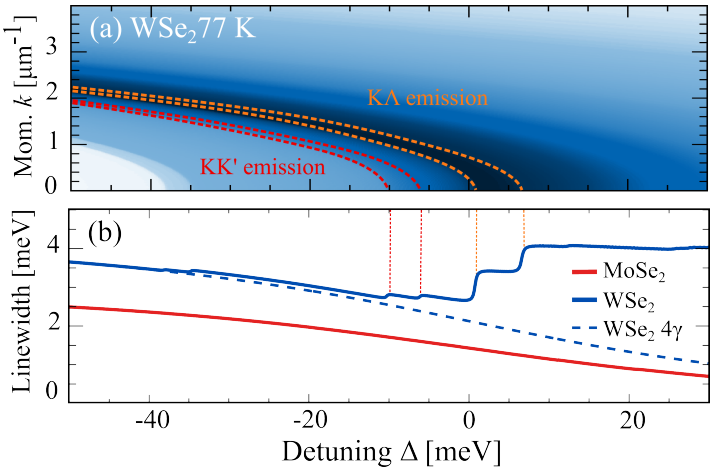


Figure 4.10: Lower polariton absorption of WSe_2 at 77 K as a function of detuning and momentum, highlighting the transition points where scattering channels into dark exciton states become energetically feasible.

but also the spectral linewidth of the lower polariton is highly sensitive to the initiation of detuning-driven polariton-phonon scattering channels, as shown in Figure 4.10(b). For $MoSe_2$, the lower polariton linewidth is largely governed by the cavity decay rate, denoted as 4γ, which correlates with the photonic Hopfield coefficient that decreases as detuning increases. This results in a notably reduced linewidth as detuning increases, depicted by the red line in Figure 4.10(b). A similar trend is observed for WSe_2; however, the onset of specific polariton-phonon scattering channels at certain detuning thresholds precipitates sharp escalations in the LP linewidth, thereby underscoring the intricate relationship between detuning, phonon activity, and polariton properties in these two-dimensional materials.

4.5.3 Polariton Linewidth: Experimental and Theoretical Insights

Polariton linewidth plays a role in understanding the dynamics of polaritons in semiconducting devices, particularly in the context of TMD-based cavities. This section complements the theoretical predictions with cryogenic reflectance measurements of WSe_2 and $MoSe_2$ monolayers in a cavity done by Christian

Scnheider group in Oldenburg University. Utilizing the full spectral tunability of the open cavity, the group mapped the coupling conditions of the two considered samples based on integrated $MoSe_2$ and WSe_2 monolayers. Both experiments reveal a clear anti-crossing behaviour of the upper- and lower polariton branches in the reflection contrast study, featuring a Rabi-splitting of 20 meV for WSe_2 and a slightly reduced Rabi-splitting of 16 meV for $MoSe_2$.

To assess the role of dark excitons in the experiment, the linewidth of the lower polariton resonance was extracted by fitting it with a Fano-type of lineshape and plot the result as a function of detuning. We observe in WSe_2 a series of step-like increases in the polariton linewidth at specific detuning values, notably at approximately -40, 29, and 26 meV. These increments are traced back to the opening of scattering channels toward the dark KΛ exciton via the emission of TA and LA phonons.

To better align with the experimental data, we apply a small downward shift of 6 meV to the theoretically calculated energy of the KΛ excitons. Such adjustments are commonly considered due to the ongoing discussion in the literature regarding the precise energetic ordering of dark excitonic states in TMD monolayers, which depends sensitively on dielectric environment, strain, and many-body effects [3, 173]. Within this context, the applied shift allows the spin-dark exciton energy, indicated by vertical lines in the figure, to coincide with the onset of additional features observed in the polariton linewidth.

Moreover, the study indicates that inhomogeneous broadening plays a significant role in enhancing the exciton scattering rate Γ, as evidenced by the overall increase in polariton linewidth with detuning observed even in the $\Delta \ll 0$ regime. This broadening, potentially caused by macroscopic or micrometric inhomogeneities such as strain in the sample, leads to enhanced exciton scattering independent of temperature or exciton state, supplementing the microscopically calculated polariton-phonon scattering rate.

We describe this inhomogeneous broadening as a temperature—and state-independent exciton scattering rate added to the microscopically calculated polariton-phonon scattering rate to account for the fact that the realistic samples investigated in the experiment include disorder and defects. The

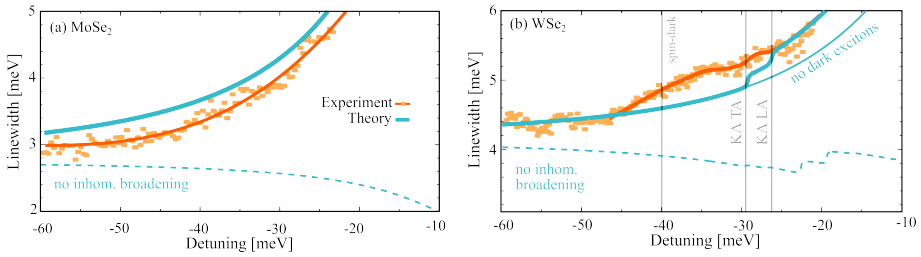


Figure 4.11: Direct experiment-theory comparison. Theoretically predicted (blue line) and experimentally measured (orange dots) lower polariton linewidth obtained from reflection measurements at 20 K for a (a) $MoSe_2$ and (b) WSe_2 monolayer in a cavity. The thin blue line shows the calculated linewidth without scattering into dark exciton states, while the dashed line represents the intrinsic linewidth without inhomogeneous broadening. The vertical black lines denote the energy of spin-dark excitons in experiments as well as the detuning values at which the scattering channels with TA and LA phonons are opened.

equation that describes the inhomogeneous broadening is

$$\Gamma^{In}_{\mathbf{k}} = C^{In}|h^{n}_{\mathrm{X},\mathbf{k}}|^2, \tag{4.1}$$

where C^{In} is a constant and $|h^{n}_{\mathrm{X},\mathbf{k}}|^2$ represents the excitonic Hopfield coefficient. We add this to the microscopically calculated polariton-phonon scattering as $\Gamma^{n}_{\mathbf{k}} \to \Gamma^{n}_{\mathbf{k}} + \Gamma^{In}_{\mathbf{k}}$. For WSe_2, we use the value $C^{In} = 6$ meV, while for $MoSe_2$ it is 13 meV.

To conclude, this chapter has delineated the intricate interplay between polariton dynamics and material properties under varying experimental conditions. Through theoretical modelling and experimental investigations, we have explored how cavity design, environmental factors, and material-specific characteristics influence the absorption properties of polaritons in TMDs. The insights obtained enhance our understanding of polariton behaviour in two-dimensional materials.

CHAPTER 5

Conclusion and Outlook

This thesis has explored the dynamics of exciton-polaritons in transition metal dichalcogenides (TMDs), with a focus on their optical and transport properties, particularly in relation to dark excitons. By employing microscopic modelling, we have gained a deeper understanding of the behaviour of these quasiparticles, especially their diffusion, in atomically thin semiconductors.

The key findings of this work include:

- **Exciton-polariton diffusion**: We developed a theoretical framework that combines the exciton density matrix formalism with the Hopfield model to predict significantly enhanced diffusion coefficients for polaritons compared to bare excitons.
- **Role of dark excitons**: We demonstrated that dark excitons play a crucial role in shaping the optical response of TMDs, with their dynamics influencing the polariton spectra. This highlights the importance of incorporating dark exciton effects into the interpretation of experimental results.

- **Experimental implications**: Confirmation of our theoretical predictions in experiment in collaboration with the group of Christian Schneider, for the influence of dark excitons in polariton systems, paving the way for future applications in quantum computing and advanced photonic devices.

The findings contribute significantly to the understanding of strong light-matter interactions in two-dimensional materials and offer valuable insights for future developments in optoelectronics and quantum technologies.

Future Work:
Future research will focus on advancing our understanding of polariton dynamics, particularly the relaxation times and photoluminescence properties at room temperature. Achieving room-temperature Bose-Einstein condensation (BEC) is a key goal, with significant implications for polariton-based devices and quantum technologies.

A promising direction is the study of the polariton bottleneck, which limits relaxation efficiency at high densities. Early studies, including recent work where I was a co-author, explore the interplay between exciton-polaritons and material limitations. These efforts lay the groundwork for overcoming the bottleneck and achieving room-temperature BEC, improving polariton transport and device performance.

Bibliography

[1] Manish Chhowalla, Hyun Seok Shin, Goki Eda, Lain-Jong Li, Kian Ping Loh, and Hua Zhang. The chemistry of two-dimensional layered transition metal dichalcogenide nanosheets. *Nat. Chem.*, 5(4):263–275, 2013.

[2] Sajedeh Manzeli, Dmitry Ovchinnikov, Daniel Pasquier, Oleg V Yazyev, and Andras Kis. 2D transition metal dichalcogenides. *Nat. Rev. Mater.*, 2:17033, 2017.

[3] Ermin Malic and Andreas Knorr. Exciton dynamics in monolayer transition metal dichalcogenides. *Annu. Rev. Condens. Matter Phys*, 9:355–378, 2018.

[4] X. Liu, T. Galfsky, Z. Sun, F. Xia, E. Lin, Y. H. Lee, S. Kéna-Cohen, and V. M. Menon. Strong light–matter coupling in two-dimensional atomic crystals. *Nat. Phot.*, 9:30–34, 2015.

[5] S Dufferwiel, S Schwarz, F Withers, AAP Trichet, F Li, M Sich, O Del Pozo-Zamudio, C Clark, A Nalitov, DD Solnyshkov, et al. Exciton–polaritons in Van der Waals heterostructures embedded in tunable microcavities. *Nat. Commun.*, 6(1):1–7, 2015.

[6] Christian Schneider, Mikhail M Glazov, Tobias Korn, Sven Höfling, and Bernhard Urbaszek. Two-dimensional semiconductors in the regime of strong light-matter coupling. *Nat. Commun.*, 9(1):1–9, 2018.

[7] Kin Fai Mak, Changgu Lee, James Hone, Jie Shan, and Tony F Heinz. Atomically thin MoS_2: A new direct-gap semiconductor. *Phys. Rev. Lett.*, 105(13):136805, 2010.

[8] Xiaodong Xu, Wang Yao, Di Xiao, and Tony F Heinz. Spin and pseudospins in layered transition metal dichalcogenides. *Nat. Phys.*, 10(5):343–350, 2014.

[9] Kin Fai Mak, Keliang He, Jie Shan, and Tony F. Heinz. Control of valley polarization in monolayer MoS_2 by optical helicity. *Nat. Nanotechnol.*, 7:494–498, 2012.

[10] Abhijeet M Kumar, Denis Yagodkin, Roberto Rosati, Douglas J Bock, Christoph Schattauer, Sarah Tobisch, Joakim Hagel, Bianca Höfer, Jan N Kirchhof, Pablo Hernández López, et al. Strain fingerprinting of exciton valley character in 2D semiconductors. *Nat. Commun.*, 15(1):7546, 2024.

[11] Abhijeet M Kumar, Douglas J Bock, Denis Yagodkin, Edith Wietek, Bianca Hofer, Max Sinner, Adrián Dewambrechies, Pablo Hernández López, Sviatoslav Kovalchuk, Raghav Dhingra, et al. Strain control of valley polarization dynamics in a 2D semiconductor via exciton hybridization. *Nano Lett.*, 25(42):15164–15172, 2025.

[12] John R Schaibley, Hongyi Yu, Genevieve Clark, Pasqual Rivera, Jason S Ross, Kyle L Seyler, Wang Yao, and Xiaodong Xu. Valleytronics in 2D materials. *Nat. Rev. Mater.*, 1(11):16055, 2016.

[13] Qing Hua Wang, Kourosh Kalantar-Zadeh, Andras Kis, Jonathan N Coleman, and Michael S Strano. Electronics and optoelectronics of two-dimensional transition metal dichalcogenides. *Nat. Nanotechnol.*, 7(11):699–712, 2012.

[14] Deji Akinwande, Nicholas Petrone, and James Hone. Two-dimensional flexible nanoelectronics. *Nature Commun.*, 5(1):5678, 2014.

[15] Gunnar Berghäuser, Philipp Steinleitner, Philipp Merkl, Rupert Huber, Andreas Knorr, and Ermin Malic. Mapping of the dark exciton landscape in transition metal dichalcogenides. *Phys. Rev. B*, 98:020301, Jul 2018.

[16] Ermin Malic, Malte Selig, Maja Feierabend, Samuel Brem, Dominik Christiansen, Florian Wendler, Andreas Knorr, and Gunnar Berghäuser. Dark excitons in transition metal dichalcogenides. *Phys. Rev. Mater.*, 2:014002, 2018.

[17] Thorsten Deilmann and Kristian Sommer Thygesen. Finite-momentum exciton landscape in mono- and bilayer transition metal dichalcogenides. *2D Mater.*, 6(3):035003, 2019.

[18] Galan Moody, Chandriker Kavir Dass, Kai Hao, Chang-Hsiao Chen, Lain-Jong Li, Akshay Singh, Kha Tran, Genevieve Clark, Xiaodong Xu, Gunnar Berghäuser, et al. Intrinsic homogeneous linewidth and broadening mechanisms of excitons in monolayer transition metal dichalcogenides. *Nat. Commun.*, 6(1):1–6, 2015.

[19] Malte Selig, Gunnar Berghäuser, Archana Raja, Philipp Nagler, Christian Schüller, Tony F. Heinz, Tobias Korn, Alexey Chernikov, Ermin Malic, and Andreas Knorr. Excitonic linewidth and coherence lifetime in monolayer transition metal dichalcogenides. *Nat. Commun.*, 7(1):13279, Nov 2016.

[20] Maciej R Molas, Clement Faugeras, Autur O Slobodeniuk, Karol Nogajewski, Miroslav Bartos, DM Basko, and Marek Potemski. Brightening of dark excitons in monolayers of semiconducting transition metal dichalcogenides. *2D Mat.*, 4(2):021003, 2017.

[21] You Zhou, Giovanni Scuri, Dominik S Wild, Alexander A High, Alan Dibos, Luis A Jauregui, Chi Shu, Kristiaan De Greve, Kateryna Pistunova, Andrew Y Joe, et al. Probing dark excitons in atomically thin semiconductors via near-field coupling to surface plasmon polaritons. *Nat. Nanotechnol.*, 12(9):856–860, 2017.

[22] Malte Selig, Florian Katsch, Samuel Brem, Garnik F Mkrtchian, Ermin Malic, and Andreas Knorr. Suppression of intervalley exchange coupling in the presence of momentum-dark states in transition metal dichalcogenides. *Phys. Rev. Res.*, 2(2):023322, 2020.

[23] Daniel Erkensten, Samuel Brem, Koloman Wagner, Roland Gillen, Raül Perea-Causín, Jonas D. Ziegler, Takashi Taniguchi, Kenji Watanabe, Janina Maultzsch, Alexey Chernikov, and Ermin Malic. Dark exciton-exciton annihilation in monolayer WSe_2. *Phys. Rev. B*, 104:L241406, Dec 2021.

[24] Koloman Wagner, Jonas Zipfel, Roberto Rosati, Edith Wietek, Jonas D. Ziegler, Samuel Brem, Raül Perea-Causín, Takashi Taniguchi, Kenji Watanabe, Mikhail M. Glazov, Ermin Malic, and Alexey Chernikov. Nonclassical exciton diffusion in monolayer WSe_2. *Phys. Rev. Lett.*, 127:076801, Aug 2021.

[25] Roberto Rosati, Raül Perea-Causín, Samuel Brem, and Ermin Malic. Negative effective excitonic diffusion in monolayer transition metal dichalcogenides. *Nanoscale*, 12(1):356–363, 2020.

[26] Roberto Rosati, Samuel Brem, Raül Perea-Causín, Robert Schmidt, Iris Niehues, Steffen Michaelis de Vasconcellos, Rudolf Bratschitsch, and Ermin Malic. Strain-dependent exciton diffusion in transition metal dichalcogenides. *2D Mat.*, 8(1):015030, 2020.

[27] Roberto Rosati, Koloman Wagner, Samuel Brem, Raül Perea-Causín, Jonas D Ziegler, Jonas Zipfel, Takashi Taniguchi, Kenji Watanabe, Alexey Chernikov, and Ermin Malic. Non-equilibrium diffusion of dark excitons in atomically thin semiconductors. *Nanoscale*, 13(47):19966–19972, 2021.

[28] Marvin Kulig, Jonas Zipfel, Philipp Nagler, Sofia Blanter, Christian Schüller, Tobias Korn, Nicola Paradiso, Mikhail M. Glazov, and Alexey Chernikov. Exciton diffusion and halo effects in monolayer semiconductors. *Phys. Rev. Lett.*, 120:207401, May 2018.

[29] Raül Perea-Causín, Samuel Brem, Roberto Rosati, Roland Jago, Marvin Kulig, Jonas D. Ziegler, Jonas Zipfel, Alexey Chernikov, and Ermin Malic. Exciton propagation and halo formation in two-dimensional materials. *Nano Lett.*, 19(10):7317–7323, Oct 2019.

[30] M. M. Glazov. Phonon wind and drag of excitons in monolayer semiconductors. *Phys. Rev. B*, 100:045426, Jul 2019.

[31] Roberto Rosati, Robert Schmidt, Samuel Brem, Rodolfo Perea-Causin, Iris Niehues, Julian Kern, et al. Dark exciton anti-funneling in atomically thin semiconductors. *Nat. Commun.*, 12:7221, 2021.

[32] Ermin Malic, Raul Perea-Causin, Roberto Rosati, Daniel Erkensten, and Samuel Brem. Exciton transport in atomically thin semiconductors. *Nat. Commun.*, 14:3430, 2023.

[33] Xidong Duan, Chen Wang, Jonathan C. Shaw, Rui Cheng, Yu Chen, Honglai Li, Xueping Wu, Ying Tang, Qinling Zhang, Anlian Pan, Jianhui Jiang, Ruqing Yu, Yu Huang, and Xiangfeng Duan. Lateral epitaxial growth of two-dimensional layered semiconductor heterojunctions. *Nat. Nanotechnol.*, 9(12):1024–1030, Dec 2014.

[34] Yongji Gong, Junhao Lin, Xingli Wang, Gang Shi, Sidong Lei, Zhong Lin, Xiaolong Zou, Gonglan Ye, Robert Vajtai, Boris I. Yakobson, Humberto Terrones, Mauricio Terrones, Beng Kang Tay, Jun Lou, Sokrates T. Pantelides, Zheng Liu, Wu Zhou, and Pulickel M. Ajayan. Vertical and in-plane heterostructures from WS_2/MoS_2 monolayers. *Nat. Mater.*, 13(12):1135–1142, Dec 2014.

[35] Chunming Huang, Sanfeng Wu, Ana M. Sanchez, Jonathan J. P. Peters, Richard Beanland, Jason S. Ross, Pasqual Rivera, Wang Yao, David H. Cobden, and Xiaodong Xu. Lateral heterojunctions within monolayer $MoSe_2$–WSe_2 semiconductors. *Nat. Mater.*, 13(12):1096–1101, Dec 2014.

[36] Ka Wai Lau, Calvin, Zhirui Gong, Hongyi Yu, and Wang Yao. Interface excitons at lateral heterojunctions in monolayer semiconductors. *Phys. Rev. B*, 98:115427, Sep 2018.

[37] David Schmitt, Jan Philipp Bange, Wiebke Bennecke, AbdulAziz AlMutairi, Giuseppe Meneghini, Kenji Watanabe, Takashi Taniguchi, Daniel Steil, D Russell Luke, R Thomas Weitz, et al. Formation of moiré interlayer excitons in space and time. *Nature*, 608(7923):499–503, 2022.

[38] Roberto Rosati, Ioannis Paradisanos, Le Huang, Zhengqing Gan, Antony George, Ken Watanabe, et al. Interface engineering of charge-transfer excitons in 2D lateral heterostructures. *Nat. Commun.*, 14:2438, 2023.

[39] Jan Philipp Bange, David Schmitt, Wiebke Bennecke, Giuseppe Meneghini, AbdulAziz AlMutairi, Kenji Watanabe, Takashi Taniguchi, Daniel

Steil, Sabine Steil, R Thomas Weitz, et al. Probing electron-hole coulomb correlations in the exciton landscape of a twisted semiconductor heterostructure. *Sci. Adv.*, 10(6):eadi1323, 2024.

[40] Qiaoling Lin, Hanlin Fang, Alexei Kalaboukhov, Yuanda Liu, Yi Zhang, Moritz Fischer, Juntao Li, Joakim Hagel, Samuel Brem, Ermin Malic, et al. Moiré-engineered light-matter interactions in MoS/WSe_2 heterobilayers at room temperature. *Nat. Commun.*, 15(1):8762, 2024.

[41] Shuchen Zhang, Linrui Jin, Yuan Lu, Linghai Zhang, Jiaqi Yang, Qiuchen Zhao, Dewei Sun, Joshua JP Thompson, Biao Yuan, Ke Ma, et al. Moiré superlattices in twisted two-dimensional halide perovskites. *Nat. Mat.*, 23(9):1222–1229, 2024.

[42] Roberto Rosati, Sai Shradha, Julian Picker, Andrey Turchanin, Bernhard Urbaszek, and Ermin Malic. Impact of charge-transfer excitons on unidirectional exciton transport in lateral tmd heterostructures. *Nano Lett.*, 25(29):11319–11324, 2025.

[43] S Shradha, R Rosati, H Lamsaadi, J Picker, I Paradisanos, Md T Hossain, L Krelle, LF Oswald, N Engel, DI Markina, et al. 2D excitonics with atomically thin lateral heterostructures. *Rep. Prog. Phys.*, 89(4):046501, 2026.

[44] Philipp Merkl, Fabian Mooshammer, Samuel Brem, Anna Girnghuber, Kai-Qiang Lin, Leonard Weigl, Marlene Liebich, Chaw-Keong Yong, Roland Gillen, Janina Maultzsch, et al. Twist-tailoring coulomb correlations in van der waals homobilayers. *Nature Commun.*, 11(1):1–7, 2020.

[45] Samuel Brem, Kai-Qiang Lin, Roland Gillen, Jonas M Bauer, Janina Maultzsch, John M Lupton, and Ermin Malic. Hybridized intervalley moiré excitons and flat bands in twisted WSe_2 bilayers. *Nanoscale*, 12(20):11088–11094, 2020.

[46] Joakim Hagel, Samuel Brem, Christopher Linderälv, Paul Erhart, and Ermin Malic. Exciton landscape in van der waals heterostructures. *Phys. Rev. Res.*, 3(4):043217, 2021.

[47] Robert Wallauer, Raul Perea-Causin, Lasse Münster, Sarah Zajusch, Samuel Brem, Jens Güdde, Katsumi Tanimura, Kai-Qiang Lin, Rupert

Huber, Ermin Malic, et al. Momentum-resolved observation of exciton formation dynamics in monolayer WS_2. *Nano Lett.*, 21(13):5867–5873, 2021.

[48] Long Yuan, Biyuan Zheng, Qiuchen Zhao, Roman Kempt, Thomas Brumme, Agnieszka B Kuc, Chao Ma, Shibin Deng, Anlian Pan, and Libai Huang. Strong dipolar repulsion of one-dimensional interfacial excitons in monolayer lateral heterojunctions. *ACS nano*, 17(16):15379–15387, 2023.

[49] Dorian Beret, Ioannis Paradisanos, Hassan Lamsaadi, Ziyang Gan, Emad Najafidehaghani, Antony George, Tibor Lehnert, Johannes Biskupek, Ute Kaiser, Shivangi Shree, et al. Exciton spectroscopy and unidirectional transport in $MoSe_2$-WSe_2 lateral heterostructures encapsulated in hexagonal boron nitride. *NPJ 2D Mater. Appl*, 6(1):1–8, 2022.

[50] Jamie M Fitzgerald, Joshua JP Thompson, and Ermin Malic. Twist angle tuning of moiré exciton polaritons in van der waals heterostructures. *Nano Lett.*, 22(11):4468–4474, 2022.

[51] Raul Perea-Causin, Daniel Erkensten, Jamie M Fitzgerald, Joshua JP Thompson, Roberto Rosati, Samuel Brem, and Ermin Malic. Exciton optics, dynamics, and transport in atomically thin semiconductors. *APL Mater.*, 10(10):100701, 2022.

[52] S. Zhang, S. Y. Park, D. H. Lee, and A. Javey. Scalable synthesis of monolayer transition metal dichalcogenides: a review. *Adv. Mater.*, 30(30):1800492, 2018.

[53] A. Du, S. Wu, B. C. H., H. Li, and H. Yang. 2D materials: from exfoliation to device applications. *Nat. Rev. Mater.*, 3:90–103, 2018.

[54] C. Weisbuch, M. Nishioka, A. Ishikawa, and Y. Arakawa. Observation of the coupled exciton-photon mode splitting in a semiconductor quantum microcavity. *Phys. Rev. Lett.*, 69(23):3314–3317, 1992.

[55] Kerry J. Vahala. Optical microcavities. *Nature*, 424:839–846, 2003.

[56] Alexey Kavokin, Jeremy J. Baumberg, Guillaume Malpuech, and Fabrice P. Laussy. *Microcavities*. Oxford University Press, 2007.

[57] Amnon Yariv and Pochi Yeh. *Photonics: Optical Electronics in Modern Communications*. Oxford University Press, 6 edition, 2006.

[58] Max Born and Emil Wolf. *Principles of Optics*. Cambridge University Press, 7 edition, 1999.

[59] Hui Deng, Hartmut Haug, and Yoshihisa Yamamoto. Exciton-polariton Bose-Einstein condensation. *Rev. Mod. Phys.*, 82(2):1489, 2010.

[60] Christian Schneider et al. Bose–einstein condensation of exciton polaritons in microcavities. *Nature Materials*, 16(11):1154–1160, 2017.

[61] F. Cadiz, E. Courtade, C. Robert, G. Wang, Y. Shen, H. Cai, T. Taniguchi, K. Watanabe, H. Carrere, D. Lagarde, M. Manca, T. Amand, P. Renucci, S. Tongay, X. Marie, and B. Urbaszek. Excitonic linewidth approaching the homogeneous limit in MoS_2-based van der Waals heterostructures. *Phys. Rev. X*, 7:021026, May 2017.

[62] Jacek Kasprzak, Murielle Richard, S Kundermann, A Baas, P Jeambrun, Jonathan Mark James Keeling, FM Marchetti, MH Szymańska, R André, JL Staehli, et al. Bose–Einstein condensation of exciton polaritons. *Nature*, 443(7110):409–414, 2006.

[63] Xuekai Ma, Bernd Berger, Marc Aßmann, Rodislav Driben, Torsten Meier, Christian Schneider, Sven Höfling, and Stefan Schumacher. Realization of all-optical vortex switching in exciton-polariton condensates. *Nat. Commun.*, 11(1):1–7, 2020.

[64] Carlos Anton-Solanas, Maximilian Waldherr, Martin Klaas, Holger Suchomel, Tristan H Harder, Hui Cai, Evgeny Sedov, Sebastian Klembt, Alexey V Kavokin, Sefaattin Tongay, et al. Bosonic condensation of exciton-polaritons in an atomically thin crystal. *Nat. Mat.*, 20:1233–1239, 2021.

[65] Oskar Painter, Richard K. Lee, Axel Scherer, Amnon Yariv, Jeremy D. O'Brien, P. Daniel Dapkus, and Il-Hyun Kim. Two-dimensional photonic band-gap defect mode laser. *Science*, 284(5421):1819–1821, 1999.

[66] Susumu Noda, Masaya Fujita, and Takashi Asano. Spontaneous-emission control by photonic crystals and nanocavities. *Nat. Phot.*, 1:449–458, 2007.

[67] Long Yuan. *Spatial and Temporal Imaging of Exciton Dynamics and Transport in Two-Dimensional Semiconductors and Heterostructures by Ultrafast Transient Absorption Microscopy.* PhD thesis, Purdue University, 2023.

[68] PJ Dean, B Fischer, DC Herbert, J Lagois, and PY Yu. *Excitons*, volume 14. Springer Science & Business Media, 2012.

[69] Hartmut Haug and Stephan W Koch. *Quantum theory of the optical and electronic properties of semiconductors.* World Scientific Publishing Company, 2009.

[70] A. S. Davydov. *Theory of Molecular Excitons.* Springer, 1971.

[71] V. M. Agranovich and D. M. Basko. *Organic Semiconductors and Hybrid Systems.* Springer, 2009.

[72] R. Rosati, I. Paradisanos, E. Malic, and B. Urbaszek. *Two dimensional semiconductors: Optical and electronic properties*, volume 1, pages 312–351. Elsevier, UK, second edition edition, 2025.

[73] Gunnar Berghäuser and Ermin Malic. Analytical approach to excitonic properties of MoS_2. *Phys. Rev. B*, 89(12):125309, 2014.

[74] Gang Wang, Alexey Chernikov, Mikhail M. Glazov, Tony F. Heinz, Xavier Marie, Thierry Amand, and Bernhard Urbaszek. Colloquium: Excitons in atomically thin transition metal dichalcogenides. *Rev. Mod. Phys.*, 90(2):021001, 2018.

[75] Daniel Vaquero, Cédric A Cordero-Silis, Daniel Erkensten, Roberto Rosati, Martijn H Takens, Kenji Watanabe, Takashi Taniguchi, Ermin Malic, and Marcos HD Guimarães. Valley-controlled many-body exciton interactions in monolayer WSe_2 phototransistors. *Nano Lett.*, 2026.

[76] Jonas Jähnert, Samuel Brem, Riccardo Rosati, and Ermin Malic. Hybrid excitons in transition metal dichalcogenide heterostructures. *2D Mat.*, 10(3):035012, 2023.

[77] Obafunso A Ajayi, Jenny V Ardelean, Gabriella D Shepard, Jue Wang, Abhinandan Antony, Takeshi Taniguchi, Kenji Watanabe, Tony F Heinz, Stefan Strauf, X-Y Zhu, and James C Hone. On the influence of

reabsorption on the decay of fluorescence in molecular crystals. *Optika i Spectr.*, 3(3):84, 1957.

[78] JJ Hopfield. Theory of the contribution of excitons to the complex dielectric constant of crystals. *Phys. Rev.*, 112(5):1555, 1958.

[79] DL Mills and E Burstein. Polaritons: the electromagnetic modes of media. *Rep. Prog. Phys.*, 37(7):817, 1974.

[80] JM Pitarke, VM Silkin, EV Chulkov, and PM Echenique. Theory of surface plasmons and surface-plasmon polaritons. *Rep. Prog. Phys*, 70(1):1, 2006.

[81] D. N. Basov, A. Asenjo-Garcia, P. J. Schuck, X. Zhu, and A. Rubio. Polariton panorama. *Nanophotonics*, 10(1):549–577, 2021.

[82] Zubin Jacob. Hyperbolic phonon–polaritons. *Nat. Mater.*, 13(12):1081–1083, 2014.

[83] Dengke Zhang, Xiao-Qing Luo, Yi-Pu Wang, Tie-Fu Li, and JQ You. Observation of the exceptional point in cavity magnon-polaritons. *Nat. Commun.*, 8(1):1–6, 2017.

[84] Iacopo Carusotto and Cristiano Ciuti. Quantum fluids of light. *Rev. Mod. Phys.*, 85(1):299–366, 2013.

[85] Mark Steger, Gangqiang Liu, Bryan Nelsen, Chitra Gautham, David W Snoke, Ryan Balili, Loren Pfeiffer, and Ken West. Long-range ballistic motion and coherent flow of long-lifetime polaritons. *Phys. Rev. B*, 88(23):235314, 2013.

[86] J Vondran, F Spitzer, M Bayer, IA Akimov, A Trautmann, M Reichelt, C Meier, N Weber, T Meier, R André, et al. Spatially asymmetric transients of propagating exciton-polariton modes in a planar CdZnTe/CdMgTe guiding structure. *Phys. Rev. B*, 100(15):155308, 2019.

[87] M. Wurdack, E. Estrecho, S. Todd, T. Yun, M. Pieczarka, S. K. Earl, J. A. Davis, C. Schneider, A. G. Truscott, and E. A. Ostrovskaya. Motional narrowing, ballistic transport, and trapping of room-temperature exciton–polaritons in an atomically-thin semiconductor. *Nat. Commun.*, 12(1):5366, Sep 2021.

[88] Jamie M Fitzgerald, Roberto Rosati, and Ermin Malic. Polariton transport in 2D semiconductors: Phonon-mediated transitions between ballistic, superdiffusive, and exciton-limited regimes. *Sci. Adv.*, 11(46):eaea3495, 2025.

[89] Dario Ballarini, Milena De Giorgi, Emiliano Cancellieri, Romuald Houdré, Elisabeth Giacobino, Roberto Cingolani, Alberto Bramati, Giuseppe Gigli, and Daniele Sanvitto. All-optical polariton transistor. *Nat. Commun.*, 4(1):1–8, 2013.

[90] German V Kolmakov, Leonid M Pomirchi, and Roman Ya Kezerashvili. Toward room-temperature superfluidity of exciton–polaritons in an optical microcavity with an embedded MoS_2 monolayer. *JOSA B*, 33(7):C72–C79, 2016.

[91] Alberto Amo and Jacqueline Bloch. Exciton-polaritons in semiconductor microcavities: Toward applications in optoelectronics. *C. R. Phys.*, 17(8):934–945, 2016.

[92] Daniele Sanvitto and Stéphane Kéna-Cohen. The road towards polaritonic devices. *Nat. Mat.*, 15(10):1061–1073, 2016.

[93] Hangyong Shan, Jamie M Fitzgerald, Roberto Rosati, Gilbert Leibeling, Kenji Watanabe, Takashi Taniguchi, Seth Ariel Tongay, Falk Eilenberger, Martin Esmann, Sven Höfling, et al. Tuning relaxation and nonlinear upconversion of valley-exciton-polaritons in a monolayer semiconductor. *Nat. Commun.*, 16(1):9700, 2025.

[94] Tim Byrnes, Na Young Kim, and Yoshihisa Yamamoto. Exciton-polariton condensates. *Nat. Phys.*, 10:803–813, 2014.

[95] G. M. Turner et al. Investigating the polariton dispersion in 2D materials. *Nat. Commun.*, 8(1):1–7, 2017.

[96] Masayuki Ueta and Kojiro Uchinokura. Time-resolved luminescence of exciton polaritons in pbi_2. *Phys. Rev. B*, 57(7):3714–3719, 1998.

[97] Hangyong Shan, Ivan Iorsh, Bo Han, Christoph Rupprecht, Heiko Knopf, Falk Eilenberger, Martin Esmann, Kentaro Yumigeta, Kenji Watanabe, Takashi Taniguchi, et al. Brightening of a dark monolayer semiconductor

via strong light-matter coupling in a cavity. *Nat. Comm.*, 13(1):1–7, 2022.

[98] Lucas C Flatten, Zhengyu He, David M Coles, Aurelien AP Trichet, Alex W Powell, Robert A Taylor, Jamie H Warner, and Jason M Smith. Room-temperature exciton-polaritons with two-dimensional WS_2. *Sci. Rep.*, 6(1):1–7, 2016.

[99] S. Wang, S. Li, T. Chervy, A. Shalabney, S. Azzini, E. Orgiu, J. A. Hutchison, C. Genet, P. Samorì, and T. W. Ebbesen. Coherent coupling of WS_2 monolayers with metallic photonic nanostructures at room temperature. *Nano Lett*, 16:4368–4374, 2016.

[100] Bo Han, Jamie M Fitzgerald, Lukas Lackner, Roberto Rosati, Martin Esmann, Falk Eilenberger, Takashi Taniguchi, Kenji Watanabe, Marcin Syperek, Ermin Malic, et al. Infrared magnetopolaritons in mote 2 monolayers and bilayers. *Phys. Rev. Lett.*, 134(7):076902, 2025.

[101] Peter C Waterman. Symmetry, unitarity, and geometry in electromagnetic scattering. *Phys. Rev. D*, 3(8):825, 1971.

[102] Michael I Mishchenko, Joop W Hovenier, and Larry D Travis. *Light Scattering by Nonspherical Particles: Theory, Measurements, and Applications*. Academic Press, 2000.

[103] Crispin W. Gardiner and Peter Zoller. *Quantum Noise: A Handbook of Markovian and Non-Markovian Quantum Stochastic Methods with Applications to Quantum Optics*. Springer Science & Business Media, 2004.

[104] D. Boyanovsky and D. Jasnow. Heisenberg-langevin vs quantum master equation. *Phys. Rev. D*, 53(7):1849–1862, 1996.

[105] Daniel F Walls and Gerard J Milburn. *Quantum Optics*. Springer, 2008.

[106] Aashish A Clerk, Michel H Devoret, Steven M Girvin, Florian Marquardt, and Robert J Schoelkopf. Introduction to quantum noise, measurement, and amplification. *Rev. Mod. Phys*, 82(2):1155, 2010.

[107] Vincenzo Savona. Theory of polariton scattering in semiconductor microcavities. *Solid State Commun.*, 112(5):343–347, 1999.

[108] Crispin W. Gardiner and M. J. Collett. Input and output in damped quantum systems: Quantum stochastic differential equations and the master equation. *Phy. Rev. A*, 31(6):3761–3774, 1985.

[109] Henrik Bruus and Karsten Flensberg. *Many-Body Quantum Theory in Condensed Matter Physics: An Introduction*. Oxford University Press, 2004.

[110] E. Malic and A. Knorr. *Graphene and Carbon Nanotubes: Ultrafast Optics and Relaxation Dynamics*. Wiley, John & Sons, 2013.

[111] Alexander L. Fetter and John Dirk Walecka. *Quantum Theory of Many-Particle Systems*. McGraw-Hill, 1971.

[112] Gerald D. Mahan. *Many-Particle Physics*. Springer US, 2000.

[113] Neil W. Ashcroft and N. David Mermin. *Solid State Physics*. Holt, Rinehart and Winston, 1976.

[114] Walter A. Harrison. *Electronic Structure and the Properties of Solids: The Physics of the Chemical Bond*. Dover Publications, Mineola, NY, 1980.

[115] Charles Kittel and Paul McEuen. *Introduction to solid state physics*. John Wiley & Sons, 2018.

[116] J. M. Riley, L. Bawden, A. N. Grubišić Čabo, M. S. Meevasana, S. S. Rajan, Y.-L. Lee, A. Ceaser, R. W. C. Leake, K. A. Kopieva, J. S. Moon, N. S. Plumb, C. H. Kim, J. Alexander, M. H. Kang, Y.-Y. Wang, C. M. Yim, S.-K. Mo, D. Lu, Z.-X. Shen, and H. F. King. Direct observation of the band structure and spin texture of monolayer WS_2. *Nat. Phys.*, 10:835–839, 2014.

[117] Andrea Splendiani, Liang Sun, Yuanbo Zhang, Tianshu Li, Jonghwan Kim, Chi-Yung Chim, Giulia Galli, and Feng Wang. Emerging photoluminescence in monolayer MoS_2. *Nano Lett.*, 10(4):1271–1275, 2010.

[118] Filip A Rasmussen and Kristian S Thygesen. Computational 2D materials database: electronic structure of transition-metal dichalcogenides and oxides. *J. Phys. Chem. C*, 119(23):13169–13183, 2015.

[119] Andor Kormányos, Guido Burkard, Martin Gmitra, Jaroslav Fabian, Viktor Zólyomi, Neil D Drummond, and Vladimir Fal'ko. k·p theory for two-dimensional transition metal dichalcogenide semiconductors. *2D Mat.*, 2(2):022001, apr 2015.

[120] Wolfgang Nolting and William D Brewer. *Fundamentals of Many-body Physics*. Springer, 2008.

[121] Mackillo Kira and Stephan W. Koch. *Semiconductor Quantum Optics*. Cambridge University Press, Cambridge, 2011.

[122] Zhenghe Jin, Xiaodong Li, Jeffrey T. Mullen, and Ki Wook Kim. Intrinsic transport properties of electrons and holes in monolayer transition-metal dichalcogenides. *Phys. Rev. B*, 90:045422, Jul 2014.

[123] Ronald S Knox. *Theory of Excitons*. Academic Press, New York, 1963.

[124] Alexey Chernikov, Timothy C. Berkelbach, Heather M. Hill, Albert Rigosi, Yilei Li, Ozgur Burak Aslan, David R. Reichman, Mark S. Hybertsen, and Tony F. Heinz. Exciton binding energy and nonhydrogenic rydberg series in monolayer WS_2. *Phys. Rev. Lett.*, 113(7):076802, 2014.

[125] N. S. Rytova. The screened potential of a point charge in a thin film. *Proceedings of the MSU*, 1967.

[126] L. V. Keldysh. Coulomb interaction in thin semiconductor and semimetal films. *JETP Lett.*, 1979.

[127] Pierluigi Cudazzo, Ilya V. Tokatly, and Angel Rubio. Dielectric screening in two-dimensional insulators: Implications for excitonic and impurity states in graphane. *Phys. Rev. B*, 84(8):085406, 2011.

[128] Samuel Brem, Jonas Zipfel, Malte Selig, Archana Raja, Lutz Waldecker, Jonas D Ziegler, Takashi Taniguchi, Kenji Watanabe, Alexey Chernikov, and Ermin Malic. Intrinsic lifetime of higher excitonic states in tungsten diselenide monolayers. *Nanoscale*, 11(25):12381–12387, 2019.

[129] J. M. Ziman. *Principles of the Theory of Solids*. Cambridge University Press, Cambridge, 1972.

[130] G. Grimvall. *The Electron-Phonon Interaction in Metals*. North-Holland, Amsterdam, 1981.

[131] T. Sohier, M. Calandra, and F. Mauri. Phonon-limited electron mobility in MoS_2 and WS_2 from first principles. *Phys. Rev. B*, 94:085415, 2016.

[132] F. Giustino. Electron-phonon interactions from first principles. *Rev. Mod. Phys.*, 89:015003, 2017.

[133] C.-H. Park and S. G. Louie. Electron-phonon interactions and their implications for electronic transport in monolayer transition metal dichalcogenides. *Nano Lett.*, 14:1113–1119, 2014.

[134] C. Cohen-Tannoudji, J. Dupont-Roc, and G. Grynberg. *Photons and Atoms: Introduction to Quantum Electrodynamics*. Wiley, New York, 1989.

[135] J. J. Sakurai. *Modern Quantum Mechanics*. Addison-Wesley, Reading, MA, revised edition, 1994.

[136] J. D. Jackson. *Classical Electrodynamics*. John Wiley & Sons, New York, 3rd edition, 1999.

[137] Andrea Splendiani, Liang Sun, Yuan Zhang, Tongfang Li, Jung Kim, Chul Hoon Chim, Giulia Galli, and Feng Wang. Emerging photoluminescence in monolayer MoS_2. *Nano Lett.*, 10(4):1271–1275, 2010.

[138] Howard J. Carmichael. *Statistical Methods in Quantum Optics 2: Non-Classical Fields*. Springer, Berlin, Heidelberg, 2009.

[139] Serge Haroche and Jean-Michel Raimond. *Exploring the Quantum: Atoms, Cavities, and Photons*. Oxford University Press, 2006.

[140] Howard J Carmichael. *An Open Systems Approach to Quantum Optics*. Springer-Verlag, Berlin, Heidelberg, 1991.

[141] Monique Combescot and Shiue-Yuan Shiau. *Excitons and Cooper pairs: two composite bosons in many-body physics*. Oxford University Press, 2015.

[142] Thomas Mueller and Ermin Malic. Exciton physics and device application of two-dimensional transition metal dichalcogenide semiconductors. *NPJ 2D Mater. Appl*, 2(1):29, Sep 2018.

[143] Keliang He, Nardeep Kumar, Liang Zhao, Zefang Wang, Kin Fai Mak, Hui Zhao, and Jie Shan. Tightly bound excitons in monolayer WSe_2. *Phys. Rev. Lett.*, 113(2):026803, 2014.

[144] Miguel M Ugeda, Aaron J Bradley, Su-Fei Shi, H Felipe, Yi Zhang, Diana Y Qiu, Wei Ruan, Sung-Kwan Mo, Zahid Hussain, Zhi-Xun Shen, Feng Wang, Steven G. Louie, and Michael F. Crommie. Giant bandgap renormalization and excitonic effects in a monolayer transition metal dichalcogenide semiconductor. *Nat. Mat.*, 13(12):1091–1095, 2014.

[145] Matthew N Brunetti, Oleg L Berman, and Roman Ya Kezerashvili. Optical absorption by indirect excitons in a transition metal dichalcogenide/hexagonal boron nitride heterostructure. *J. Phys. Condens. Matter*, 30(22):225001, 2018.

[146] Heather M. Hill, Albert F. Rigosi, Alexey Chernikov, Timothy C. Berkelbach, David R. Reichman, Mark S. Hybertsen, and Tony F. Heinz. Observation of excitonic states in transition metal dichalcogenides. *Phys. Rev. Lett.*, 115(26):267403, 2015.

[147] Mackillo Kira and Stephan W Koch. Many-body correlations and excitonic effects in semiconductor spectroscopy. *Prog. Quantum Electron.*, 30(5):155–296, 2006.

[148] Florian Katsch, Malte Selig, Alexander Carmele, and Andreas Knorr. Theory of exciton–exciton interactions in monolayer transition metal dichalcogenides. *Phys. Status Solidi B*, 255(12):1800185, 2018.

[149] AL Ivanov and H Haug. Self-consistent theory of the biexciton optical nonlinearity. *Phys. Rev. B*, 48(3):1490, 1993.

[150] Yutaka Toyozawa. Theory of line-shapes of the exciton absorption bands. *Prog. Theor. Phys.*, 20(1):53–81, 1958.

[151] Galina Khitrova, HM Gibbs, M Kira, Stephan W Koch, and Axel Scherer. Vacuum Rabi splitting in semiconductors. *Nat. Phys.*, 2(2):81–90, 2006.

[152] Denis G Baranov, Martin Wersall, Jorge Cuadra, Tomasz J Antosiewicz, and Timur Shegai. Novel nanostructures and materials for strong light–matter interactions. *Acs Photonics*, 5(1):24–42, 2018.

[153] Fengrui Hu and Zhe Fei. Recent progress on exciton–polaritons in layered transition-metal dichalcogenides. *Adv. Opt. Mater.*, 8(5):1901003, 2020.

[154] F. Lengers, T. Kuhn, and D. E. Reiter. Phonon signatures in spectra of exciton polaritons in transition metal dichalcogenides. *Phys. Rev. B*, 104:L241301, Dec 2021.

[155] Dominik Christiansen, Malte Selig, Gunnar Berghäuser, Robert Schmidt, Iris Niehues, Robert Schneider, Ashish Arora, Steffen Michaelis de Vasconcellos, Rudolf Bratschitsch, Ermin Malic, and Andreas Knorr. Phonon sidebands in monolayer transition metal dichalcogenides. *Phys. Rev. Lett.*, 119:187402, Nov 2017.

[156] Aymeric Delteil, Thomas Fink, Anne Schade, Sven Höfling, Christian Schneider, and Ataç İmamoğlu. Towards polariton blockade of confined exciton–polaritons. *Nat. Mat.*, 18(3):219–222, 2019.

[157] John M Ziman. *Electrons and phonons: the theory of transport phenomena in solids*. Oxford university press, 2001.

[158] Ortwin Hess and Tilmann Kuhn. Maxwell-Bloch equations for spatially inhomogeneous semiconductor lasers: I. theoretical formulation. *Phys. Rev. A*, 54:3347–3359, Oct 1996.

[159] Roberto Rosati, Jonas K Konig, Sophia Terres, Joshua JP Thompson, Michał Baranowski, Paulina Płochocka, Alexey Chernikov, and Ermin Malic. Microscopic insights into magneto-optics and magneto-transport in 2D perovskites. *Nano Letters*, 26(16):5468–5476, 2026.

[160] S. Brem, M. Selig, G. Berghaeuser, and E. Malic. Exciton relaxation cascade in two-dimensional transition metal dichalcogenides. *Sci. Rep.*, 8:8238, 2018.

[161] A Thränhardt, S Kuckenburg, A Knorr, T Meier, and SW Koch. Quantum theory of phonon-assisted exciton formation and luminescence in semiconductor quantum wells. *Phys, Rev. B*, 62(4):2706, 2000.

[162] Viktar S Asadchy, Mohammad Sajjad Mirmoosa, Ana Diaz-Rubio, Shanhui Fan, and Sergei A Tretyakov. Tutorial on electromagnetic nonreciprocity and its origins. *Proc. IEEE*, 108(10):1684–1727, 2020.

[163] Richard B Adler, Lan Jen Chu, and Robert M Fano. *Electromagnetic energy transmission and radiation*. Wiley, 1960.

[164] Hermann Haus. *Waves and fields in optoelectronics*. Prentice-Hall, 1984.

[165] LC Botten, RC McPhedran, NA Nicorovici, and GH Derrick. Periodic models for thin optimal absorbers of electromagnetic radiation. *Phys. Rev. B*, 55(24):R16072, 1997.

[166] Jessica R Piper, Victor Liu, and Shanhui Fan. Total absorption by degenerate critical coupling. *Appl. Phys. Lett.*, 104(25):251110, 2014.

[167] J. Schilp, T. Kuhn, and G. Mahler. Electron-phonon quantum kinetics in pulse-excited semiconductors: Memory and renormalization effects. *Phys. Rev. B*, 50:5435–5447, Aug 1994.

[168] F. Lengers, T. Kuhn, and D. E. Reiter. Theory of the absorption line shape in monolayers of transition metal dichalcogenides. *Phys. Rev. B*, 101:155304, 2020.

[169] Fausto Rossi. *Theory of semiconductor quantum devices: microscopic modeling and simulation strategies*. Springer Science & Business Media, 2011.

[170] Y Chen, A Tredicucci, and F Bassani. Bulk exciton polaritons in GaAs microcavities. *Phys. Rev. B*, 52(3):1800, 1995.

[171] Stanley Pau, Gunnar Björk, Joseph Jacobson, Hui Cao, and Yoshihisa Yamamoto. Microcavity exciton-polariton splitting in the linear regime. *Phys. Rev. B*, 51(20):14437, 1995.

[172] Obafunso A Ajayi, Jenny V Ardelean, Gabriella D Shepard, Jue Wang, Abhinandan Antony, Takeshi Taniguchi, Kenji Watanabe, Tony F Heinz, Stefan Strauf, X-Y Zhu, and James C Hone. Approaching the intrinsic photoluminescence linewidth in transition metal dichalcogenide monolayers. *2D Mater.*, 4(3):031011, jul 2017.

[173] Archana Raja, Lutz Waldecker, Jonas Zipfel, Yeongsu Cho, Samuel Brem, Jonas D Ziegler, Marvin Kulig, Takashi Taniguchi, Kenji Watanabe, Ermin Malic, Tony F. Heinz, Timothy C. Berkelbach, and Alexey

Chernikov. Dielectric disorder in two-dimensional materials. *Nat. Nanotechnol.*, 14(9):832–837, 2019.

[174] Alexey Kavokin and Guillaume Malpuech. *Thin Films and Nanostructures: Cavity polaritons*. Elsevier, 2003.

[175] Vincenzo Savona. Effect of interface disorder on quantum well excitons and microcavity polaritons. *J. Phys. Condens*, 19(29):295208, 2007.

[176] Sebastian Klembt, Petr Stepanov, Thorsten Klein, Anna Minguzzi, and Maxime Richard. Thermal decoherence of a nonequilibrium polariton fluid. *Phys. Rev. Lett.*, 120(3):035301, 2018.